National Library
of Canada

Acquisitions and
Bibliographic Services Branch

395 Wellington Street
Ottawa, Ontario
K1A 0N4

Bibliothèque nationale
du Canada

Direction des acquisitions et
des services bibliographiques

395, rue Wellington
Ottawa (Ontario)
K1A 0N4

Your file Votre référence

Our file Notre référence

NOTICE

The quality of this microform is heavily dependent upon the quality of the original thesis submitted for microfilming. Every effort has been made to ensure the highest quality of reproduction possible.

If pages are missing, contact the university which granted the degree.

Some pages may have indistinct print especially if the original pages were typed with a poor typewriter ribbon or if the university sent us an inferior photocopy.

Reproduction in full or in part of this microform is governed by the Canadian Copyright Act, R.S.C. 1970, c. C-30, and subsequent amendments.

AVIS

La qualité de cette microforme dépend grandement de la qualité de la thèse soumise au microfilmage. Nous avons tout fait pour assurer une qualité supérieure de reproduction.

S'il manque des pages, veuillez communiquer avec l'université qui a conféré le grade.

La qualité d'impression de certaines pages peut laisser à désirer, surtout si les pages originales ont été dactylographiées à l'aide d'un ruban usé ou si l'université nous a fait parvenir une photocopie de qualité inférieure.

La reproduction, même partielle, de cette microforme est soumise à la Loi canadienne sur le droit d'auteur, SRC 1970, c. C-30, et ses amendements subséquents.

Canada

X-ray Structural Studies of Heteroepitaxy of Gallium-Indium Arsenide on Gallium Arsenide

by

Yushan Shi
Center for the Physics of Materials
Department of Physics, McGill University
Montreal, Canada
April, 1992

A Thesis submitted to the Faculty of Graduate Studies and Research
in partial fulfillment of the requirements for the degree of
Doctor of Philosophy

ISBN 0-315-80266-9

Abstract

This thesis presents the techniques and results of our x-ray structural studies of strained $Ga_{1-x}In_xAs$ epilayers grown on GaAs (001) by metallorganic chemical vapor deposition.

By combining conventional x-ray techniques with newly developed glancing incidence and reflectivity measurements, we study both the out-of-plane and the in-plane structure. We also obtain direct information on the mechanisms of the structural relaxation which occurs in these systems. The techniques we have used are based on using a conventional x-ray source and could be widely used to characterize and study growth processes and sample quality.

Using the conventional characterization of the positions, widths, and intensities of Bragg peaks lattice parameters, domain sizes and strains have been evaluated. Studying the shape of the Bragg peaks shows that the simple theoretical models based on the existence of a critical thickness due to dislocation can not be used to explain the structural relaxation observed. Our results based on thin (500 ± 12Å, $x=0.19\pm0.003$) and thick (40000 ± 1000Å, $x=0.16\pm0.01$) epilayers require a complicated microstructure in a transition region between the substrate and the surface of the epilayers.

Résumé

Cette thèse présente les techniques et résultats de notre étude structurale par rayons x, de couches épitaxiales de $Ga_{1-x}In_xAs$ déposées sur un substrat de GaAs (001) par déposition chimique en phase gazeuse métallorganique.

En combinant des techniques conventionelles et des techniques nouvellement développées comme des mesures par incidence rasante et des mesures de réflectivité, nous étudions les structures extraplanaires et intraplanaires. Nous obtenons aussi de l'information directe sur les mécanismes de relaxation structurale qui sont présents dans ces systèmes. Les techniques que nous avons utilisées sont basées sur l'utilisation d'une source conventionelle de rayons x et pourraient être utilisées généralement pour caractériser et étudier les procédés de croissance et la qualité des échantillons.

En utilisant la caractérisation conventionelle des positions, largeurs et intensités des pics de Bragg, les paramètres du réseau, la grandeur des domaines et des contraintes ont été évalués. L' étude de la forme des pics de Bragg montre que de simples modèles théoriques basés sur l'existence d'une épaisseur critique due aux dislocations ne peuvent être utilisées pour expliquer la relaxation stucturale observée. Nos résultats basés sur la couche épitaxiale mince (500 ± 12Å, $x=0.19\pm0.003$) et épaisse (40000 ± 1000Å, $x=0.16\pm0.01$) requièrent une microstructure complexe entre le substrat et la surface de la couche épitaxiale.

Acknowledgments

I would like to take this opportunity to thank my thesis supervisor, Prof. Mark Sutton, for introducing me to this subject and guiding me through the research, for his support, encouragement and patience.

I'd like to thank Prof. Alain Roth for providing the samples and helpful discussions, and thank Prof. Martin Grant and Dr. Zaven Altounian for valuable advice and comments on my research.

Many thanks to Loki Jorgenson and Martin Lacasse for helping me solve computer and Latex problems, to Diane Koziol and Paula Domingues for dealing with the administrative details, to Frank van Gils, John Egyed and Michel Champagne for helping me in the machine shop, and to Eric Dufresne for translating the abstract into French.

Discussions with Tony Yang, Jacques Mainville, Tianqu Gu, Steve Brauer, Hank Fischer, Yiming Huai, Yan Xu and Eric Dufresne were very beneficial to my understanding of x-ray scattering and phase transitions. All students and professors in the Center of Physics for Materials are sincerely appreciated for creating a nice atmosphere for research and study.

For my mother and father

Contents

List of Figures

Chapter 1

Introduction

The past decade has witnessed a fundamental change in the technology of fabricating electronic and photonic devices. By using epitaxial growth, many new semiconductor materials, such as III-V, II-VI compounds, and their alloys, have been explored and various novel electronic architectures, such as single and multi quantum wells, quantum wires and dots, have been constructed. In laboratories, physicists now are able to do experiments, which used to be "gedanklich" to our fathers [1–5].

Despite the great achievement of epitaxial growth, "our current understanding of the processes which control growth at a fundamental, atomic level is remarkably primitive". A panel of distinguished scientists in this field made a joint report [6] last year (1990), in which eight fundamental issues had been identified. The structure appearing during the initial stages of epitaxial growth is one of them.

As conventionally defined, epitaxial growth can be homoepitaxy provided that the materials of the overgrowth and the substrate are the same, or heteroepitaxy provided that the two materials are different. An ideal case of homoepitaxy means that there will be no interface between the epilayer and the substrate because their structures are the same. In heteroepitaxy, the structure of the epilayer differs from that of the substrate, and also differs with that of its own material in the bulk equilibrium state. This difference is most pronounced at the epitaxial interface

where the two materials contact. Because of its technological importance, and also because of its academic interest, the structure of epilayers and epitaxial interfaces has been systematically studied since 1949, and many models have been proposed [7]. A historical review of the processes of epitaxial growth, the structural issue and previous studies will be presented in next chapter.

Why is it still a problem after so many years of studies? It has also been pointed out by the panel: "thus development of new *in situ* diagnostics for growth as well as higher resolution techniques for characterization of epitaxial materials is greatly needed" [6]. As we know, many ingenious techniques, such as low-energy electron diffraction (LEED) [8], reflection high energy electron diffraction (RHEED) [9], scanning and transmission electron microscopy (SEM and TEM) [10], ion surface scattering (ISS) [11], photo- and cathodo-luminescence (PL and CL) [12], and more, have been playing important roles in the structural studies of all phases of heteroepitaxy. However, the high resolution, non-destructive and comprehensive structural measurements which provide insight on the structures of buried interfaces, as well as their effects on the structures of epilayers have been only recently started [13–16].

X-rays have been used as structural probes for a long time, and the corresponding theory, instruments and techniques are well established [17–24]. It could be argued that the discovery of x-ray diffraction brought forth the science of solid state physics, but the advantages of x-rays in structural analysis had not been fully appreciated until last decade. X-rays have been conventionally considered as a bulk probe and not suitable for studying two-dimensional (2-D) structures, because the interaction between x-rays and matter is very weak. The lack of scatterers in a 2-D system has been compensated by the abundance of photons since the late 1970s when x-ray beams from a synchrotron were made available for applied science. Since then, techniques of x-ray scattering have been developed for surface structural analysis, such as glancing incidence x-ray scattering (GIXS) and absolute reflectivity

measurements (ARM) [25–38]. X-rays have been reestablised as an unique probe for any type of atomic structure and provided an ideal tool for studying heteroepitaxy which is virtually a complex system and possesses aspects of both 3-D and 2-D structural features.

By using a triple-axis four-circle diffractometer with a 2.2 kW Cu-target tube source and Ge(111) resolution, we have measured the structure of $Ga_{1-x}In_xAs$ epilayers on GaAs substrates. This is one of the most important and most interesting systems of heteroepitaxy [39–57]. Compared with the synchrotron, the x-ray source we have used in our experiments is a weak source. In order to fully utilize this source, we have studied the intensity and wavelength distributions of the primary incident x-ray beam, and their redistribution in space after scattering by perfect crystals, *i.e.*, the resolution function of the diffractometer. The principles of x-ray scattering, the essential features of the experimental set-up, and the techniques we have practised and developed for data collection and treatment will be described in Chapter 3.

As an *ex situ* characterization of heteroepitaxy with x-ray scattering, our studies are comprehensive. This claim is not based on the number of samples we have investigated, but on the techniques we have used. Our studies have been concentrated on two samples: a thin epilayer of 500Å $Ga_{0.81}In_{0.19}As$ and a thick epilayer of 40000Å $Ga_{0.84}In_{0.16}As$, both grown on GaAs (001) substrates by metallorganic chemical vapor deposition (MOCVD). The thick sample has been originally used in our experiment as a reference for both the experimental set-up and the techniques, because it is commonly believed that the epilayer of such thickness is relaxed [44]. The thickness of the thin epilayer lies in a sensitive region, in which different structures have been reported [42,47,48,58]. As being reviewed in Section 2.4, previous structural studies of this system as a function of thickness and indium composition of the epilayers have been principally carried out by investigating a lot of samples with

various structural probes. Our work, in a sense, is a supplement or complement to previous studies. But we have observed some new phenomenon and obtained some new structural information which is difficult to achieve by using other techniques.

With respect to the epitaxial interfaces, we have measured the out-of-plane structures with normal Bragg scattering, and the in-plane structures with glancing incidence x-ray scattering. We have also studied the surface and interface morphologies of the epilayers with x-ray reflectivity measurements. By controlling the penetration depth of the x-ray beam in GIXS geometry, we have measured the evolution of the in-plane structure of the epilayers along the direction of growth and obtained direct information on the structural relaxation. Our data have been analysed with conventional techniques by studying the positions, widths and intensities of Bragg peaks to evaluate lattice parameters, domain sizes and strains. We have also studied the shape of the Bragg peaks to investigate the modulated structure of the epilayers. Contrary to the traditional concept of a critical thickness due to dislocations, our data suggest a transition region of complicated microstructure between the substrate and the surface of the epilayer to accommodate the structural relaxation. By fitting the lineshapes of Bragg peaks to models, such as the strain modulation within domain and correlated domain modulation, We have gained some insight on this transition region. The results we obtained will be presented and discussed in Chapter 4.

Chapter 5 summarizes the work and ideas presented in this thesis.

Chapter 2

Background

2.1 Epitaxial Growth

It was first found in nature that two different crystals sometimes grew together with definite and unique relationship in their orientations. This observation led to attempts to reproduce the effect in laboratories. According to the literature, the first successful attempt was reported by M. L. Frankenheim in 1836, who grew sodium nitrate crystal from solution on the surface of calcite crystal [59]. It was L. Royer who coined the term epitaxy from Greek "$\epsilon\pi\iota$" and "$\tau\alpha\xi\iota\zeta$" in 1928 to describe this type of oriented crystal growth [60]. Literally, epitaxy means "arrangement on", which can be understood as one crystal being arranged on another crystal. It can also be understood as one assembly of atoms being arranged on another assembly of atoms which had previously been periodically arranged.

Frankenheim's method is defined as liquid phase epitaxy (LPE) in modern terminology, and this was the only available technique for epitaxial growth until 1930s. Because of its simple instrumentation and fast growth rate, LPE is still used to produce electronic materials. In LPE the substrate is brought into contact with a supersaturated liquid solution in a temperature-controlled furnace, and the epitaxial

crystal is formed by carefully cooling the melt. It has been reported recently that the thickness of the epilayer grown by LPE can be well controlled at the level of tens of *nm* [61].

The monolayer control in epitaxial growth was first demonstrated in late 1960s by molecular beam epitaxy (MBE) [62], which has been considered as the technique mainly responsible for the revolution in device physics. The process of growth of MBE is simple in concept. In MBE, the constituent elements of epilayer are individually heated to their evaporation point, forming a series of elemental or molecular "beams", raining directly on the substrate in a ultra high vacuum (UHV) chamber. The flux in each beam can be controlled individually, either by varying the evaporation source temperature or by using mechanical shutters [63]. Although MBE is a powerful technique, its wide-ranging application has been limited by the need for UHV apparatus which is expensive in terms of both capital outlay and operating expense. Another major problem in MBE is the difficulty to form a "beam" of some elements, such as phosphorus. This has been found "bouncing around" in the system during the growth and producing point defects in epilayers [64].

The principal competitor of MBE is metal-organic chemical vapor deposition (MOCVD) which demonstrated monolayer scale control in the early 1980s [65]. Because of its complex process, MOCVD has proceeded somewhat more slowly than the MBE technique. In MOCVD, one or more of the overgrowing constituents are transported to the reaction zone in the form of metal alkyli, while the other constituents are usually transported as hydrides. The formation of the desired compounds occurs via the pyrolysis of the metallorganics and hydrides and the subsequent recombination of the atomic or molecular species at or near the heated substrate. The process can be well controlled by fixing the flow rates and thus the partial pressures of the various reactants with electronic mass flow controllers [66]. It has been shown that the devices produced by MOCVD and MBE have very similar performance

characteristics [64]. The major advantages of MOCVD over other techniques is a suitability for large-scale production and its versatility for making all III-V and II-VI semiconductor compounds. These make it the most widely employed technique in industrial and research laboratories.

Leaving aside the many techniques and processes of epitaxial growth, let us focus on the fundamental structural issue of heteroepitaxy. As shown in Fig 2.1, heteroepitaxy, as the term "epitaxy" is originally defined, is essentially a bicrystal system with defined orientation. Restricted by underdeveloped techniques of both growth and characterization, the earlier structural work of epitaxy was simply examining if the two crystals in contact, whether occurring in nature or grown in laboratories, had any relationship in their orientations. Barker, a chemist, who studied the growth of alkali halides upon each other in the 1900s claimed that epitaxy was more likely to occur if the molecular volume of the two intergrowing alkali halides were nearly equal [67]. With the technique of x-ray diffraction and the concept of a crystalline lattice, Royer carried out his extensive and systematic studies of a wide variety of overgrowths in 1920s, and reported that epitaxy occurred only when it involved the parallelism of two lattice planes with lattice mismatch no more than 15% [60]. The definition of lattice mismatch will be discussed mathematically in next section.

With more and more control over the process of growth, and as thinner and thinner epilayers were grown, people got closer and closer to the epitaxial interface. The chronological progress of the structural study of heteroepitaxy follows an approach from thick to thin which is just opposite to the real growing process. In 1940s, several vapor phase growth techniques, such as vacuum evaporation, electrodeposition and chemical vapor deposition, were available for performing epitaxial growth [68]. By assuming the epitaxial crystal was grown layer-by-layer at the atomic scale upon the surface of the substrate, Frank and van der Merwe calculated

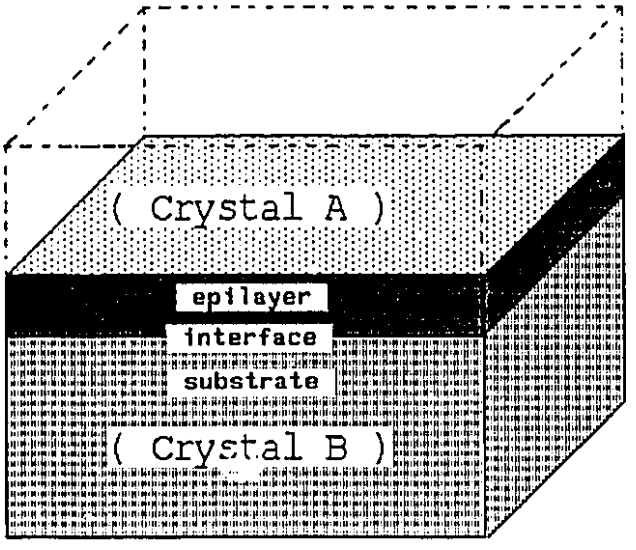

Figure 2.1: Epilayer and Epitaxial interface. Crystal B is the substrate. Crystal A is the equilibrium bulk state of the overgrowth which the epilayer will reach eventually as its thickness increases.

the equilibrium ground state of epitaxial interfaces and predicted the existence of a critical thickness of the epilayer, below which the lattice of the overgrowth was strained to match the lattice of the substrate and above which dislocations would be generated at the epitaxial interface to release the accumulated elastic energy [69]. Frank and van der Merwe's original work has dominated most subsequent treatment of epitaxy, and the structural issue of heteroepitaxy has been focused on the identification and characterization of misfit dislocations at the epitaxial interfaces to examine the critical thickness predication among various systems [70].

Because of the significant discrepancy between theoretical calculations and experimental measurements, Frank and van der Merwe's model has been modified and improved, and some new models have also been proposed, to explain the experimental observation [43, 71–73]. With more quantitative description in terms of lattice mismatch, interfacial and strain energies, these models will be briefly reviewed later in this chapter.

Major progress has occurred during the last decade in our fundamental understanding of the structural and dynamical properties of crystal surfaces, the physics of wetting and adsorption, the kinetics of phase transitions and *etc*, revealed the primitivity of our previous knowledge on heteroepitaxy [6, 74–76]. The surface of the substrate, which acts as the template for epitaxial growth has much more complicated structure than that previously thought. The pure 2-D growth, *i.e.*, the layer-by-layer growth (Frank-van der Merwe mode), is only a very special case under zero lattice mismatch between the overgrowth and the substrate or under kinetic constraint on mass transport [77–80]. Heteroepitaxial grown epilayers are more often energetically favorably formed via 3-D island growth on the bare substrates (Volmer-Weber mode) or on microscopically thin layers initially adsorbed on the substrates (Stanski-Krastanov mode) [81]. Surface and interface roughnesses introduced via island growth make the structure of epilayers and epitaxial interfaces complicated.

Although heteroepitaxy is a complex system with many variables, it can be principally separated into static and kinetic components. The current structural issue of heteroepitaxy can be technically treated as a static problem with kinetic perturbation to take care of the residual effects of growth. Based on this idea, the structural issue of heteroepitaxy will be discussed more specifically in the next two sections with the concepts of incommensurate modulation and critical thickness, which correspond to the in-plane and out-of-plane structures of the epilayers respectively.

2.2 Incommensurate Modulation

An essential feature of heteroepitaxy is the lattice mismatch between the two materials which form the overgrowth and the substrate, respectively. For modeling an epitaxial interface, let us consider two 2-D square lattices, lattice E on the top of lattice S, with the principal axes x and y in parallel, as shown in Figure 2.2. The lattice constants of E and S are denoted as a_e and a_s respectively. The vertical spacing between these two lattices is denoted as a_i, which is comparable with the lattice constant a_e or a_s. The percentage difference of the two lattice constants,

$$f = \frac{a_e - a_s}{a_s} \times 100\%, \tag{2.1}$$

is defined as the lattice mismatch provided that both a_e and a_s are the lattice constants in their equilibrium states. The parameter f is also defined as the incommensurability between these two lattices if one of them, say a_e, changes continuously. Because they are square lattices, the value of f is the same along both the x and y axes. The mutually registered lattice points in E and S form a coincidence-site lattice (CSL) [82] with period

$$p = \frac{a_e}{f}, \tag{2.2}$$

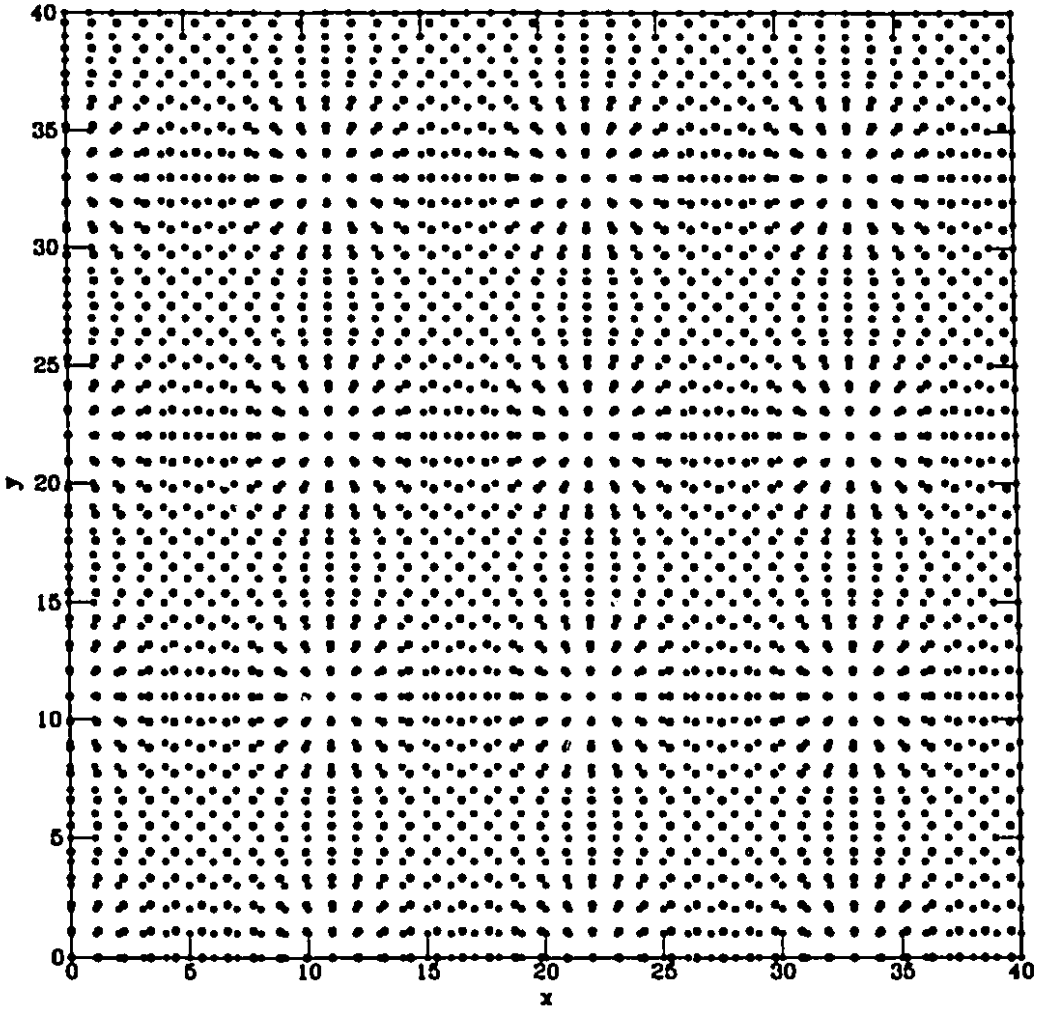

Figure 2.2: Two 2-D square lattices, lattice E (full circles, $a_e = 1.1$) on the top of lattice S (open circles, $a_s = 1.0$) with principal axes in parallel, $f = 10\%$ and $p = 11$. (f and p are defined in the text.) The vertical spacing between these two lattices, a_i, is comparable with the lattice constant a_e or a_s.

which is reciprocally proportional to the value of lattice mismatch. Equation 2.2 should exclude the case of $f = 0$, which only occurs when lattice constants a_e and a_s equal, such as in homoepitaxy. As illustrated by Figure 2.2, the misregistrations of lattice points between these two lattices can also demonstrate periodicity, as indicated by Equation 2.2.

Technically, lattice E can be considered as the first monolayer of the overgrowth and lattice S can be considered as the surface of the substrate. The lattice points in one lattice could move to achieve better registration to their nearest neighbors in the other lattice. The result in a modulated structure, which is conventionally called incommensurate modulation. For simplicity, the lattice S can be regarded as rigid in space and providing a 2-D periodic field, and only the lattice points of lattice E, *i.e.*, the atoms of the overgrowth, will be rearranged to lower the interfacial energy caused by the lattice mismatch (or incommensurability). Based on a simple sinusoidal model proposed by Frenkel and Kontorowa [83], the potential energy of lattice point $[n, m]$ in lattice E may be written as

$$V_{nm} = \frac{1}{2}W_x\left[1 - cos\left(\frac{2\pi x_{nm}}{a_s}\right)\right] + \frac{1}{2}W_y\left[1 - cos\left(\frac{2\pi y_{nm}}{a_s}\right)\right], \qquad (2.3)$$

where x_{nm} and y_{nm} its the displacements from a potential minimum of the substrate field and W_x and W_y denote the strengths of inter-lattice chemical bonding along axes x and y respectively. The minimum of V_{nm} is only reached when the lattice point $[n, m]$ is best registered to one of the lattice points in lattice S, such as at CSL points. The interfacial energy of this system can be obtained by summing over the potential energies of all lattice points in lattice E. The movement of lattice point $[n, m]$ to lower the interfacial energy causes linear and shear strains in lattice E, which are defined as

$$\epsilon_x = \frac{x_{n+1,m} - x_{nm} - a_e}{a_e}, \qquad (2.4)$$

and

$$\epsilon_{xy} = \frac{y_{n+1,m} - y_{nm}}{a_e} + \frac{x_{n+1,m} - x_{nm}}{a_e}. \tag{2.5}$$

The strain-energy density per lattice point may be written as [84]

$$U = \frac{1}{2}\mu a_e^2 \left[\frac{2(\epsilon_x^2 + \epsilon_y^2 + 2\nu\epsilon_x\epsilon_y)}{1-\nu} + \epsilon_{xy}^2 \right], \tag{2.6}$$

where μ, ν represent the shear modulus and Poisson's ratio of the material of the overgrowth. The minimum of U is only reached when the strains in lattice E are zero. The total strain energy in lattice E can be obtained by integrating over the whole lattice.

If the interfacial energy dominates completely, all the lattice points in E may be rearranged to fit the lattice of the substrate. In this case, the strains in both x and y axes equal the lattice mismatch,

$$\epsilon_x = \epsilon_y = -f. \tag{2.7}$$

The negative sign appeared in Equation 2.7 implies that the strains can actually eliminate the incommensurability between these two lattices. This is the case conventionally called "pseudomorphism", provided that the additional layers are strained to match the previous layer in the same way during the growth [69]. The corresponding expansion of out-of-plane lattice spacing, ϵ_z, caused by the in-plane lattice contraction for a cubic lattice may be calculated with classical elastic theory,

$$\epsilon_z = \frac{-2\nu}{1-\nu}\epsilon_x. \tag{2.8}$$

This relation has been frequently used to examine the "pseudomorphism" of heteroepitaxial crystals because of experimental difficulties in directly measuring ϵ_x and ϵ_y [85,86].

If the strain energy of lattice E dominates completely at the interface between these two lattices, *i.e.*,

$$\epsilon_x = \epsilon_y = 0, \tag{2.9}$$

there should be no epitaxy because the substrate has no effect on the atomic ordering of the overgrowth. Obviously, Equation 2.7 and Equation 2.9 present only the two extremes of a range of possibilities.

In general, the competition between the interfacial energy and the strain energy results in a modulated structure at the epitaxial interface. One of ideal modulated structures is presented by a monolayer of atoms adsorbed on an incommensurate substrate, as illustrated by Figure 2.2 and Figure 2.3. In this case, the modulated monolayer usually consists of an assembly of domains, which can be locally coherent with the substrate, separated by incoherent regions that are naturally called domain walls [87]. The formation of domain walls has been commonly used to describe the commensurate incommensurate (C-I) phase transitions in systems with competing interactions [88–90]. In heteroepitaxy, the modulated structure can be resulted from layer by layer growth, or from island growth (ref: Section 2.1). In principle, the behavior of C-I phase transitions is considerably different in three dimensions (3-D) and two dimensions (2-D), which may result in a complicated microstructure in the epilayer. However, the 2-D nature of C-I phase transition usually dominates at the initial stages of heteroepitaxy.

In equilibrium state, the thickness of domain wall usually depends on the atomic interaction at the epitaxial interface. The wall can be as thick as the size of the domain if the lateral interaction within lattice E is strong, or can be as thin as one row of atoms if the interaction between lattice E and lattice S is strong. The atoms can also displace out of the lattice plane, as shown in Figure 2.3 in order to lower the free energy. With the classical evaluation of the interfacial energy and elastic energy, as indicated by Equation 2.3 and Equation 2.6, the domain walls should disappear for a monolayer grown on a substrate of infinite thickness, by means of a uniform *macrostrain*, which is given by Equation 2.7. With a simple microscopic point of view, and only considering nearest neighbor interactions, the positions of atoms

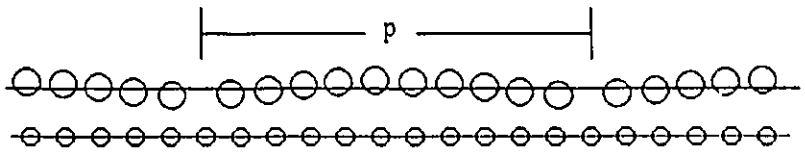

Figure 2.3: The rearrangement of lattice points in lattice E results in modulated structure which consists of correlated domains with period p.

can be locally adjusted to lower the energy by means of a non-uniform *microstrain*, which in principle lead to thick domain walls. In the latter case, there may be no macrostrain in the overgrowth and the period of domain structure equal to the period of a CSL lattice. This is indicated by Equation 2.2 and shown in Figure 2.3. In real systems, both macrostrain and microstrain may exist in the incommensurate phase of the overgrowth, and thus result in an incommensurate modulation. Even though the structural modulation may be quite complicated, the period of domain distribution can be generally estimated by the residual incommensurability of this system through the equation,

$$p_j(z) = \frac{a_j}{f - \epsilon_j(z)}, \tag{2.10}$$

where z denotes the growth axis along which the macrostrain may change, and j denotes the in-plane axis x or y for a possible asymmetrical in-plane modulation. The thickness of the domain wall is approximately proportional to the value of microstrain.

The periodicity of domain distribution and properties of domain walls can be affected by the roughness of the substrate surface and by 3-D island growth. It can also be affected by defects at the substrate surface, such as steps and kinks. In current structural studies of heteroepitaxy, these effects can be technically considered as perturbations to the intrinsic properties of heteroepitaxy. In next section, we will review some theoretical models which have been previously proposed to evaluate the structural evolution of the epilayer along the direction of epitaxial growth with the concept of critical thickness.

2.3 Critical Thickness

As mentioned in last section, heteroepitaxy is formed by means of arranging atoms at the epitaxial interface to lower the interfacial energy caused by the lattice mismatch between the overgrowth and the substrate. But this atomic arrangement increases the elastic strain energy of the epilayer. The elastic strain energy increases with the thickness of the strained epilayer, and eventually leads to structural relaxation. The structure of epilayers in heteroepitaxy has been traditionally treated as two phases: strained and relaxed, and the parameter to measure the phase transition is the thickness of the epilayer. Generation of dislocations, or in other words, formation of domain walls, is usually used to describe the mechanism of structural relaxation.

Frank and van der Merwe (F-v) assumed that the total energy E_t of heteroepitaxy was a summation of the homogeneous strain energy E_h and the dislocation energy E_d of the epilayer, which was minimum at equilibrium [69]. The dislocation energy is merely the summation of interfacial energies over the dislocation lines where the lattice points are misregistered, as indicated by Equation 2.3. For the epilayer grown on the (001) face of Silicon-like crystals, these two energies have been calculated as [84],

$$E_h = 2\mu \frac{1+\nu}{1-\nu} \epsilon^2 h, \tag{2.11}$$

and

$$E_d = \frac{\mu b^2}{4\pi(1-\nu)p} \left[1 + ln \left(\frac{2\sqrt{2(1-\nu)}}{\pi b} L \right) \right], \tag{2.12}$$

where h is the thickness, L is the lateral dimension of the epilayer, b is the value of Burger's vector, p is the averaged distance between dislocation lines, or period of in-plane domains as mentioned in last section. For simplicity, the in-plane asymmetry has not been considered in evaluating the average domain sizes along axes x and y. By differentiating E_t with the condition of "pseudomorphism", as indicated by Equation 2.7, the critical thickness h_c is related to the lattice mismatch f through

an implicit equation [84,91]

$$\frac{1}{h_c}\left[1+ln\left(\frac{2\sqrt{2(1-\nu)}}{\pi b}\,2h_c\right)\right]=\frac{8\pi(1+\nu)}{b}f. \tag{2.13}$$

Equation 2.13 leads to the dotted curve shown in Figure 2.4 for the theoretical critical thickness of $Ga_{1-x}In_xAs$ epilayers grown on GaAs substrate. The value of Poisson's ratio ν used in the calculation is 1/3, which is commonly used for III-V compound semiconductors [92]. The Burger's vector used is $\frac{a_0}{2}[110]$, where $a_0 = 5.6533$Å, is the lattice constant of GaAs crystal [49]. The value of h_c in terms of f based on F-v model is about half smaller than the photoluminescence (PL) measurement [48], but about one order as small as the structural relaxation measurement with x-rays and ion scattering [79,47].

In early 1970s, Matthews and Blakeslee had proposed a model, which is usually called the mechanical equilibrium model [72]. Matthews and Blakeslee (M-B) suggested that the misfit dislocations were introduced through the glide of threading dislocations, which required excess stress σ_{ex} for driving the relaxation process. The stability limit was given by $\sigma_{ex} = 0$ and the critical thickness for epilayers grown on GaAs (001) could be calculated with [93]

$$\frac{1}{h_c}ln\left(\frac{4h_c}{b}\right)=\frac{4\pi(1+\nu)}{(1-\nu cos^2\beta)b}f, \tag{2.14}$$

where β is the angle between the dislocation line and Burgers vector. The three dashed lines illustrated in Figure 2.4 are calculated with Equation 2.14, in the case of β equals $0°, 60°$ and $90°$ respectively. The lower curve in the figure is corresponding to the smaller value of β. It is obvious that the generation of screw dislocations at the interface requires the smallest energy. M-B's curve agrees reasonably well with the PL data, but does not agree with the x-ray data.

In 1985, People and Bean (P-B) suggested another model, which has been conventionally called as the energy balance model [72]. In P-B's model the misfit

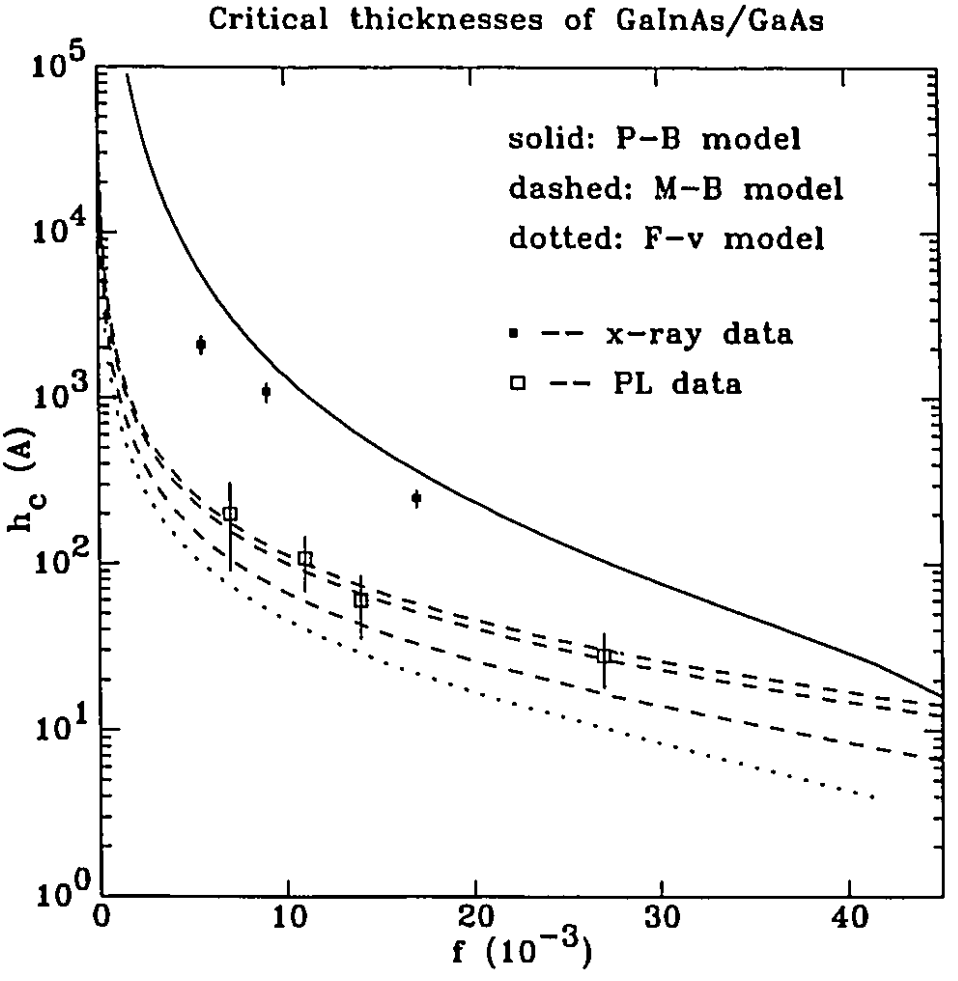

Figure 2.4: The critical thickness of $Ga_{1-x}In_xAs$ epilayers grown on GaAs substrates. The dotted line is calculated with Frank-van der Merwe's model, the solid line is calculated with People-Bean's model, and the three dashed lines are calculated with Matthews-Blakeslee's model in the case of β equals 0°, 60° and 90° respectively. The lower dashed line is corresponding to the smaller value of β. The full squares are x-ray data taken from Orders and Usher's paper [47]. The open squares are photoluminescence (PL) data selected from Weng's paper [48].

dislocation generation is determined solely by strain energy density of the epilayer in excess of the energy density associated with the formation of a screw dislocation at a distance from the free surface equal to the film thickness h. The strain energy density has been given by Equation 2.11, and the energy density associated with an isolated screw dislocation at a distance h from a free surface is approximately [94]

$$E_{sd} \simeq \frac{\mu b^2}{8\pi\sqrt{2}a} ln\left(\frac{h}{b}\right), \tag{2.15}$$

where a is the lattice constant of the overgrowth. Equating E_h and E_{sd} and setting $h = h_c$, one obtains

$$\frac{1}{h_c} ln\left(\frac{h_c}{b}\right) = \frac{32\pi(1+\nu)}{(1-\nu)b} f^2. \tag{2.16}$$

Approximating a as a_0, the GaAs lattice constant, the critical thickness of P-B's model is illustrated by the solid line in Figure 2.4. P-B's curve agrees with the x-ray data pretty well, but obviously does not agree with the P-L data.

Different theoretical calculations and different experimental measurements, which should one believe? Contributing to this perplexity are two factors: a) the resolution of the measuring techniques is not high enough, and b) the equilibrium may not have been reached under experimental conditions used. Dodson and Tsao proposed a plastic relaxation model in 1987 [73]. According to the Dodson-Tsao model, the motion of a small density of pre-existing dislocations in an applied strain field results in the generation of more dislocations through dislocation multiplication and results in plastic flow. The total amount of strain relaxed is a function of both temperature and time, and denoted as $\gamma = \gamma(t, T)$, and therefore so could the value of h_c. Combining Equation 2.14 and Equation 2.16, the following simple empirical formula can be used to calculate the critical thickness,

$$\frac{1}{h_c(\gamma)} ln\left(\frac{4h_c(\gamma)}{b}\right) = A(\gamma)f^2 + B(\gamma)f, \tag{2.17}$$

where the values of the coefficients A and B depend on the resolution of the measuring technique and γ parameterizes any non-equilibrium effect. In the case of $A = 0$,

Equation 2.17 reduces to the equilibrium form, Equation 2.14, which implies that the resolution of the experimental technique is so high that it is able to 'see' the onset of the first misfit dislocations created. In the case of $B = 0$, Equation 2.17 reduces to the form of Equation 2.16, and implies that the non-equilibrium effect obstructs the process of structural relaxation.

2.4 $Ga_{1-x}In_xAs$ on GaAs

$Ga_{1-x}In_xAs$ is one of the most important semiconductor materials and the junction of $Ga_{1-x}In_xAs$ /GaAs is one of typical systems of heteroepitaxy. The In composition x in the $Ga_{1-x}In_xAs$ alloy can be adjusted from 0 to 1 to produce materials of electronic properties between GaAs and InAs. In its equilibrium bulk state, the band gap of the $Ga_{1-x}In_xAs$ alloy is linearly determined by the value of x and covers the range 0.9-3.0 μm of the electromagnetic spectrum, which is of practical interest for infrared-emitting diodes and detectors [95,96]. In addition, the small electron effective mass for $Ga_{1-x}In_xAs$ gives electron mobilities and peak velocities considerably higher than for GaAs [97]. The heterojunctions of $Ga_{1-x}In_xAs$ /GaAs, in which the $Ga_{1-x}In_xAs$ epilayers are usually thin and strained, are superior materials for high-frequency field-effect transistor (HFFET), heterojunction bipolar transistor (HJT), and high electron mobility transistor (HEMT) devices [64].

The early MOCVD $Ga_{1-x}In_xAs$ growth studies used trimethylgallium (TMGa), trimethylindium (TMIn) and arsenic hydrides as the sources in atmospheric-pressure reactor [39, 98] (ref: Section 2.1). The basic reaction governing the formation of $Ga_{1-x}In_xAs$ can be written as

$$x(CH_3)_3Ga + (1-x)(CH_3)_3In + AsH_3 \longrightarrow Ga_xIn_{1-x}As + 3CH_4. \qquad (2.18)$$

It was found that the pressure resulted in parasitic reactions yielding low growth efficiencies and poor materials properties [99]. A major advance was the change to low

pressure (75 Torr) by Duchemin and coworkers [100]. This eliminated the prereaction problems and led to the excellent results of Razeghi and Duchemin [101]. After decades of studying and improving, the MOCVD growth of $Ga_{1-x}In_xAs$ epilayers on GaAs substrates is now almost a technique of state-of-the-art and produces high quality electronic materials which are comparable with that grown by MBE (ref: Section 2.1) [55,102].

Although $Ga_{1-x}In_xAs$ is a ternary alloy of III-V elements, it can be assigned a lattice because the In atoms are randomly distributed [40,48]. As indicated by the table of elements, indium atoms have the same electron configuration as gallium (Ga) atoms, but with 18 more electrons in a full inner shell [103]. The chemical bonding between indium and arsenic (As) is essentially the same as that between gallium and arsenic [104]. Because of the random distribution of In atoms, the $Ga_{1-x}In_xAs$ alloy can be regarded as a compound of As and $Ga_{1-x}In_x$, an effective atom with the weighted average number of electrons and forms the same type structure of GaAs (or InAs). Both GaAs and InAs crystals have zinc-blende structure but with different lattice constants, which are 5.6533Å and 6.0585Å at room temperature respectively [85]. The lattice constant of $Ga_{1-x}In_xAs$ at the equilibrium state obeys the Vegard's law [85,40] and can be calculated as

$$a = 5.6533 + 0.4051x(\mathring{A}), \tag{2.19}$$

where 0.4051Å is the difference of lattice constants between InAs and GaAs crystals. Equation 2.19 directly gives us a formula to calculate the lattice mismatch of heterojunction of $Ga_{1-x}In_xAs$ /GaAs in terms of the In composition x by $f = 7.166x\%$ (ref: Equation 2.1).

The first systematic structural study of MOCVD grown $Ga_{1-x}In_xAs$ on GaAs substrates was carried out by Nagai [40]. Nagai studied a series of $Ga_{1-x}In_xAs$ epilayers with x between 0.5 and 1.0 and thicknesses 5-10 μm and reported his observation of lattice deformation and inclination of the epilayers by using conventional

x-ray technique. This technique is alternatively called as normal Bragg scattering in this thesis and will be discussed later in detail in Section 3.2.2. By studying $Ga_{1-x}In_xAs$ on GaAs, and also other systems, such as $Ga_{1-x}In_xP$ and $GaAs_xP_{1-x}$, on GaAs or GaP substrates, Olsen and Smith pointed out that misorientation and tetragonal distortion of epilayers are general phenomena of heteroepitaxy of III-V compounds, and related these phenomena to lattice mismatchs between the epilayers and substrates by means of elastical theory of crystals [85]. In a review paper about the growth effects in the heteroepitaxy of III-V compounds, Olsen and Ettenberg summarized the previous theoretical and experimental studies and pointed out another general phenomenon of asymmetric dislocation introduction [86]. When a III-V compound was grown on the (001) faces of another III-V compound, the misfit dislocation was initially formed only along one (110) direction but not along the orthogonal one. Abrahams *et al.* had actually reported their observation about asymmetrically distributed dislocations in $Ga_{1-x}In_xP$ and $GaAs_xP_{1-x}$ (001) epilayers earlier and stated that the misfit dislocations tend to be uniformly distributed in one (110) direction, while there was a marked tendency for periodic banding of the dislocations in the other (110) direction [105]. Abrahams *et al.* attributed this asymmetry to the chemical non-equivalent of the termination of the extra half-planes of 60° dislocations at the the III-V epitaxial interface. For example, the extra half-plane of dislocation along one (110) direction was terminated with a row of atoms of group III, and the extra half-plane of dislocation along the orthogonal (110) direction would be terminated with a row of atoms of group V. The first set of dislocation was defined as α type, while the second set of dislocation was defined as β type, and their mobilities could be quite different as reported by Kuester *et al.* for GaAs crystals [106].

The asymmetries in dislocation densities, surface morphology, and strain of MBE grown $Ga_{1-x}In_xAs$ epilayers on GaAs (001) substrates as a function of indium

composition and layer thickness were furtherly investigated by Kavanagh *et al.* by using transmission electron microscopy (TEM), medium energy ion blocking (MEIB) and double-crystal x-ray diffractometry (DXD) [49]. TEM studies showed that 60° α dislocations formed first in only one (110) direction at the interface for thin epilayers (900 and 1600 Å and $x = 0.07$). But asymmetry in residual strain was not detected by DXD in these samples. In the epilayers thicker than 3000Å ($x = 0.07$), orthogonal arrays of dislocations (60° and edge type) were observed with equal densities. But both MEIB and DXD indicated asymmetry in in-plane strain for these thick epilayers. Based on their results, Kavanagh *et al.* pointed out that 60° Burgers vectors were restricted to one or two of the four possible Burgers vectors when the epilayer was thin and asymmetrically distributed when the epilayer was thick. In addition, the edge type dislocations with asymmetric densities were observed in the thick epilayer which might compensate the asymmetry of dislocation densities of 60° type, and produced a dislocation network with about the same densities along the two in-plane orthogonal (110) directions.

More plan-view TEM analysis of MBE grown $Ga_{1-x}In_xAs$ /GaAs strained epilayer was performed by Dixon and Goodhew [53]. They reported their results that there were two critical thicknesses (ref: Section 2.3), corresponding to the turnover of threading dislocations and the nucleation of new dislocations. And they also pointed out that not all interfacial dislocations acted to relieve the misfit strain. Recent TEM studies on the formation, interaction and propagation of misfit dislocations at MBE grown $Ga_{1-x}In_xAs$ /GaAs heteroepitaxial interface have been carried out by Chang *et al.* [50]. Chang *et al.* reported that with the strained systems of less than 2% lattice mismatch, the majority of the misfit dislocations were confined at the same heterointerface after the elastic strain relaxation. Most of the misfit dislocations were found to be mixed dislocations with Burgers vector of $a/2(110)$ type at 60° to the dislocation line. Sessile type edge dislocations could

also originate from the combination of two 60° mixed dislocations. Numerous sessile edge dislocations were generated during the later part of the elastic strain relaxation through climb or interaction processes. The interfacial dislocation network was found to contain regions of dislocation with the same Burgers vector that extend over several micrometers. The structural evolution of the strained $Ga_{1-x}In_xAs$ epilayers on GaAs (001) at initial stage of MBE has been recently studied by Snyder *et al* by using *in situ* scanning tunneling microscopy (STM) and reflection high energy electron diffraction (RHEED) [107]. They observed the effect of strain that resulted in a 2-D rippled surface in the initial stages and then turned to be a 3-D island morphology during the growth of the epilayer, and pointed out that significant strain relief might be accommodated by coherent islands.

Many experimental data on the structures of $Ga_{1-x}In_xAs$ /GaAs heterojunction have been collected by various techniques since Nagai, and most of them have shown the same features on dislocation interaction and lattice relaxation when the epilayers are thick (thicker than P-B's h_c, ref: Section 2.3) and with high densities of dislocations. The dislocations are usually studied by TEM and the lattice relaxation is usually measured by conventional x-ray techniques and their results are compatible. With thiner epilayers (thiner than P-B's h_c and thicker than F-v's h_c, ref: Section 2.3), the dislocations can be seen by TEM, but the corresponding lattice relaxation has not been detected by x-ray scattering. Because of the techniques needed to prepare thin samples for TEM studies, there is always the worry that different effects are being studied. Photoluminescence (PL) is extremely sensitive to the defects of the epilayer and may provide a low limit of probing the onset of dislocations. The PL data collected by Weng [48], as shown in Figure 2.4, seems to agree quite well with M-B's h_c. But there is little structural information that can be extracted from PL data, because the line widths are sensitive to material uniformity on the scale of the carrier diffusion length or the probe spot size, whichever is larger.

The typical dimensional resolution of PL measurement is about 1 μm.

With x-ray scattering, one should be able to "see" the lattice relaxation, and possibly also "see" the onset of dislocations. High resolution and comprehensive x-ray measurements should help to resolve some these problems. To this end, we need not only a good understanding of the system and the issue, but also a good understanding of the principles and techniques of x-ray scattering.

Chapter 3

Experiment

3.1 Principles of X-ray Scattering

X-rays are electromagnetic radiation with wavelengths on the order of 1 Å, and have been used to probe the atomic structures of condensed matter since the phenomenon of x-ray diffraction was first observed in 1912 [108, 17]. The coherence length of a well monochromated x-ray beam is on the order of 1 μm, and in principle is able to reveal any microstructures up to such a length scale.

The fundamental process of x-ray scattering is the electromagnetic interaction between x-ray photons and atomic electrons which has been best described by the theory of quantum electrodynamics [109]. Because the nature of atomic structural studies with x-rays is the coherent summation of elastic scatterings from different scatterers, a classical treatment of the scattering process with proper quantum correction is easier to understand and more appropriate to be used to describe the principles of the experiment.

The elemental "building blocks" of condensed matter are atoms, and each of which consists of certain number of electrons and one atomic nucleus. As shown

in Figure 3.1, the elastic scattering of x-rays is usually expressed as a function of the momentum transfer, q, which is defined by $\mathbf{q} = \mathbf{k}_o - \mathbf{k}_i$, the difference between wavevectors of the scattered and the incident x-rays. The plane defined by $\mathbf{k}_o$ and $\mathbf{k}_i$ is called the scattering plane, and the vector q is also called the scattering vector. The cross-section of x-rays elastically scattered by a free electron is given by the well-known Thomson scattering equation [23],

$$\left.\frac{d\sigma(q)}{d\Omega}\right|_{ele} = r_0^2 P(q), \tag{3.1}$$

where $r_0 = e^2/mc^2 = 2.82 \times 10^{-13} cm$ is the classical radius of the electron and $P(q)$ is the polarization factor. With respect to the scattering plane, the polarization factor $P(q)$ can be written as

$$P(q) = \frac{1}{2}\left[1 + \gamma\left(1 - \frac{q^2}{2k^2}\right)^2\right], \tag{3.2}$$

where k is the magnitude of $\mathbf{k}_i$ or $\mathbf{k}_o$, and γ is the polarization coefficient of the primary incident beam, which is defined as the ratio of x-ray intensities of the parallel component to the perpendicular component. For an unpolarized beam, γ equals 1. Eq 3.1 can be equally used to describe the x-ray elastic scattering of the atomic nucleus by substituting the charge and mass of the electron in r_0 with those of the nucleus respectively. This shows that the x-ray scattering cross-section of nucleus is million times smaller than that of electrons and can be ignored in atomic structural analysis. Recent measurements of nuclear resonant scattering are exception to this [110].

The cross-section of x-rays scattered by a single atom with thermal vibrations can be written as

$$\left.\frac{d\sigma(q)}{d\Omega}\right|_{atm} = {r_0}^2 P(q)|f(q)|^2 e^{<u^2>q^2}, \tag{3.3}$$

where $f(q)$ is the atomic form factor, $e^{<u^2>q^2}$ is the Debye-Waller factor and $\langle u^2 \rangle$ denotes the averaged square of atomic vibration magnitude. The atomic form factor represents the distribution of electrons within the atom and can be generally

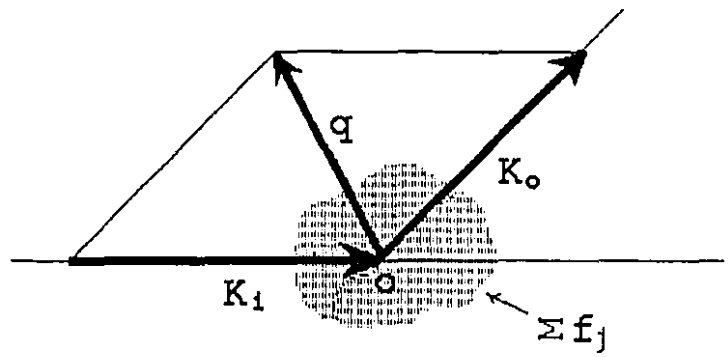

Figure 3.1: X-ray scattering. The wavevectors of incident and scattered x-rays are denoted as $\mathbf{k}_i$ and $\mathbf{k}_o$ respectively and define the scattering plane. Their difference is the momentum transfer of the x-rays. It is called the scattering vector and denoted as q. $\sum f_i$ represents the assemblage of atoms which scatter x-rays.

expressed by

$$f(q) = f_0(q) + \Delta f'(q) + i\Delta f''(q). \tag{3.4}$$

The first term, $f_0(q)$, is the classical term obtained by assuming that electrons are continuously distributed inside the atom with spherical symmetry. The second and third terms in $f(q)$ represent the dispersive corrections due to both the quantum energy levels inside the atom and the outermost electrons which may spread over the sample, such as in metals [23]. The maximum value of $f_0(q)$ is the atomic number of the atom when $q = 0$, *i.e.*, $f_0(0) = Z$. The magnitude of dispersive correction is usually less than a few percent for x-rays.

A coherent summation of scatterings from an assemblage of atoms can be directly generated from Eq 3.3,

$$\left.\frac{d\sigma(q)}{d\Omega}\right|_{coh} = {r_0}^2 P(q) \left| \sum_{j=1}^{N} S_j(\mathrm{q}) f_j(q) e^{i\mathrm{q}\cdot\mathrm{r}_j} e^{\frac{1}{2}<u_j^2>q^2} \right|^2, \tag{3.5}$$

where the subscript j denotes an individual atom j located at the equilibrium position r_j and N is the total number of atoms within the coherent region determined by the coherence length of the incident x-ray beam. The two new factors appearing in Eq 3.5, are $S_j(\mathrm{q})$, called the coherence factor in this thesis and $e^{i\mathrm{q}\cdot\mathrm{r}_j}$, called the phase factor. They bear the information of the configuration of this assembly of atoms and play important roles in the analysis of x-ray techniques and structures.

In a real experiment, the illuminated volume of the sample is usually much larger than the coherent region of the incident beam. Thus an incoherent summation of the scattering from all coherent regions within the illuminated volume is required to calculate the intensity. The total scattering cross-section may be obtained by integrating over the illuminated volume x, and written as

$$\frac{d\sigma(q)}{d\Omega} = \int_x \left.\frac{d\sigma(q,x)}{d\Omega}\right|_{coh} \frac{I(x)}{X_{coh}} dx, \tag{3.6}$$

where $I(x)$ is the x-ray intensity distribution over the illuminated volume, and X_{coh} is the size of a single coherent region of the incident x-rays. The x-dependent

integrand, $\frac{d\sigma(q,x)}{d\Omega}\Big|_{coh}$, denotes that the scattering patterns may change from region to region due to local structural fluctuations. It has been reported recently that this fluctuation can be experimentally studied with coherent x-rays [111].

In the normal case of structural determination, the fluctuations have been averaged over the whole illuminated volume of the sample, as indicated by Equation 3.6, and therefore only the global structural features are revealed. When determining the desired structural parameters, such as lattice constants and crystal types, the issue of the coherent region is unimportant. The coherent summation in Equation 3.5 is usually taken over all the scatterers of the whole illuminated volume of the sample for simplicity.

The coherence factor in Eq 3.5 for atom j can be considered as the ratio of the scattering amplitudes scattered by the same atom *i.e.*, atom j, with and without the existence of all other atoms. The explicit form of the beam factor can be worked out under approximations which can be properly chosen according to the structural and geometrical features of the sample and also the techniques of x-ray scattering involved.

As indicated by Eq 3.3, the interaction between x-rays and atoms is very weak and an approximation of considering only single scattering is natural and reasonable. Under this approximation (Born approximation), the beam factors are same for all atoms and equal to 1, *i.e.*,

$$S_j(\mathrm{q}) = 1. \tag{3.7}$$

In this case, Eq 3.5 is reduced to

$$\frac{d\sigma(q)}{d\Omega}\Big|_{coh} = {r_0}^2 P(q)|F(\mathrm{q})|^2, \tag{3.8}$$

where

$$F(\mathrm{q}) = \sum_{j=1}^{N} f_j(q) e^{\frac{1}{2}<u_j^2>q^2} e^{i\mathrm{q}\cdot\mathrm{r}_j}, \tag{3.9}$$

can be regarded as a generalized structure factor of the sample. Eq 3.8 presents the principle of kinematical theory of x-ray scattering and its conceptual simplicity shows the fundamental advantage of x-rays in atomic structural studies.

In a crystal, all atoms are periodically arranged. The structure factor $F(\mathbf{q})$ is greatly simplified by using translational symmetry. The scattering pattern determined by Eq 3.8 has the same symmetry in q-space with periodically distributed scattering intensity maxima, which are usually called Bragg peaks. If the ordering of atoms is modulated, the scattering pattern in q-space is also modulated, but in a reciprocal way. The shape of Bragg peaks can provide us the information of larger scale structures which have been superimposed on the fundamental ordering of atoms.

If the atomic ordering in a crystal is perfect up to a macroscopic length scale, say a perfect crystal, the Bragg peaks calculated by Eq 3.8 are basically δ-functions in q-space. This does not agree with experiment. Because of the perfect ordering of scatterers, the collective effects of multiple scattering in a perfect crystal can not be ignored. In this case, the beam factor $S_j(\mathbf{q})$ must account for the effect of interference between the primary incident x-rays and the scattered x-rays by all atoms within the coherent region except that by atom j. The theory of x-ray scattering originally developed for perfect crystals is called dynamical theory. Its principal correction to the kinematical theory is a width to the Bragg peaks called the Darwin width [23]. The value of Darwin width is determined by the atomic density of the material and the wavelength of x-rays [112]. The existence of a Darwin width can also be understood as the result of a rapid attenuation of x-ray intensity inside the sample under Bragg conditions. The explicit form of beam factor $S_j(\mathbf{q})$ for perfect crystals can be worked out in principle by solving Maxwell equations in an electric medium of periodic permittivity [113].

As shown in last chapter, the geometric feature of heteroepitaxy is a thin film

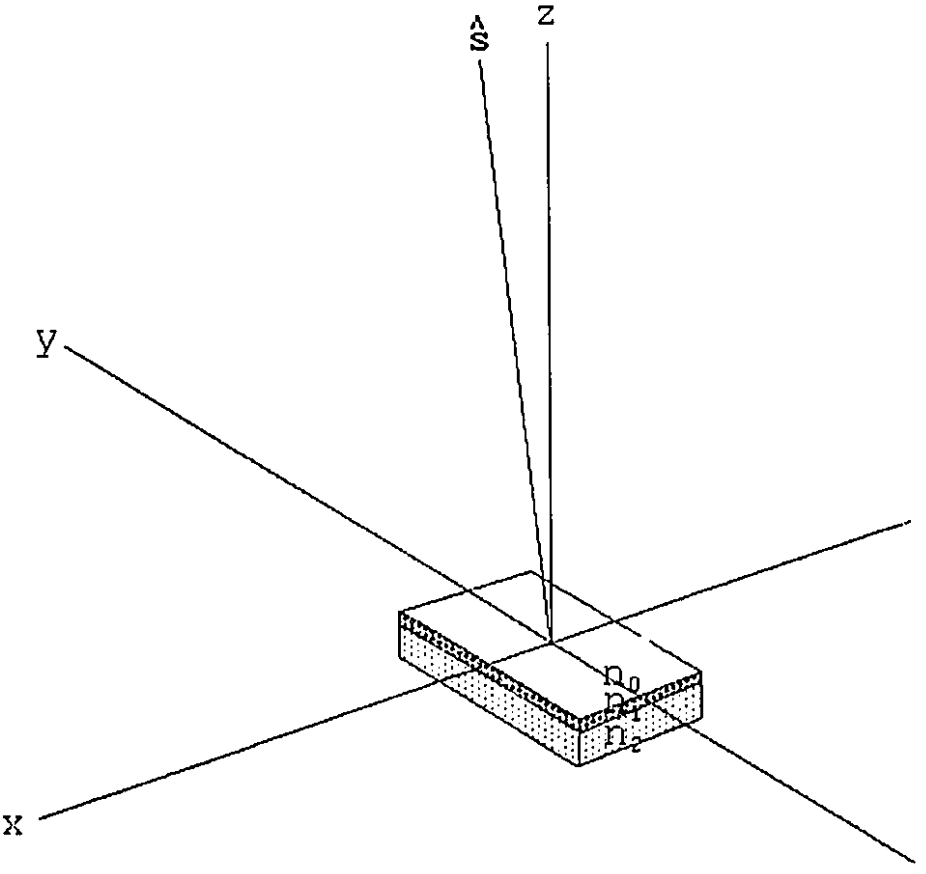

Figure 3.2: X-ray optics. The refraction indices of air, the epilayer and the substrate are denoted as n_0, n_1 and n_2 respectively. The misalignment between the surface normal and the axis z defined by the crystal axis of the substrate is due to the mechanical miscut.

on a crystalline substrate with an extended surface, and its structure should be studied both in-plane and out-of-plane. Another effect of multiple scattering which occurs whenever the projection of the x-ray momentum transfer q along the sample surface normal is very small, *i.e.*, glancing incidence scattering, has been used to study the in-plane structures [25].

The surface normal of the sample is denoted by $\hat{s}$, as shown in Fig 3.2, which may not agree with the z-axis of the sample coordinate system defined by the principal crystallographic axes of the substrate. The angle between $\hat{s}$ and the axis z usually equals the surface miscut. When the component of scattering vector q along the surface normal *i.e.*, q_s has been set to be very small, x-rays are no longer sensitive to the electron density change of the sample on an atomic scale, and the sample can be treated as a macroscopic optical medium. The x-ray index of refraction, n_l, of the medium l is proportional to the atomic factor of atoms, and can be written as

$$n_l = 1 - \delta_l + i\beta_l, \tag{3.10}$$

with

$$\delta_l = \frac{2\pi}{k^2} r_0 \rho_l [f_{0l}(0) + \Delta f_l'(0)], \qquad \beta_l = \frac{\rho_l}{2k} \Delta f_l''(0),$$

where k is the magnitude of the wavevector of x-rays in vacuum, ρ_l is the atomic density of medium l. For compound materials, an effective atomic form factor and atomic density can be used to define the refraction index. Total reflection occurs at interfaces whenever x-ray photons attempt to enter a less optically dense medium, provided that the value of q_s is smaller than a critical value [18,114].

The relation between q's in different optical media, say n_l and n_m, with common interface follows Snell's law, which can be stated as

$$n_l \sqrt{(2k)^2 - q_{ls}^2} = n_m \sqrt{(2k)^2 - q_{ms}^2}. \tag{3.11}$$

In our study, the refraction index of air, the epilayer and the substrate are denoted as n_0, n_1 and n_2 respectively, as shown in Fig 3.2. Since $n_0 = 1$, the critical value of

q_z at the top surface of the sample, denoted as q_{01c}, can be easily worked out to be $2k\sqrt{2\delta_1}$ from Equation 3.11. The penetration depth of the x-ray evanescent wave for the sample surface, denoted as Λ_{01} is given by [115]

$$\Lambda_{01}^{-1} = \frac{1}{\sqrt{2}}\left(\sqrt{(q_{0z}^2 - q_{01c}^2)^2 + 4(2k)^4\beta_1^2} + q_{01c}^2 - q_{0z}^2\right)^{1/2}. \tag{3.12}$$

As indicated by the equation, the penetration depth is controlled by q_{0z}, the surface normal component of q in air. When Λ_{01} is larger than the thickness of the epilayer, x-rays cross the epitaxial interface and enter the substrate. The penetration depth of x-rays for the epitaxial interface Λ_{12} takes the same form as Λ_{01} in Eq 3.12 by merely changing the subscripts of the two media correspondingly.

Under the glancing incidence alignment, the explicit form of the beam factor in Eq 3.5 is a function of q_z, which can be worked out with Distorted Wave Born Approximation [116, 36]. If the miscut angle of the surface to the crystal plane of substrate is zero, *i.e.*, $q_z = q_z$, and under the condition of specular scattering, *i.e.*, $q_x = 0, q_y = 0$,

$$S_j(\mathbf{q}) = \frac{2q_z}{q_z + \sqrt{q_z^2 - q_{01c}^2}} e^{\frac{1}{2}q_z\sqrt{q_z^2 - q_{01c}^2}\sigma_{01}^2}, \tag{3.13}$$

where σ_{01} denotes the *rms* value of roughness at the surface of the sample. Because the interface between different mediums may not be atomically flat, the roughness can be approximated by a Gaussian distribution, and gives a term which is similar to that from thermal motion of atoms. Eq 3.13 is, aside from the roughness term, the well-known Fresnel transmission coefficient and the contribution of individual atoms are not distinguished.

A general form of the beam factor with $q_x \neq 0$ and/or $q_y \neq 0$, which includes both the non-specular scattering and the small mechanical miscut angle between the z axis and the surface normal $\hat{s}$ of the sample, as shown in Fig 3.2, can be derived

from Eq 3.13,

$$S_j(\mathbf{q}) = \sqrt{\frac{2q_{z-}}{q_{z-} + \sqrt{q_{z-}^2 - q_{01c}^2}}}\sqrt{\frac{2q_{z+}}{q_{z+} + \sqrt{q_{z+}^2 - q_{01c}^2}}}e^{\frac{1}{2}q_z\sqrt{q_z^2 - q_{01c}^2}\sigma_{01}^2}, \tag{3.14}$$

where

$$q_{z+} = \frac{q_z^2 + \sqrt{q_x^2 + q_y^2}\sqrt{(2k)^2 - q_z^2}}{\sqrt{q_x^2 + q_y^2 + q_z^2}},$$

$$q_{z-} = \frac{q_z^2 - \sqrt{q_x^2 + q_y^2}\sqrt{(2k)^2 - q_z^2}}{\sqrt{q_x^2 + q_y^2 + q_z^2}},$$

relating to the unequal incident and exit angles of x-rays to the surface of the sample respectively. Since the surface miscut of the sample is usually a fixed parameter during the x-ray measurement, these two cases included in Equation 3.14 can be further distinguished by the form of phase factors used in the summation of the structure factor of the epilayer.

Due to the mechanical miscut at the sample surface, the epitaxial interface is not parallel to the plane defined by crystal axes x and y of the substrate, and the in-plane summation limits of the structure factor of the epilayer given in Eq 3.5 is generally a function of the out-of-plane summation index. The form of this function is determined by the surface miscut.

The Fresnel reflectivity of x-ray scattering at the surface of the sample is readily obtained by integrating over the differential cross-section given by Eq 3.5 [36]

$$R_{01} = 16\pi^2 r_0^2 \rho_1^2 \frac{|S_j(\mathbf{q})|^4}{q_z^4} = |r_{01}|^2. \tag{3.15}$$

It is interesting to note how the x-ray reflectivity relates to the transmission coefficient in the above equation. The reflectivity at the interface between the epilayer and the substrate r_{12} has the same form as r_{01} by merely substituting the atomic density ρ_1 and the beam factor $S_j(\mathbf{q})$ by those of the substrate. The total reflectance from this system can be written as

$$r = \frac{r_{01} + r_{12}e^{in_1 q_{1z} h}}{1 + r_{01}r_{12}e^{in_1 q_{1z} h}} \tag{3.16}$$

where h is the thickness of the epilayer and its modulation on the reflectivity curve provides an accurate determination of the thickness. The interfacial roughness σ_{12} contained in r_{12} which affects the amplitudes of thickness modulation along q_z can also be used to evaluate the interfacial roughness [117].

To make a summary to this section, let us come back to Equation 3.5. The terms of the summation in Equation 3.5 contains two factors conceptually: one depends on the atomic configuration and the other one depends on coherence effects. The first one is what we want to measure, and the second one can be adjusted to realize the various x-ray structural techniques. Under the approximation of single scattering, as indicated by Equation 3.7, 3.8 and 3.9, the first factor dominates, and the scattering pattern is simply a Fourier transform of the density-density correlation function of the sample. In the extreme case of multiple scattering, such as x-rays incident with glancing angle at the sample surface, the second factor dominates, and the sample can be considered as stratified optical medium. Equation 3.13, 3.14, 3.15 and 3.16 indicate that the surface and interface morphology of the epilayer (or thin film) can be studied. Combining these two results in the technique of glancing incident x-ray scattering (GIXS) which is particular useful for studying the atomic structures in two dimensions. By accurately controlling the penetration depth of x-ray evanescent wave in GIXS geometry, the depth selectivity of x-rays provides a direct measure of the structures intermediate to 2-D and 3-D.

3.2 Techniques and Geometry

3.2.1 Experimental Set-up

The experimental measurements of scattering patterns are carried out by using a triple-axis four-circle x-ray diffractometer with a conventional 2.2 kW Cu-target tube source. Because the construction and general features of this diffractometer have

been described in detail in my Master's thesis [118], here only a brief description of the set-up which is necessary for us to understand the techniques and geometry will be presented.

As shown in Fig 3.3(a), a diffractometer consists of three major parts: the source, the detector and the goniometer. The source is responsible for providing a well defined primary incident beam, and this beam will be discussed in detail in next section. For simplicity, a parallel beam with only single wavelength, say Cu-$K_{\alpha 1}$ line, is used here to describe the techniques and the geometry. The detector is adjusted to accept all elastically scattered x-ray photons passing through Slit 4 and reflected by the analyzer crystal. The sample is mounted on the center of a goniometer with four circles, 2θ, θ, χ and ϕ. The plane defined by the source, the center of the goniometer and the counter is called scattering plane which is parallel with the floor in the laboratory and parallel with the paper in the figure. The normal of this plane, is the principal axis of the diffractometer. The monochromator crystal, the analyzer crystal and all the vertical slits along the beam are aligned symmetrically with respect to the scattering plane.

To achieve high resolution, two identical Ge single crystals with (111) surface normal are used as monochromator and analyzer, and mounted in front and behind the sample, as shown in Figure 3.3(a). Four slits are employed along the x-ray beam to adjust the beam cross-section and intensity, and also assist in alignment. The mechanical resolution of Slit 1, Slit 2 and Slit 3 are 0.01 mm in both horizontal and vertical direction, and among them Slit 3 is controlled by the computer. Slit 4 is actually the rectangular window of the analyzer housing. The resolution of all four circles of the goniometer is determined by the steps of the Huber gears and the reducing gears, which is 0.00025°. The geometric parameters of this set-up are given and illustrated in Fig 3.4.

With respect to the scattering plane, the momentum transfer of x-ray scatter-

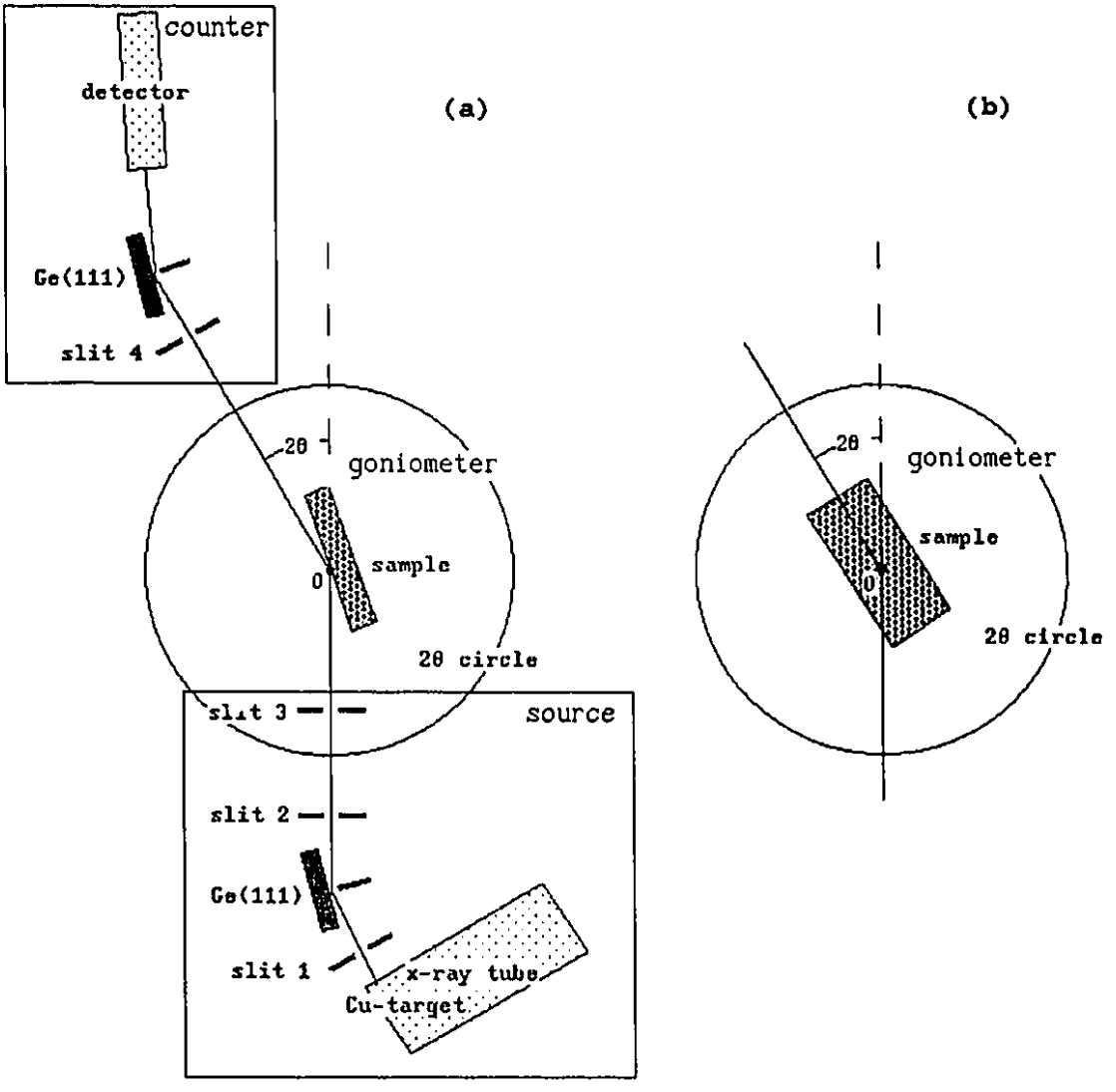

Figure 3.3: Experimental set-up: (a) normal scattering, (b) glancing incidence scattering. The plane shown is the scattering plane and parallel to the floor in the laboratory.

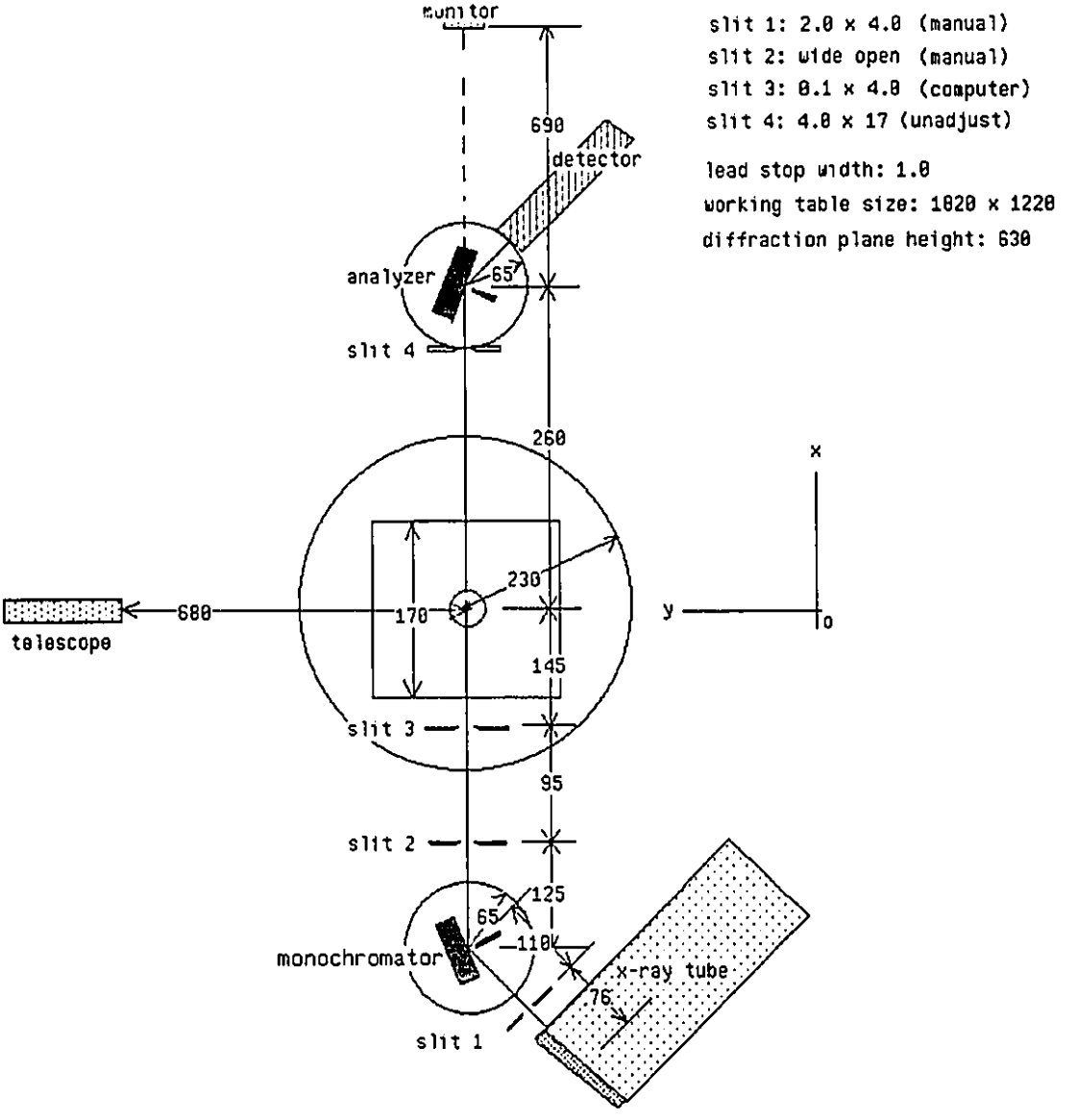

Figure 3.4: The geometrical parameters of the set-up. The horizontal and vertical widths of slits as labeled have been used for reflectivity measurements. The unit of figures is mm.

ing q can be decoupled into in-plane and out-of-plane components. The out-of-plane component, q_v, is usually of quite low resolution and the change of resolution with q can be ignored. The in-plane component can be further decoupled into longitudinal and transverse components which are denoted as q_l and q_t respectively. These three mutually perpendicular components, *i.e.*, q_l, q_t and q_v define the Cartesian coordinates of the diffractometer with units of inverse angstroms (Å^{-1}). The in-plane resolution function is principally determined by the reflections of the monochromator and analyzer. In this set-up, the in-plane resolution is limited by the Darwin width of Ge (111) [118].

Generally, the intensity distribution of scattered x-rays is a convolution integral of all the components along the x-ray beam from the tube to the detector. In principle, this distribution in terms of the variables, q_l, q_t and q_v, can be written as

$$\begin{aligned} I(q_l, q_t, q_v) &= \int_\alpha \int_\lambda \int_v \int_t J(\lambda) F(\alpha) S_x(t,v) S_1(t,v) R_M(q_M) S_M(t) S_2(t,v) \\ &\quad S_3(t,v) R_S(q_S) S_4(t,v) S_A(t) R_A(q_A) S_d(t,v) d\alpha d\lambda dv dt \end{aligned} \tag{3.17}$$

where $J(\lambda)$, $F(\alpha)$ and $S_x(t,v)$ are the wavelength distribution, divergence and spot size of the x-ray beam emitted from the tube. $S_i(t,v)$ represents the effect of Slit i, and i = 1, 2, 3, 4. The subscripts, M, S, A, denote the monochromator, sample and analyzer crystals respectively. Their scattering is expressed by $R_M(q_M), R_S(q_S)$ and $R_A(q_A)$, where q_M, q_S and q_A are the corresponding x-ray momentum transfers. The subscripts x and d denote the x-ray tube and detector. The variables t and v denote the sizes of horizontal and vertical windows.

Equation 3.17 is a conceptual representation of the experimental setup. It is a complicated integral and can be usually simplified in practical use. With wide open slits, perfect crystals and integrating over the vertical component, Equation 3.17 leads to a simple formula,

$$I(\Delta q_l, \Delta q_t,) = \int_\alpha \int_\lambda X(\lambda, \alpha, t) R_M(q_M) R_S(q_l, q_l) R_A(q_A) d\alpha d\lambda, \tag{3.18}$$

where $X(\lambda, \alpha, t) = J(\lambda)F(\alpha)S_x(t)$ denotes the x-ray source. Equation 3.18 can be used to evaluate the widths of in-plane Bragg peaks produced by a perfect crystal as sample, *i.e.*, to evaluate the in-plane resolution function.

Figure 3.5 shows the intensity distribution of the (111) reflection of a perfect Si crystal taken with this geometry. The $\langle 111 \rangle$ axis of the sample is set along q_l, and q_t has been scanned along $\langle 1\bar{1}0 \rangle$. The units used in this mesh will be discussed later in Section 3.4. The contour lines in the figure are plotted on a logarithmic scale and differ in intensities by factors of two. The maximum intensity of this peak is 54000 counts per second. Since the Si (111) reflection is almost a non-dispersive reflection for this diffractometer and since its Darwin width is smaller than that of Ge(111), the wavelength spread of the x-ray source in Eq 3.18 can be approximated as a δ-function. The scattering of triple perfect crystals can be therefore simplified as a convolution of the three scattering functions of the monochromator, the sample and the analyzer. These scattering functions of perfect crystals have been approximated as Gaussian or Lorentzian distributions to evaluate the resolution function of triple-axis diffractometer [119,120].

The three streaks intersecting at the center of the Si (111) peak, as shown in the figure, reveal the essential feature of a scattering pattern produced by three perfect crystals. The streak at the center is caused by the scattering of the sample. This streak is misaligned from q_l by about 1°, this is attributed to the miscut on the surface of the sample. The streak from the bottom left to the top right is caused by the monochromator, and the streak from the bottom right to the top left is caused by the analyzer. The angle between these two inclined streaks equals the scattering angle of Si (111). The slight intensity asymmetry on these two streaks can be attributed to the asymmetric collimation of slits on the incident and the scattered x-ray beams. The length of the streak can be used to evaluate the surface roughness of the crystal that produces the streak. For imperfect crystals and for

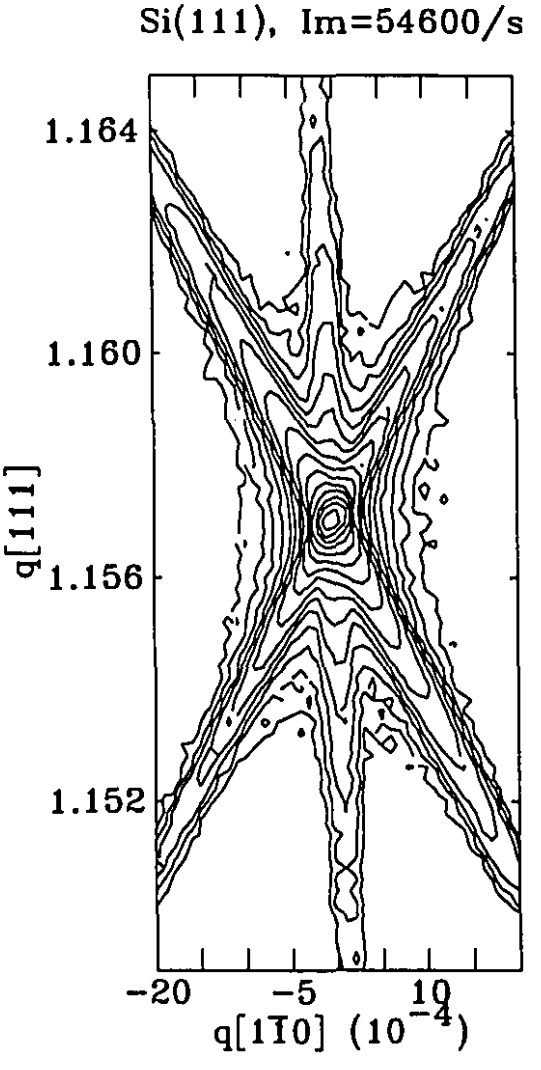

Figure 3.5: Triple crystal scattering. Si (111) peak in $(1\bar{1}0)$-(111) plane, which is basically non-dispersive scattering in this setup. The streak at the center is caused by the sample, which has been miscuted about 1° to Si (111) planes on the surface. The streak from the bottom left to the top right is caused by the monochromator, and the streak from the bottom right to the top left is caused by the analyzer. The angle between these two inclined streaks equals to the scattering angle of Si (111). The axis of $q[1\bar{1}0]$ has been enlarged by a factor of 2 in the figure for clarity.

weak scattering, streaks are usually not seen.

With a Gaussian approximation for the Darwin crystal scattering functions, Cowley and his colleagues have worked out the resolution function of a triple crystal x-ray diffractometer in detail [120–122]. According to Cowley's treatment, the in-plane resolution function with conventional tube source and Ge(111) monochromator and analyzer are plotted with solid curves in Figure 3.6. The resolution of longitudinal scan, *i.e.*, Δq_l, is limited at the non-dispersive alignment, while the resolution of transverse scan, *i.e.*, Δq_t linearly increases with q_l from $q_l = 0$. Cowley monochromated the incident x-rays to only the Cu-$K_{\alpha 1}$ line with slits and measured the peak width of perfect crystals. His experimental data agrees pretty well with his theoretical calculation when q_l is bigger than 4 Å^{-1} [121]. With perfect Si and GaAs crystals, we have also measured the widths of Bragg peaks. We have kept the whole beam profile of Cu-K_α emission line without isolating Cu-$K_{\alpha 1}$ line with slits. Our data agree quite well with the theoretical curves. The out-of-plane resolution of this set-up, Δq_v, equals 0.022Å^{-1}, which is independent of q_l.

A not purely monochromated incident x-ray beam has been used in our high resolution measurement. Two principal reasons can be listed. 1) To monochromate the incident beam further with slits or by crystal reflection, we usually have to sacrifice beam intensity which is very precious for weak scattering, such as the scattering from epilayer and interface. 2) If the intensity and wavelength distributions of the incident x-ray beam are well defined, high resolution data can still be obtained from data treatment because the x-rays of different wavelengths are incoherent. In the dispersive case, the scattering due to x-rays of different wavelengths spread out along q_l. The whole scattering pattern can be simply treated as the superposition of patterns produced by x-rays of single wavelength with corresponding origins along q_l. The wavelength distribution of the primary incident beam will be discussed in detail in Section 3.3 and the techniques of data collection and treatment will be

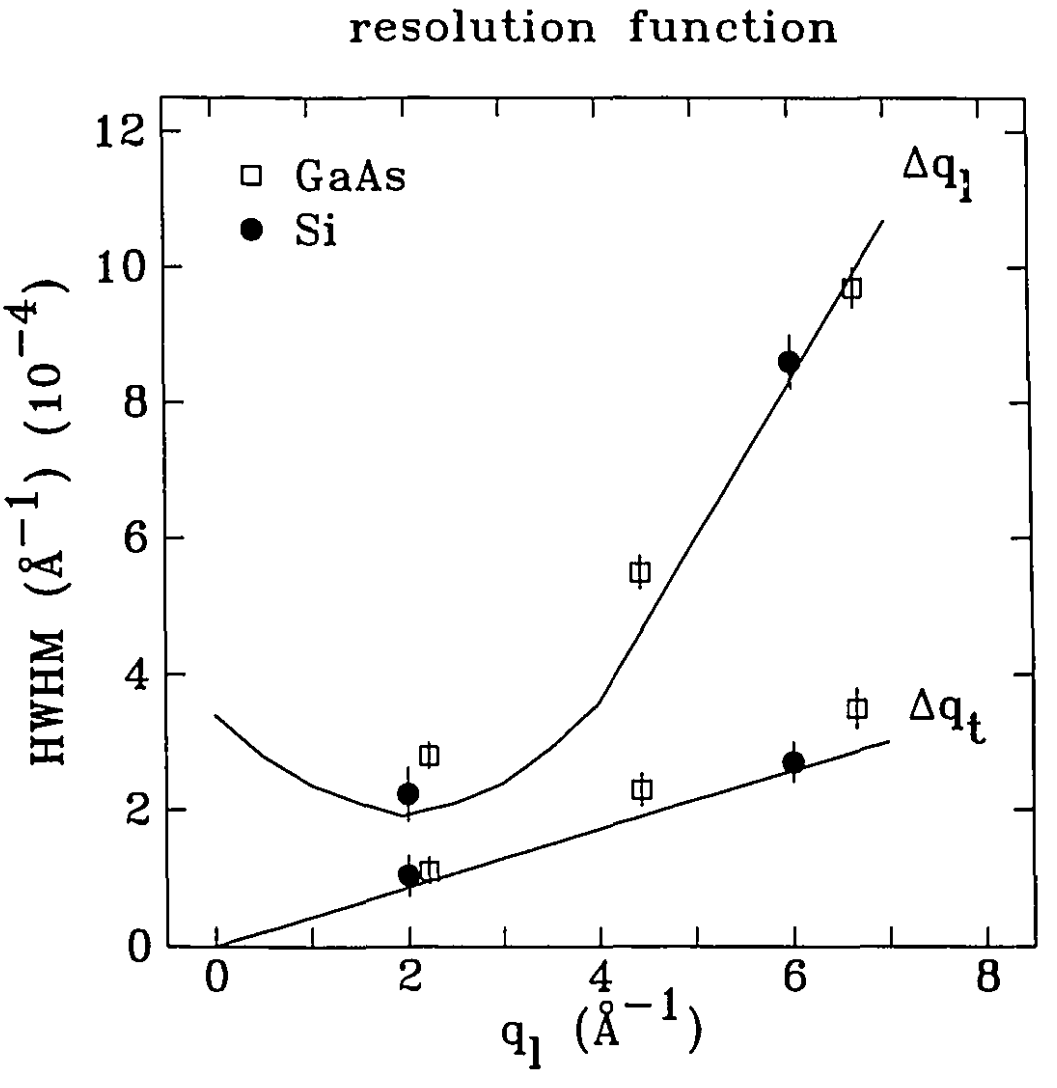

Figure 3.6: The resolution function of a triple-axis x-ray diffractometer with Ge(111) monochromator and analyzer. The solid curves are calculated with Cowley's formula. The data points are collected from (002), (004) and (006) reflection of a perfect GaAs crystal, and from (111) and (333) of a perfect Si crystal.

described in Section 3.4.

Since the detector can only move in the scattering plane by the 2θ circle of the goniometer and the direction of the incident beam is fixed in the laboratory frame, the scattering vector, q, is principally confined to the scattering plane as determined by the setup. The relation between the angular position of the detector 2θ and q_l is given by

$$q_l = 2ksin\left(\frac{2\theta}{2}\right). \tag{3.19}$$

The orientation of the sample is determined by the three Euler angles $[\omega, \chi, \phi]$, and among them the angular coordinate ω is coupled to the θ and 2θ circles via

$$\omega = \theta - \frac{2\theta}{2}. \tag{3.20}$$

A rotation matrix $R(\omega, \chi, \phi)$ is programmed according to Busing and Levy's original work [123] to map the diffractometer frame $[q_l, q_t, q_v]$ onto the laboratory frame with the constraints indicated by Eq 3.19 and Eq 3.20. An orientation matrix, U has also been programmed to map the crystal reference frame $[q_x, q_y, q_z]$ onto the diffractometer reference frame with the constraints determined by the geometrical and structural features of the sample.

Based on the geometrical features of the samples and our diffractometer, the experimental measurement will be discussed from two aspects. Normal scattering is mainly used to measure the out-of-plane structure and glancing incidence scattering is mainly used to measure the in-plane structure. We combine the normal Bragg scattering and reflectivity measurement as one technique, *i.e.*, normal scattering, because the sample under study only needs to be aligned once in our diffractometer and this combination can be used to measure the surface miscut angle accurately, which is crucial for the geometry of glancing incidence x-ray scattering.

3.2.2 Normal Scattering

There are two reasons to define this technique as normal scattering: 1) in the experiment the surface normal of the sample is first aligned in the scattering plane, as shown in Figure 3.3 (a); 2) it is basically the normal or conventional technique used for x-ray scattering. Bragg scattering is a well known technique and has been commonly used to measure the out-of-plane structure of the epilayer, its strain or structural relaxation along the crystal axis z. Because Bragg scattering probes the lattice spacing on the atomic scale, the value of q_l usually runs between 2Å^{-1} and 7Å^{-1} for semiconductor crystals. With the same alignment, q_l can be set to very small value to measure the reflectivity of the sample. Because q_l is small, it is only sensitive to the large scale electronic density change along the surface normal of the sample. Combining the techniques of normal Bragg scattering and reflectivity measurement as one, we are able to obtain some useful information of the sample, such as surface miscut. This also makes it easy to account for the geometrical and optical corrections needed for high resolution work.

As mentioned in last subsection, x-ray scattering is confined to the scattering plane. The technical procedure of normal scattering is to first align the q_z axis of the sample reference frame with the q_l axis of the diffractometer reference frame. This is realized by locating a Bragg peak of the substrate crystal along the z axis, say, the (004) peak of GaAs. The optimization of this peak by rocking all circles of the diffractometer provides the first reference vector of the orientation matrix U. The alignment of the q_x axis of the sample into the scattering plane can be achieved by means of telescope. It is usual to find at least one (110) cleavage edge in a GaAs crystal, which can be defined as the q_x axis. The optimization of the (220) Bragg peak of GaAs provides the second reference vector for the orientation matrix U. A horizontal translation of the sample is usually needed to make sure that the x-rays illuminate the desired area of the sample. The data in normal scattering is normally

collected with zone mode [123]. This mode can be regarded as two-circle goniometry with circles χ and ϕ fixed at certain values which are often defined as zero.

Bragg scattering is carried out at large q_l, and reflectivity measurement is carried out at small q_l. The specular reflection usually occurs when q_l agrees to the surface normal of the sample, which may not be along the q_z axis of the crystal reference due to the surface miscut, as shown in Figure 3.7. The projection of miscut angle of the sample in the x-z plane can be accurately determined by the offset of Bragg scattering and specular reflection. This measurement requires accurate beam alignment. The horizontal width of Slit 3, as shown in Figure 3.3, is usually used to define the cross-section of this incident x-ray beam. The sample is aligned to block half of the incident beam when its surface is parallel with the incident beam and the detector is set at arm-zero, *i.e.*, $2\theta = 0$. When q_l is small, the geometrical and optical effects due to the sizes of the incident beam and the sample are important. These corrections will be discussed in detail in Section 3.4. Under this alignment, the non-specular reflectivity at small q_l, and off Bragg scattering at larger q_l can also be studied with transverse scans along q_t or q_v.

By the same technique, normal Bragg scattering and reflectivity measurement can be carried out in the y-z plane of the sample (as opposed to x-z plane). This is realized principally by rotating the sample 90° about the z axis. This can be usually done by means of an appropriate combination of ω, χ, and ϕ rotations. It occurs very often that the structure of the epilayer is different along x and y, as discussed in Section 2.2. Only after the projections of the miscut angle on the axes, x and y are accurately measured, can the sample reference frame of coordinates be defined. In glancing incidence x-ray scattering of miscut surface, there is a quadrant of the sample in which the x-rays can enter and exit with less absorption that in other quadrants. This quandrant is called the preferential quadrant and selected as the one which the surface normal of the sample inclines to.

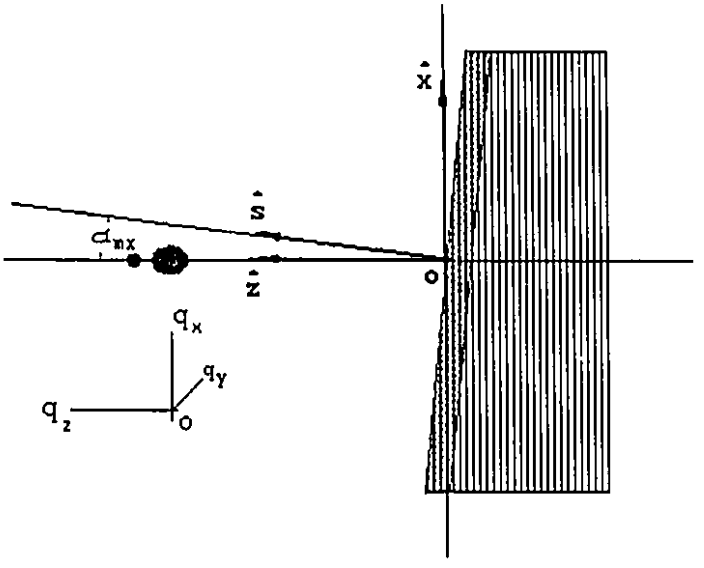

Figure 3.7: The sample with miscut surface. The reference coordinate system is defined by the principal Bragg peaks of the substrate, and the x-z component of miscut angle, α_{mx}, is determined by the out-of-plane Bragg scattering and surface specular reflection. The small and large spots along q_z are the Bragg spots of the substrate and the epilayer respectively. The vector $\hat{\mathbf{s}}$ is the surface normal and peaks with specular reflection.

3.2.3 Glancing Incidence Scattering

The aim of glancing incident x-ray scattering is measuring the in-plane structure of the epilayer and epitaxial interface. This is often difficult to be measured by other techniques. As shown in Figure 3.3 (a) and Figure 3.8, the essential feature of this technique is to bring the x-y plane of the sample's reference frame into the scattering plane of the diffractometer and keep the surface of the sample under the condition of specular reflection, *i.e.*, $\alpha_h = \alpha_i$.

The first question is how to align the sample. The surface normal of the sample has to be aligned with the main axis of the diffractometer. This alignment can be achieved by means of a laser beam. The reflected spot of the laser beam should not move with rotation of the sample around the main axis of the diffractometer when the sample is aligned. The slits can be used to align the cleavage edge of the sample to be parallel to the incident x-ray beam. The position of the sample is denoted by $[\omega_0,\ \chi_0,\ \phi_0]$, which can be directly read from the diffractometer. The preferential quadrant of the sample is aligned into the first quadrant of the reference coordinate frame of the diffractometer. Some manual adjustment of the sample holder can set the initial Euler triple $[\omega_0,\ \chi_0\ \phi_0]$ to be [0,0,0].

The first reference vector of the orientation matrix U is defined by locating the principal in-plane Bragg peak of the substrate, say GaAs (220) with a small positive χ. The value of χ roughly equals the sum of the critical angle of the material of the sample and the projection of the surface miscut on the plane defined by the momentum transfer q and the main axis of the diffractometer. Since the in-plane Bragg peak is actually a rod along the surface normal, and it is less sensitive to χ than to other angles. The out-of-plane component and in-plane component of the x-ray momentum transfer q are related through the angle χ,

$$q_s = q_l \cdot tan\chi. \tag{3.21}$$

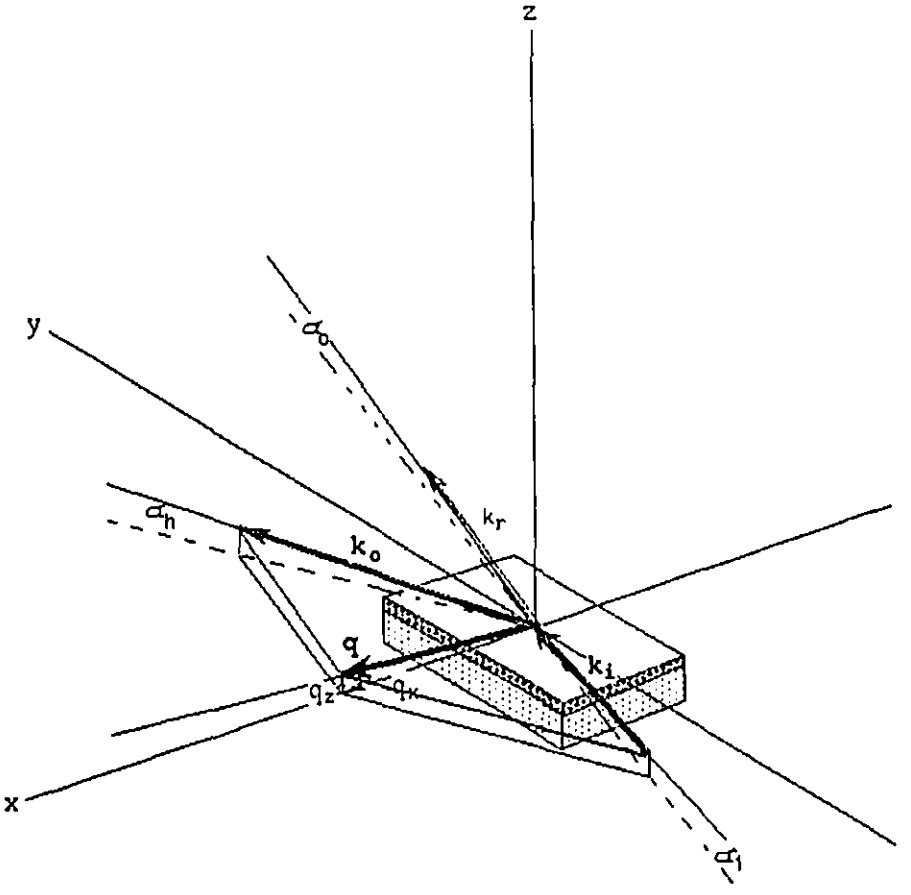

Figure 3.8: Glancing incidence scattering. The three angles a_i, a_o and a_h denote the angles between the surface of the sample and the incident, reflect and reflected-diffract x-ray beams respectively.

A scan along q_z can be used to optimize the signal. Since the projection of miscut angle, denoted as α_{mx}, has already been accurately measured in normal scattering, the real position of the first principal in-plane peak is well defined. It may not be centered at the maximum of the Bragg streak due to the glancing incident footprint correction which will be discussed later.

The azimuth mode of the four-circle goniometry [123] is specially useful in data collection of glancing incidence scattering. Taking the surface normal of the sample as the azimuth reference vector at 90°, the condition of specular reflection is constrained during scans. In this case, the angle between the incident beam and the sample surface, α_i, is given by

$$sin\alpha_i = sin\chi sin\theta_B = sin\alpha_h, \tag{3.22}$$

where θ_B is the Bragg angle of the in-plane peak, and α_h is the exit angle of scattered x-rays.

The sample coordinate system is usually defined by the crystallographic axes of the substrate, as mentioned in Section 3.1. For GaAs (001) substrate, $\langle 001 \rangle$ is naturally selected as z-axis and $\langle 110 \rangle$ is usually selected as x-axis. The y axis of this coordinate system must be $\langle 1\bar{1}0 \rangle$. In the geometry of glancing incidence scattering, when the first reference vector of orientation matrix U has been defined with GaAs (220) peak, the second reference vector of U is the azimuth reference vector $\mathbf{A} = [A_x, A_y, A_z]$. The components of vector A are defined by

$$\begin{aligned} A_x &= [tan(\alpha_{mx}) + tan(\alpha_{my})]/2|A|, \\ A_y &= [tan(\alpha_{mx}) - tan(\alpha_{my})]/2|A|, \\ A_z &= 1/|A|, \end{aligned} \tag{3.23}$$

where

$$|A| = \sqrt{[tan(\alpha_{mx}) + tan(\alpha_{my})]^2/4 + [tan(\alpha_{mx}) - tan(\alpha_{my})]^2/4 + 1}.$$

In principle, another in-plane peak, say GaAs $(2\bar{2}0)$, should be easily found by a rotation of $\omega = 90°$ in azimuth mode and about the reference vector **A**. Similar as the (220) peak, the glancing incident reflection and footprint correction must be taken into account in data treatment.

As mentioned in Section 3.1, the penetration depth of x-rays is determined by the out-of-plane component of x-ray momentum transfer which depends on the incident and exit angles of the x-ray beam. By controlling the penetration depth in glancing incidence x-ray scattering, the evolution of in-plane structure from the epitaxial interface to the top surface of the epilayer can be studied. If the surface miscut is small, the in-plane depth profiling can be taken along the scattering rod, *i.e.*, along q_z, with corresponding geometrical correction in fitting of the in-plane Bragg peak positions. If the in-plane depth profiling is taken along the axis q_z, the corresponding corrections to the intensities of the peaks should be made because of the misalignment of the scattering rod.

3.3 X-ray Source

The x-rays are generated by a 2.2 kW Cu-anode x-ray tube (Philips, Type 2273/20). With point focusing, x-rays can be regarded as emitted from a spot on the center of the anode. The size of this spot as viewed along the x-ray beam is $1.2mm \times 0.4mm$ and illustrated in Figure 3.9. The divergence of the primary beam in the scattering plane is principally determined by the monochromator crystal, which can be estimated as 0.0036°, i.e., the Darwin width of Ge (111) reflection with Cu-$K_{\alpha 1}$ emission line in this set-up. The out-of-plane (scattering plane) beam divergence is about 1°, which is principally determined by the slits. The cross-section of the primary incident beam is about $1.0mm \times 4.0mm$ as shown in Figure 3.9. The in-plane and out-of-plane intensity distributions were measured by scanning Slit 3

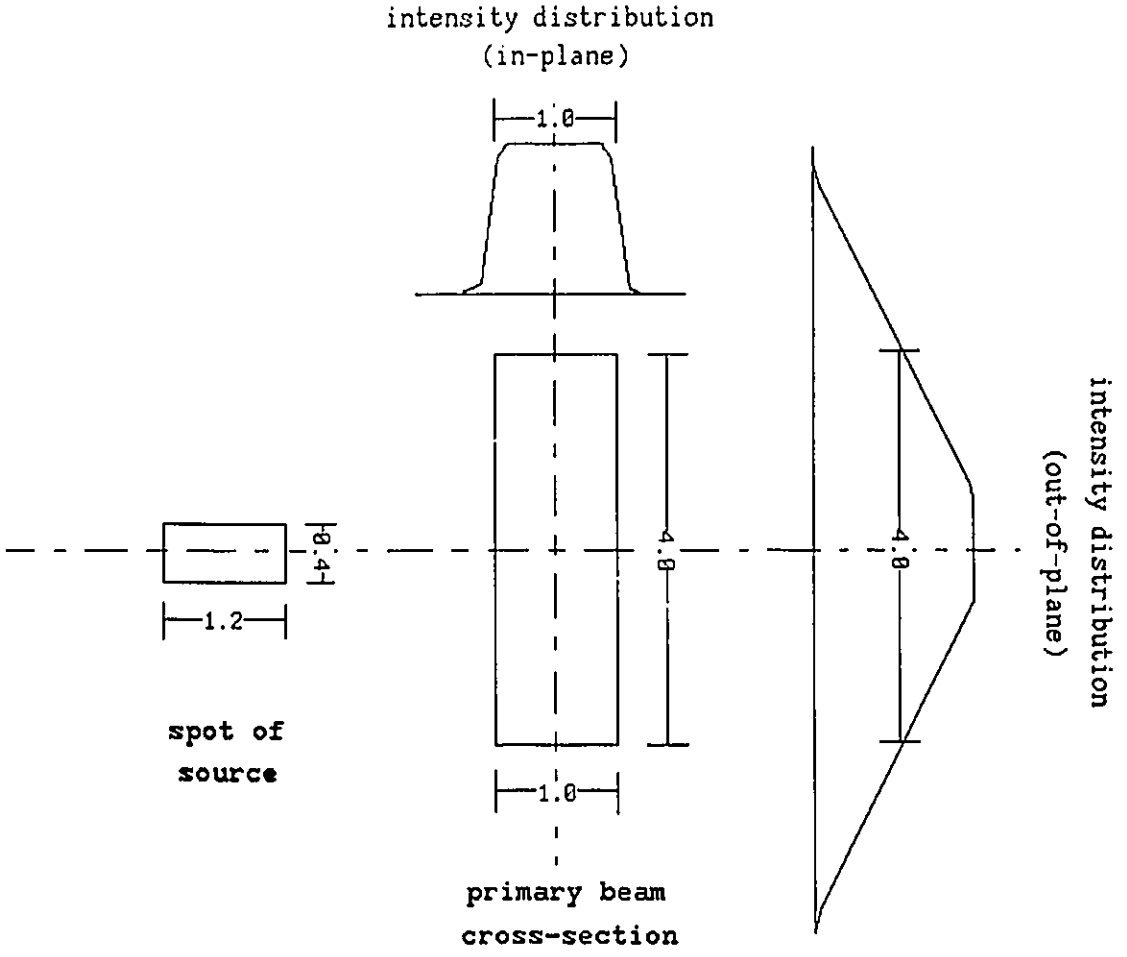

Figure 3.9: The intensity distribution of $K_{\alpha 1}$ emission line. The intensity distribution of the primary beam is measured by scanning Slit 3 horizontally and vertically. The horizontal line represents the scattering plane. The full widths at half maximum of Slit 3 scans are used to define the cross-section of the incident primary beam, which is $1.0 \times 4.0 mm^2$ in our experiment.

cross the beam, and the FWHM (Full Width at Half Maximum) values are used to define the beam size. These numbers agree with the width of lead stop before the monochromator crystal (1.0 mm) in horizontal and the window of Slit 1 ($2.0mm \times 4.0mm$) in vertical with small divergence corrections.

As shown in Figure 3.9, in the scattering plane, the x-rays are basically uniformly distributed. The intensity of the incident beam increases linearly with the horizontal width of Slit 3 up to 1.0 mm. The cross section and intensity are controlled by Slit 3, which is important for making a geometrical correction in data analysis, specially in the case of small q scattering. Slit 3 is left wide open, say 2.0 mm horizontally, for large q scattering to eliminate slit effects on the shape of the beam. All the slits are symmetrically centered with respect to the beam. The vertical width of Slit 3 is usually set to 2.0 mm in normal Bragg scattering, and 1.0 mm in glancing incidence scattering, which keeps the intensity uniformly distributed across the beam out-of-plane.

The x-ray spectrum of the incident beam is selected by the Bragg reflection of monochromator crystal from the spectrum generated by the x-ray tube [118]. In most cases of structural analysis, the Cu-K_α characteristic line is used principally because of its strongest intensity. As shown in Figure 3.10, the spectrum of incident beam peaks at three wavelengths, $K_{\alpha 1}$, $K_{\alpha 2}$ and $K_{\alpha 3}$. This spectrum is measured by scanning the detector (2θ scans) cross the primary incident beam with monochromator and analyzer crystals aligned in the experimental condition. The three wavelength dispersion peaks are completely Lorentzians as all the slits are essentially wide open in the scattering plane. The parameters of this beam are given in Table 3.3. The intensities in the table have been scaled to the intensity of $K_{\alpha 1}$. The absolute intensity of x-rays is determined by the power setting of the generator. The x-ray photon intensity of $K_{\alpha 1}$ emission illuminated on the sample is 3×10^5 photons $/sec \cdot mm^2$ under the tube power of $40kV \times 40mA$ at the maximum.

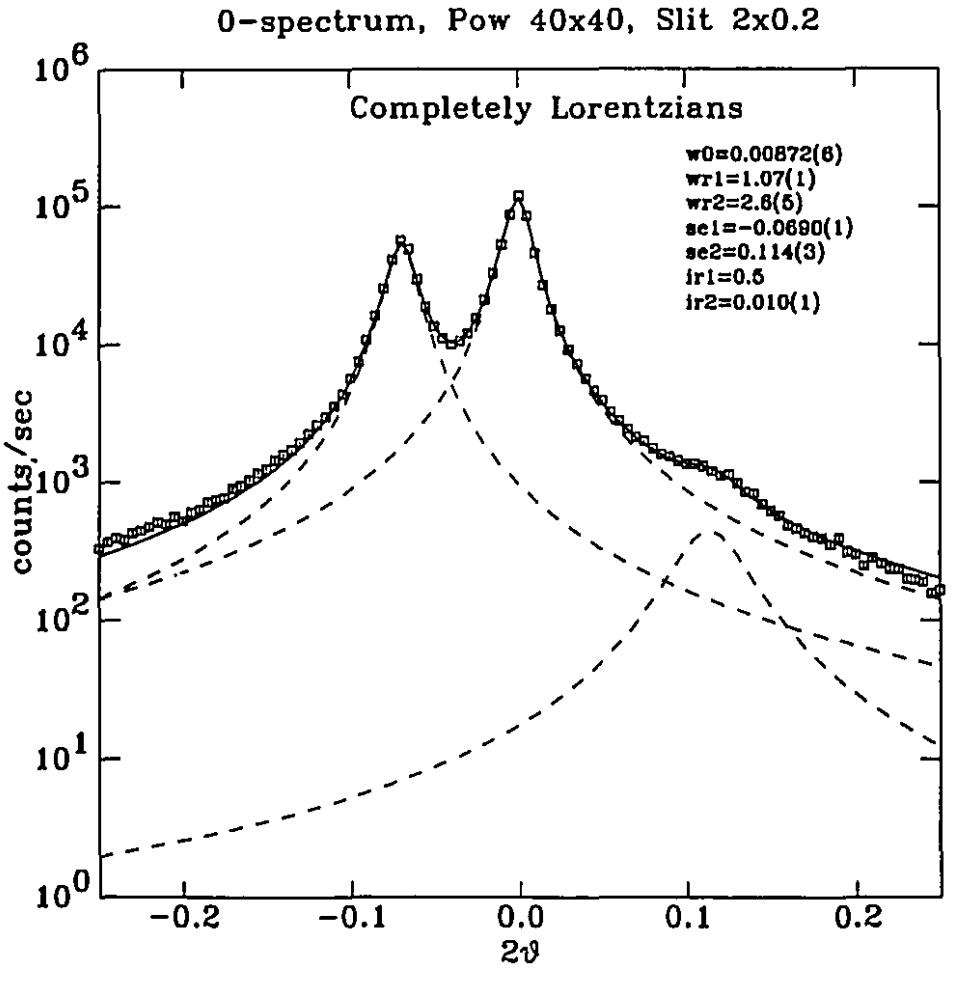

Figure 3.10: The wavelength distribution of the primary incident beam, measured by 2θ scan at arm-zero with only monochromator and analyzer in (+,0,+) triple-crystal configuration. The x-ray photon peak intensity of $K_{\alpha 1}$ emission line illuminated on t' ample is 3×10^5 photons / $sec \cdot mm^2$ when the tube power is set at $40kV \times 40mA$.

If the widths of these peaks are also scaled to $K_{\alpha 1}$ line, the widths are 1.0, 1.07, and 2.65, for $K_{\alpha 1}$, $K_{\alpha 2}$, and $K_{\alpha 3}$ lines respectively. The $K_{\alpha 3}$ line seen here is actually an average of a group of transitions called non-diagram lines [18]. These numbers can be used as fixed parameters in data analysis.

	$\lambda(\AA)$	2θ	I	HWHM
$K_{\alpha 1}$	1.54051	0.0	1.0	0.00872(6)
$K_{\alpha 2}$	1.54433	−0.0690(1)	0.5(0)	0.00933(8)
$K_{\alpha 3}$	1.53420	0.114(3)	0.010(1)	0.0226(3)

The angular separations of peaks of $K_{\alpha 1}$, $K_{\alpha 2}$, and $K_{\alpha 3}$ lines change with q due to the dispersion of x-rays with different wavelengths. A simple formula can be used to calculate the separation, which can be written as

$$\Delta\theta = \frac{\lambda_{\alpha i} - \lambda_{\alpha 1}}{\lambda_{\alpha 1}} |tan\theta_s - tan\theta_m| \tag{3.24}$$

where θ_s is the Bragg angle of sample and θ_m is the Bragg angle of monochromator crystal which equals to 13.665° for Ge(111) reflection of $K_{\alpha 1}$ line. The wavelength $\lambda_{\alpha i}$ can be either the $K_{\alpha 2}$ line or $K_{\alpha 3}$ line. In data fitting, a small correction may be needed for these parameters to compensate for the angular separation of $K_{\alpha 2}$ and $K_{\alpha 3}$. These corrections can be well determined by fitting the scattering from the Bragg peaks of the substrates which are often resolution limited. The polarization coefficient of the x-ray beam is, $\gamma = 0.623$, and includes polarization effects of both the monochromator and analyzer.

3.4 Data Collection and Treatment

As discussed in Chapter 2, heteroepitaxy is a complex system which may contain more than one set of atomic ordering and present more than one length scale of structures. The x-ray scattering pattern of heteroepitaxy can be quite complicated, specially with an x-ray source of more than one wavelengths and with a diffractometer of more than one elements of scattering, as described in the last two sections of this chapter. To extract the useful information effectively, the methods and techniques of data collection and treatment are important.

Equation 3.5 indicates that the scattered x-ray photons from an ordered system are principally localized at Bragg peaks in q-space. The positions, shapes and integrated intensities of these Bragg peaks provide us direct information of the atomic arrangement of the system. For a perfect crystal, the Bragg peaks are periodically distributed in q-space, and their periods are just reciprocally proportional to the lattice constants of the crystal. The shapes of these Bragg peaks can usually be well fit to Lorentzian distributions, as shown in Figure 3.10, and their widths often reflect the resolution function of the instrument, as shown in Figure 3.6. Their absolute integrated intensities can also be accurately evaluated, as indicated by Equation 3.6. As illustrated by Figure 3.11, the substrates used for epitaxial growth are usually perfect crystals and their Bragg peaks construct a natural reference frame in q-space and guide the data collection and treatment.

The crystallographic axes of the substrate is usually defined by convention. For example, GaAs crystals has zinc blende structure, and the three axes ⟨100⟩, ⟨010⟩ and ⟨001⟩ construct a Cartesian coordinate system. If the epitaxial growth direction is along one of these axes, it can be easily defined as ⟨001⟩ axis, or axis z, and called the out-of-plane axis. The other two crystallographic axes of this system are defined as x and y axes, and called as in-plane axes. In heteroepitaxy, the structure of

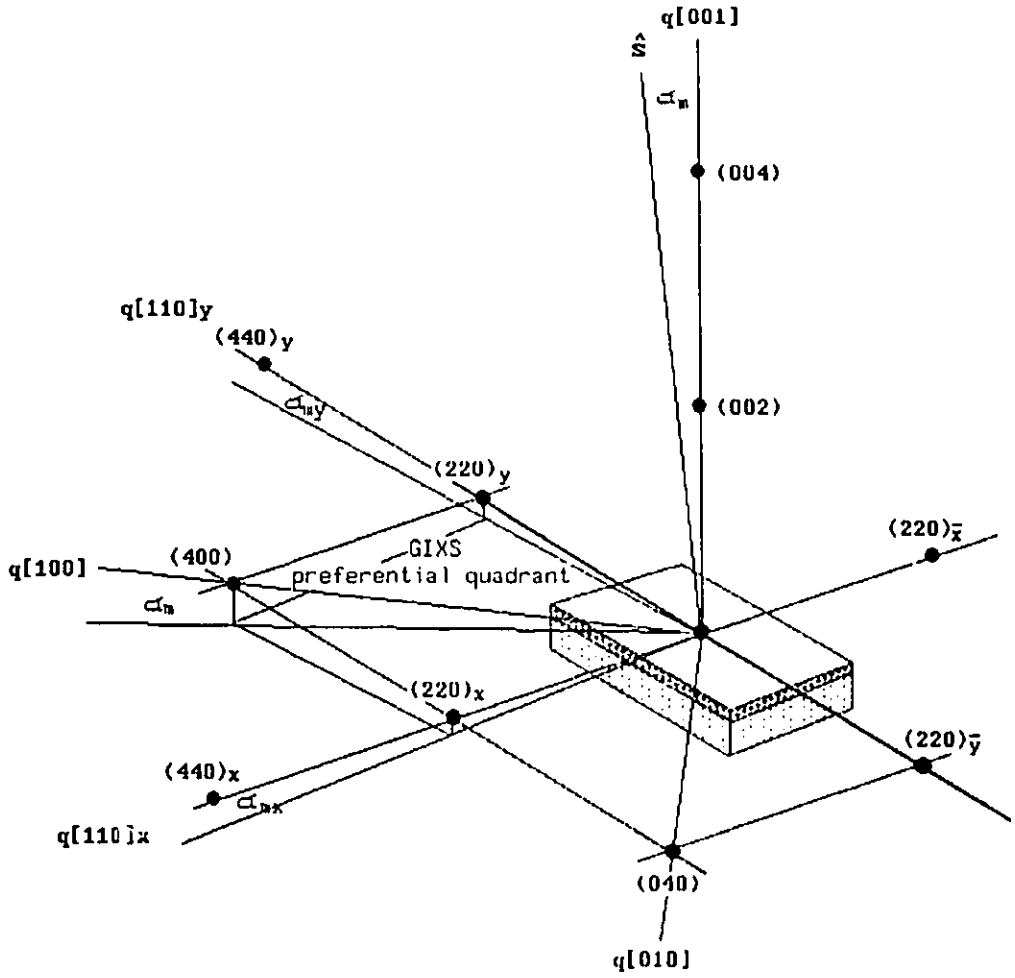

Figure 3.11: Reference coordinates system. The reference coordinate system is defined by the reciprocal lattice of the substrate crystal and determined by the principal out-of-plane and in-plane Bragg scattering of the substrate. The surface miscut makes a preferential quadrant for glancing incidence x-ray scattering, in which the x-rays are less absorbed than in any other quadrant. This preferential quadrant is defined as the first quadrant in our reference coordinate system and flanked by q[110]x and q[110]y axes in our measurements.

the substrate is only a reference, and is not the subject we are going to study. A reference coordinate system having better coupling with the microstructure of the epilayer and the epitaxial interface and with the techniques of data collection may need to be constructed on the base of the conventional crystallographic coordinate system of the substrate. Since the (110) plane is the cleavage plane of GaAs crystal and the $\langle 110 \rangle$ axis bears more features of microstructure of III-V heteroepitaxy, the axes of $\langle 110 \rangle$, $\langle 1\bar{1}0 \rangle$ and $\langle 001 \rangle$ of the substrate are used to construct a orthogonal reference coordinate system in our structural studies.

A problem of ambiguity can arise if there are more than one epilayer of the same epitaxial system under investigation. The epitaxial interface of III-V heterostructure has only a two-fold symmetry with respect to the chemical bonding, and the asymmetrical bonding strength at the interface can cause asymmetric structural properties of the epilayers. Based on this, the $\langle 110 \rangle$ axis and $\langle 1\bar{1}0 \rangle$ can be absolutely defined for GaAs. Given a crystal, it is usually not easy to distinguish $\langle 110 \rangle$ axis and $\langle 1\bar{1}0 \rangle$ axis. To avoid potential misleading data interpretation, we define the two in-plane orthogonal $\langle 110 \rangle$ axes as $\langle 110 \rangle_x$ and $\langle 110 \rangle_y$, which construct a right-hand screw orthogonal coordinate system with axis $\langle 001 \rangle$.

In q-space, the three components of the momentum transfer $\mathbf{q}$ in the new coordinate system are denoted as $q[110]x$, $q[110]y$ and $q[001]$ respectively. For easier geometrical setting in data collection and easier comparison of data collected in different axes, the value of the q-component is scaled to the fundamental translational unit of this axis. Therefore, the unit along $q[001]$ axis is Å^{-1}, while the unit along $q[110]x$ axis or $q[110]y$ axis is $\sqrt{2}\text{Å}^{-1}$. For example, the (004) peak of the GaAs crystal is located at $4.446[001]\text{Å}^{-1}$ in q-space, and $(440)_x$ peak is located at $4.446[110]_x\text{Å}^{-1}$ which equals 6.288Å^{-1}. The value of q used to indicated the position of Bragg peak is the momentum transfer of Cu-$K_{\alpha 1}$ line.

As discussed in the second section of this chapter, the data are collected with

normal scattering and glancing incidence scattering. In normal scattering data on the out-of-plane structure and the surface and interface morphologies are collected, and in glancing incidence scattering data on the in-plane structure are collected. Because our structural study of heteroepitaxy requires an analysis the shapes of the Bragg peaks, one dimensional scans along the three axes of q-space, and two dimensional meshs in defined q planes are carried out to present the data, and will be discussed in detail in the next chapter. As mentioned in Section 3.2.1, the resolutions are different along different axes in the reference coordinate system of the diffractometer. The coupling between the sample coordinate system $[q_x, q_y, q_z]$ and $[q_l, q_t, q_v]$ is determined by the orientation matrix U and various constraints, which has also been discussed in Section 2 of this chapter.

Our structural analysis has focused on the study of Bragg peaks. The formation of intensity maximums, *i.e.*, Bragg peaks, in scattering pattern is first due to the coherent summation of ordered scatterers, as indicated by Equation 3.5. For a one dimensional ordered atoms in a chain, the x-ray scattering pattern has the form $\frac{\sin^2(q_x a_x N/2)}{\sin^2(q_x a_x/2)}$, where N is the number of atoms and a_x is the distance between atoms [23]. A single intensity maximum of scattering can be approximated by a Gaussian curve with errors smaller than 10% for the integrated intensity and 5% for the width of the peak. These errors are mainly due to the intensity wiggles of coherent summation which are not presented by the Gaussian curve. If the atomic ordering is perturbated by fluctuation, a random process over time and/or space, and the scattering pattern is superposed by the incoherent summation of coherent regions, as indicated by Equation 3.6, the wiggles are smeared out and errors are reduced. Another effect on the shape of the scattering maximum is the x-ray emission line, which has an intrinsic intensity distribution [18]. This distribution can be fit to a Lorentzian distribution, as shown in Figure 3.10. Even though many elements of scattering may be involved in the formation of Bragg peaks, as indicated by Equa-

tion 3.17 and Equation 3.18, their shape can be fit to a combination of Gaussian and Lorentzian distributions.

Wertheim and colleagues has shown that fitting the Voigt line shape by the linear combination of Gaussian and Lorentzian curves of equal widths (EWGL) can be accurate to about 1% [124]. The Voigt line shape is a convolution integration of Gaussian and Lorentzian distributions [125], which bears the essential feature of x-ray scattering, as described by Equation 3.17 and Equation 3.18. With least-squares arithmetic [126], the Bragg peak of scattering pattern has been fit to the curve

$$f_0(\Gamma,\eta,q,q_0) = \frac{1-\eta}{\pi}\frac{\Gamma^2}{\Gamma^2+(q-q_0)^2} + \eta\sqrt{\frac{ln2}{\pi}}exp\left[-\left(\frac{q-q_0}{\Gamma}\right)^2 ln2\right], \qquad (3.25)$$

where Γ is the half width at half maximum (HWHM) of the peak and η is the Gaussian fraction. Wertheim *et al.* present curves which relate Γ and η to underlying parameters of the Gaussian and Lorentzian in the convolution. This lineshape conveniently allows for the adjustment of the scattering in the center to the tails, and called a EWGL curve in this thesis.

The function $f_0(\Gamma,\eta,q,q_0)$ can be very effectively used to fit the width, Γ, the position q_0 of the Bragg peak, as well as the fraction of statistical effect η, for a well monochromated x-ray incident beam. This well monochromated x-ray incident beam can be regarded as $K_{\alpha 1}$ emission line in our experiment. Because the x-rays of different wavelengths are not coherent, and the superposition of the scattering patterns produced by x-rays of different wavelength can be linearly treated as

$$\begin{aligned} f(\Gamma,\eta,q,q_0) &= f_0(\Gamma,\eta,q,q_0) \qquad (3.26)\\ &+ \gamma_2 f_0(w_2\Gamma,\eta,q,(q_0+\Delta q_2)) + \gamma_3 f_0(w_3\Gamma,\eta,q,(q_0+\Delta q_3)), \end{aligned}$$

where γ_2 and γ_3 are the intensity ratios of $K_{\alpha 2}$ and $K_{\alpha 3}$ lines to $K_{\alpha 1}$ lines respectively, and w_2 and w_3 are the width ratios, as given in the table of Section 3.3. The variables of Δq_2 and Δq_3 are the peaks separations produced by $K_{\alpha 2}$ and $K_{\alpha 3}$ lines from that

produced by $K_{\alpha 1}$ line, which can be evaluated with Equation 3.24. The value of η is assumed not to change with the characteristic wavelengths of the x-ray tube, is a number between 0 and 1. The arm-zero spectrum of x-ray primary incident beam as shown Figure 3.10 demonstrates a good example, in which $\eta = 0$.

As indicated by Equation 3.17 and Equation 3.18, the slits can affect the x-ray scattering pattern. In order to eliminate the effects of slits, all the horizontal slits have been set open when the data are collected at large q_l, provided that the primary incident beam is symmetrically distributed, as shown in Figure 3.10. In actuality, the slits have little effects if their horizontal widths are larger than that of the incident x-ray beam, which is $1mm$ in our setup. With only the effect of scattering from the crystals, the Bragg peaks can be easily fit to the curve indicated by Equation 3.25 and Equation 3.27. However, slits are always involved. They can be due to the finite size of the sample, the window of the detector, as well as the geometrical configuration of monochromator and analyzer crystals.

Figure 3.12 shows two curves of the arm-zero spectrum of the incident x-ray beam under the same power setting, but with different slit widths of Slit 3 (refer to Figure 3.3). The intensity distribution of the incident beam is basically uniform, and the number of photons counted at arm-zero is proportional to the cross-section of the beam, which is determined by the window of slits. Comparing with the curve collected with wide open horizontal slit ($2.0mm$), the principal change of the curve taken with narrow slit width ($0.4mm$) is the counts at the two shoulders. This shape of the curve suggests for us to use a compatible function to take care of it. As indicated by Equation 3.17, the slits effect is convolutionally involved in the integration of scattering pattern. By means of the same technique used in combining the Gaussian and Lorentzian, we deal with the effect of the slits with another EWGL curve of considerable larger width and much smaller intensity, as show in Figure 3.12. Therefore, the fitting curve of the x-ray scattering is merely

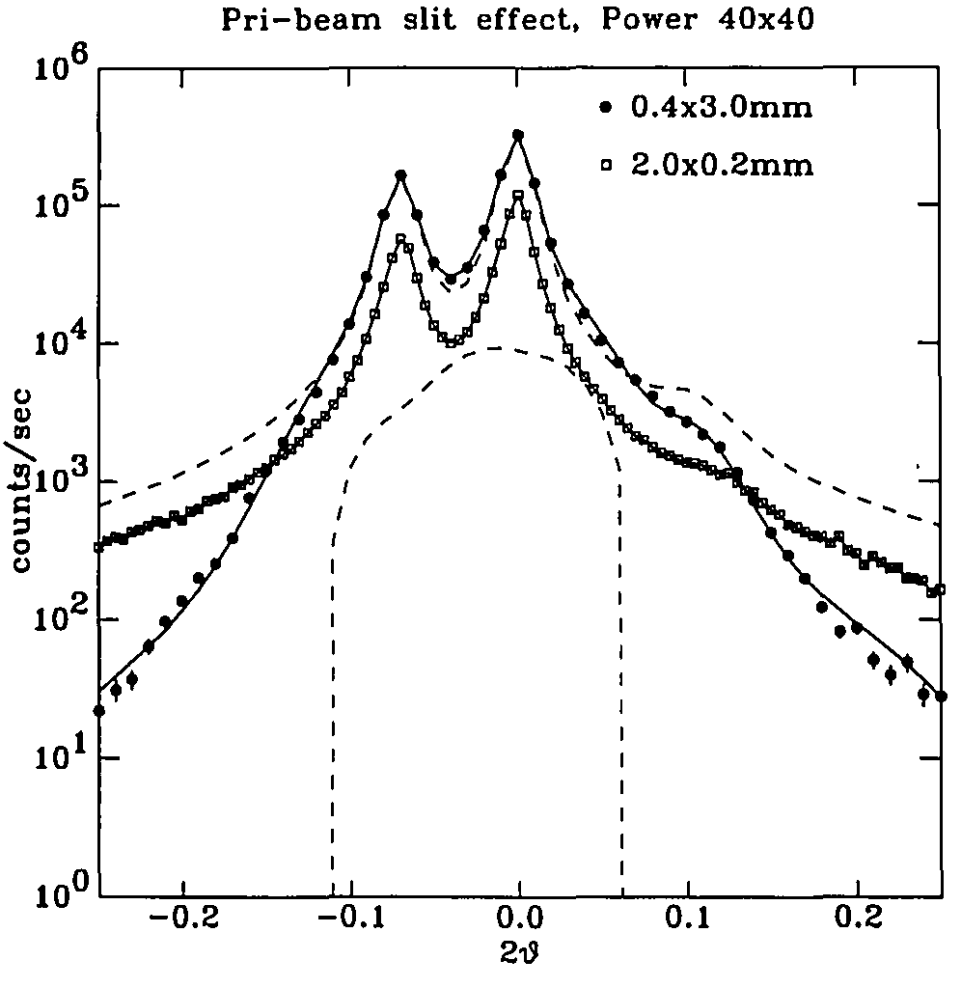

Figure 3.12: The slits effect. The width of slit changes the profile of the primary incident beam. This effect may be accounted for by adding another EWGL curve in data fitting, which is usually with much bigger peak widths and much smaller intensity. The curve with open square points is the same curve shown in Figure 3.10. The parameters used to treat the slit effect are $W_D = 0.086°, r_D = 0.11$, and $\eta_D = 1.17$.

a weighted summation of two spectrum curves indicated by Equation 3.27 at the same position in q-space, in the case that the slits need to be accounted for in data treatment. This fitting curve may be written as

$$f_{fit}(\Gamma, \eta, q, q_0) = f(\Gamma, \eta, q, q_0) + r_D \cdot f(W_D, \eta_D, q, q_0), \tag{3.27}$$

where W_D, r_D, η_D are the width, intensity ratio and Gaussian fraction of the curve for the slit effect. The value of W_D relates to the width of slits and usually more than one order broader than the scattering peak of the sample, Γ. The value of r_D is usually smaller than 0.1. The value of η_D can be between 0.95 and 1.20. The more than unity value of Gaussian fraction implies the subtraction of a Lorentzian from the curve to take care of the lost scattering at the shoulders, as shown in Figure 3.12. Equation 3.27 is a simple way to treat the slit effect, which may not be mathematically rigorous and should be used with caution. In the case that the slit effect must be accounted for, W_D, r_D and η_D can be obtained by fitting the Bragg peaks of the substrate, and then used as fixed parameters to fit the scattering of the epilayer nearby in q-space. The parameters used in fitting the arm-zero spectrum with slit widths of $0.4 \times 3.0mm$, as shown in Figure 3.12, are $W_D = 0.086°, r_D = 0.11$, and $\eta_D = 1.17$. It can also be seen in Figure 3.12 that the slit effect may slightly increase the widths of the real scattering peaks, *i.e.*, the sharper peaks. It seems that the slit effect should be possibly avoided in data collection for high resolution structural work. However, as shown in the same figure, the depression of scattering at the tails of Bragg peaks by using slits can also increase the resolution in some cases.

Since the x-ray scattering pattern with small q_l is not sensitive to the structure at the atomic scale, the reflectivity is simply fit to the Fresnel curve multiplied by a Debye-Waller factor, as indicated by Equation 3.15. The polarization effect of the incident x-ray beam can be ignored. Similar to the effect of slits for the data collection with large q_l scans, there is an instrumental correction for collecting

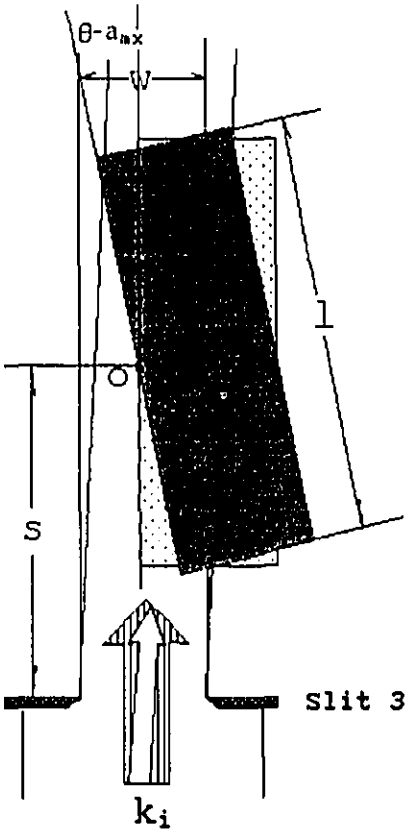

Figure 3.13: Footprint Correction. The sample is only illuminated by part of the x-ray beam when the incident angle is very small. The vector $\mathbf{K_i}$ denotes the wavevector of the incident x-ray beam. The big arrow denotes the $K_{\alpha 1}$ line, which is aligned symmetrically in-plane at arm-zero. The small arrow denotes the $K_{\alpha 2}$ line, which has only half intensity of $K_{\alpha 1}$ line and an angular and a translational offset with respect to the center of the diffractometer.

data with small q_l scans. It is called the footprint correction and illustrated by Figure 3.13. When the x-rays incident with a glancing angle at the sample surface, only part of the beam is reflected by the sample. The reflected photon counts are reduced because less incident x-ray photons hit the sample. If the intensity of the incident x-rays are uniformly distributed across the horizontal width of Slit 3, as shown in Figure 3.13, Figure 3.3 and Figure 3.9, the factor of footprint correction P_{f1} for $K_{\alpha 1}$ emission line of the x-ray source is given by

$$\begin{aligned} P_{f1} &= \frac{L_x}{w} sin(\theta - \alpha_{mx}), \qquad if \;\; \theta \leq sin^{-1}\frac{w}{L_x} + \alpha_{mx}, \\ P_{f1} &= 1, \qquad otherwise, \end{aligned} \tag{3.28}$$

where L_x is the lateral length of the sample along axis x, w is the horizontal width of the incident x-ray beam as defined by Slit 3, and α_{mx} is the projection of surface miscut angle on the x-z plane. The Equation 3.28 works the same way for the y direction if the sample is rotated along z axis by 90°, provided that the subscript x in the equation has been substituted by y.

As described in Section 3.3, the $K_{\alpha 2}$ emission line of the x-ray source has half of the intensity of the $K_{\alpha 1}$ line and peaks with an angular separation $\Delta 2\theta$ = 0.069° to the $K_{\alpha 1}$ at arm-zero. Because the difference of wavelengths between $K_{\alpha 1}$ line and $K_{\alpha 2}$ line, the reflectivity curve of $K_{\alpha 2}$ line is incoherently superposed on the reflectivity curve of $K_{\alpha 1}$ line, with an angular offset of beam incidence and an translational offset of the illuminated area on the surface of the sample. The angular offset between $K_{\alpha 1}$ and $K_{\alpha 2}$, $\Delta\theta$, and the translational offset cross the beam, Δw, are readily given with the geometrical parameters of the set-up as given in Figure 3.4. These offsets and the intensity ratio should be accounted for in fitting the reflectivity curve which contains both of the contributions of $K_{\alpha 1}$ line and $K_{\alpha 2}$ line. The footprint correction factor for $K_{\alpha 2}$ line, P_{f2} has the form

$$P_{f2} = \frac{L_x}{w} sin(\theta - \alpha_{mx} + \Delta\theta), \qquad if \ \ \theta \leq sin^{-1}\frac{w - \Delta w}{L_x} + \alpha_{mx} - \Delta\theta,$$
$$P_{f2} = 1. \qquad otherwise, \tag{3.29}$$

The translational offset along the x-ray beam has a smaller effect and has been ignored in Equation 3.29. The contribution of $K_{\alpha 3}$ line is about 2 orders weaker and has been ignored in the data treatment of reflectivity measurement. The specular reflectivity curves presented in this thesis are usually fit to

$$R(\theta, \lambda_1, \lambda_2) = P_{f1} R(\theta, \lambda_1) + \gamma_2 P_{f2} R(\theta, \lambda_2). \tag{3.30}$$

The value of γ_2 can slightly deviate from 0.5 because the slit may reduce the intensities of $K_{\alpha 1}$ and $K_{\alpha 2}$ lines in an unequal ratio. The variable θ can be easily converted to q_z, through $q_z = \frac{4\pi}{\lambda_1} sin\theta$. The footprint correction should also be made in glancing incidence scattering. But it is not an in-plane correction. The out-of-plane footprint correction for GIXS should be integrated over the out-of-plane beam divergence with Equation 3.29, while the dispersion effect of x-ray source need not to be considered.

In this section, we have only discussed the simplest Bragg peaks which can be fit to a EWGL curve or incoherent summation of several EWGL curves as indicated by Equation 3.25. In many cases, the Bragg peaks can not be fit to EWGL curves because of the effect of microstructure of the epilayers. We may need to develop models of microstructure to study the shape of the scattering patterns. Even though the lineshape of Bragg peaks may be more complicated, the techniques we used to treat the dispersive effect, the slit effect and foot print correction are the same.

Chapter 4

Results and Discussion

4.1 The Samples

The system of heteroepitaxy we have investigated is $Ga_{1-x}In_xAs$ grown on GaAs by MOCVD. The samples were prepared by Prof. Alain Roth of microstructure division, National Research Council of Canada. Our studies have been concentrated on two samples: a 500Å $Ga_{0.81}In_{0.19}As$ epilayer which is referred as the thin sample and a 40000Å $Ga_{0.84}In_{0.16}As$ epilayer which is referred as the thick sample, and both were grown on (001) faces of GaAs crystal substrates. The Indium (In) composition of the thick epilayer might be slightly nonuniform along the direction of growth due to the fluctuation of flow rate. The composition is estimated to be between 16%-15% by the sample producer [127].

Calculating with Eq 2.19, the lattice constant of $Ga_{0.81}In_{0.19}As$ is 5.7303Å and that of $Ga_{0.84}In_{0.16}As$ is 5.7181Å. The lattice mismatchs in these two samples are 1.36% and 1.14% respectively. The slightly non-uniform of In composition in the thick epilayer cause a 0.07% error bars to the value of lattice mismatch. It should be understood that these lattice parameters are simply some preliminary reference numbers to start with, and they may be changed because of our structural measure-

ments. The GaAs substrates in both samples have some miscut at the surfaces with respect to the (001) crystalline planes of GaAs crystals.

The lateral sizes of the thin sample and the thick sample are $4.6 \times 7.7mm$, and $5.0 \times 7.0mm$ respectively. The thicknesses of the GaAs substrates in both samples are $0.2mm$. These samples are as-grown and without further mechanical or chemical treatments. The surfaces of the samples were simply cleaned with acetone before the x-ray structural measurements, which have been performed under normal laboratory environment. The useful parameters and constants of the samples are summarized in the following table for easy reference.

	$t(\AA)$	$a(\AA)$	$\Delta a(\%)$	$L_x(mm)$	$L_y(mm)$
thin-epi	5×10^2	5.7303	~ 0	4.6	7.7
thick-epi	4×10^4	5.7181	~ 0.6	5.0	7.0
substrate	2×10^6	5.6533	~ 0	$\sim$	$\sim$

The subscripts, x and y, denote the two orthogonal in-plane $\langle 110 \rangle$ axes of the GaAs substrates (ref: Section 3.4). The values of Δa are estimated errors of lattice constants due to Indium compositions of epilayers in sample preparation.

4.2 The Data

4.2.1 Out-of-plane Measurements

The out-of-plane data have been measured with normal Bragg scattering, in which the q_z axis of the sample reference frame is principally aligned with the q_l axis of the diffractometer (ref: Section 3.2.2). For our samples, the q_z axis is defined by the $\langle 001 \rangle$ crystalline axis of the GaAs substrate, which will be denoted as q[001] axis in data presentation. The two in-plane axes of the sample reference frame are denoted

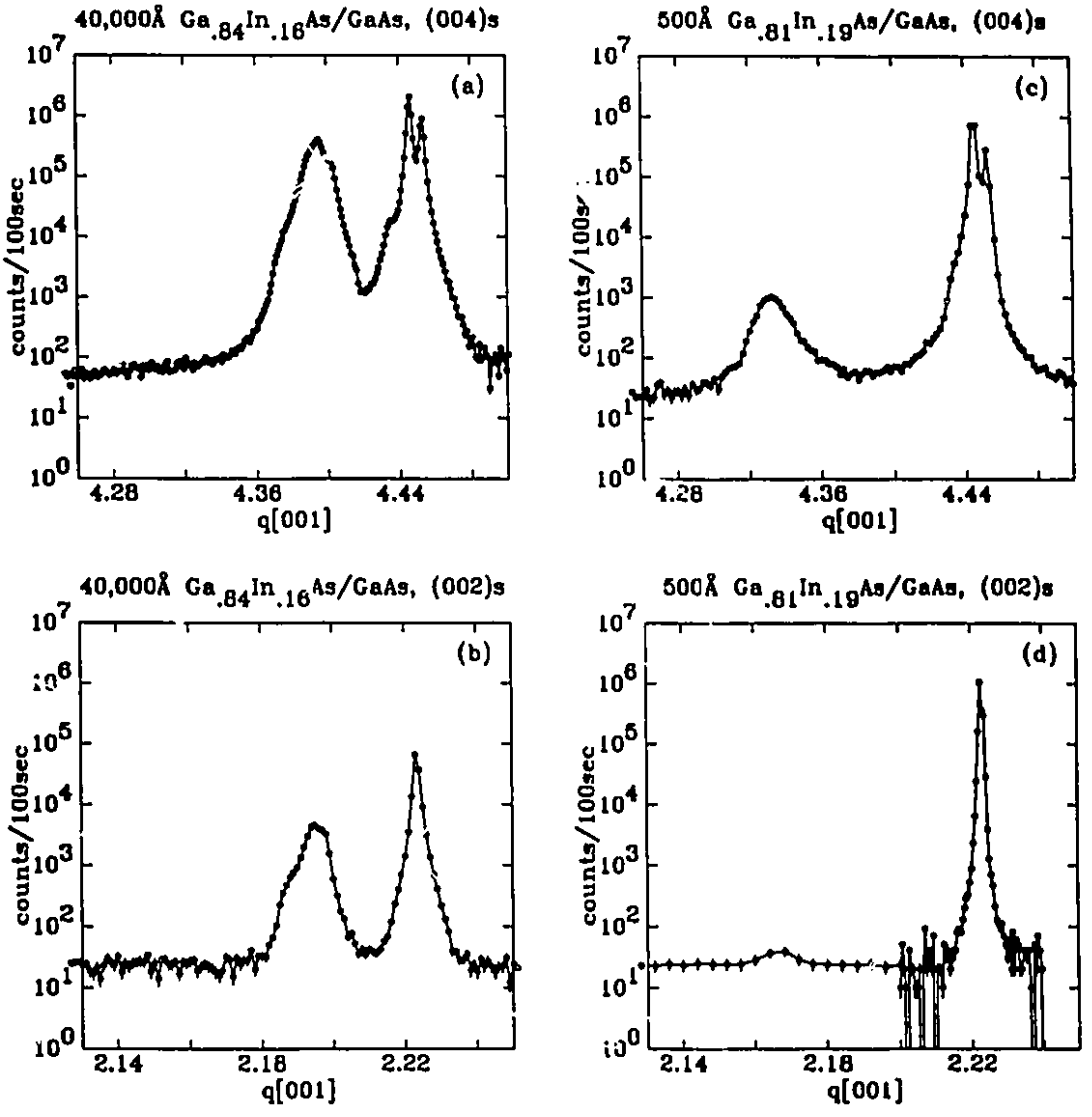

Figure 4.1: The q_l scans along (001) axis of the samples. These are r w data and the solid lines used in figures are guide to the eye. The intensities of scattered x-rays are represented as counts per 100 seconds, which is the regular counting time for epi-peaks. The scattering intensities from the substrate are strong and usually counted in 1 or 10 seconds, and they are scaled to 100 seconds in the figures for comparison. The counting time of (002) peak of 500Å$Ga_{0.81}In_{0.19}As$ shown in (d) is 1000 seconds, while the counting time of the GaAs substrate peak is 1 second. The "dark current" of about 20 counts per 100 seconds presents a nearly uniform background. (a) (004) peaks of the thick sample. (b) (002) peaks of the thick sample. (c) (004) peaks of the thin sample. (d) (002) peaks of the thin sample. The unit of abscissa is [001]$Å^{-1}$, *i.e.*, $Å^{-1}$.

as $q[110]x$ and $q[110]y$ with respect to the preferential quadrant (ref: Section 3.4). In data collection, $q[110]x$ and $q[110]y$ have been nominally taken as $q[110]$ axis and $q[1\bar{1}0]$ axis to meet the vector algebra and define the orientation matrix. By using the zone mode of four-circle goniometry, we collected the data in x-z plane and y-z plane separately.

Figure 4.1 shows the q_l-scans of Bragg peaks along (001) axis of the GaAs substrate. These figures only present the raw data and the solid lines are used to guide the eye. The subfigures (a) and (b) show the (004) and (002) peaks of the thick sample, and the subfigures (c) and (d) show the (004) and (002) peaks of the thin sample. The Bragg peaks of the GaAs substrates are used as references, and their positions agree with the known lattice constants. The difference in shapes of the GaAs (004) and (002) peaks is due to the dispersive effect of the incident x-ray beam. The GaAs (002) peak is close to the non-dispersive condition of our set-up (ref: Section 3.3), and the separation of $K_{\alpha 1}$ and $K_{\alpha 2}$ lines is not resolved. The calculated position of the $Ga_{0.84}In_{0.16}As$ (004) peak is between $4.3953[001]\text{Å}^{-1}$ and $4.3984[001]\text{Å}^{-1}$, and averaged at $4.3968[001]\text{Å}^{-1}$. The measured positions of the (004) and (002) peaks of the thick epilayer agree pretty well with the calculated values from Vegard's law, and indicate that the lattice of the thick epilayer is basically relaxed. The overall profiles of the (004) and (002) peaks of the thick epilayer are essential same and not affected by the wavelength dispersion of the source. This should be attributed to the structural features of the thick epilayer and will be discussed later.

Based on Vegard's law, the calculated position of (004) peak of $Ga_{0.81}In_{0.19}As$ is $4.3859[001]\text{Å}^{-1}$, but the measured position is $4.33[001]\text{Å}^{-1}$. This disagreement indicates a 1.28% out-of-plane lattice spacing expansion of of the thin epilayer. Assuming that the in-plane lattice constant of the thin epilayer is strained to match the lattice of the GaAs substrate, the Poisson's ratio is evaluated to be $\nu = 0.32$

(ref: Equation 2.8), and agrees with the value that previous measured [85]. The HWHM width of the (004) epi-peak of the thin sample is about 0.006[001]$Å^{-1}$, which evaluates the thickness of the thin epilayer to be 500Åand agrees with its nominal thickness. The (002) peak of the thin epilayer is very weak, which has been observed by increasing the counting time to 1000 seconds per data points. Its position in q is half of (004) peak, as expected. A background of 20 counts per 100 seconds appears in all figures is due to the dark current of the detector.

Figure 4.2 shows the out-of-plane meshes of (004) peaks of the epilayers. The two subfigures on the top, (a) and (b), show the (004) epi-peak of the thick sample. The two subfigures at the bottom, (c) and (d) show the (004) epi-peak of the thin sample. The two subfigures on the left, (a) and (c) are meshes in x-z plane, and the two subfigures on the right, (b) and (d), are meshes in y-z plane. The contours are plotted in a logarithmic scale and differ in intensities by factor of two. The maximum intensities of the peaks are labeled as I_m in counts/time in the titles of figures. The four figures are drawn in same scales along axes q[001], q[110]x and q[110]y and to make it easy to compare with each other. In principle, the denser the contour lines are, the sharper the peak is, and the longer the range of atomic ordering in the epilayer. The position and width of the (004) of the thick epilayer as indicated by the contours suggest that its out-of-plane structure is close to that of equilibrium state. Some asymmetric scattering appearing at the lower left corner of the mesh (a) may be due to the microstructure of the epilayer. The intensity of the asymmetric scattering can be estimated by counting the number of contour lines and is about 3 orders weaker than that of the main peak of the thick epilayer. As shown in (b), The (004) epi-peak of the thick sample is misaligned with the (004) peak of the substrate to the negative side of q[110]y axis. The tail of the (004) sub-peak can be seen in both figures (a) and (b). This misalignment of Bragg peaks of the epilayer to the substrate could be possibly induced by the in-plane modulated

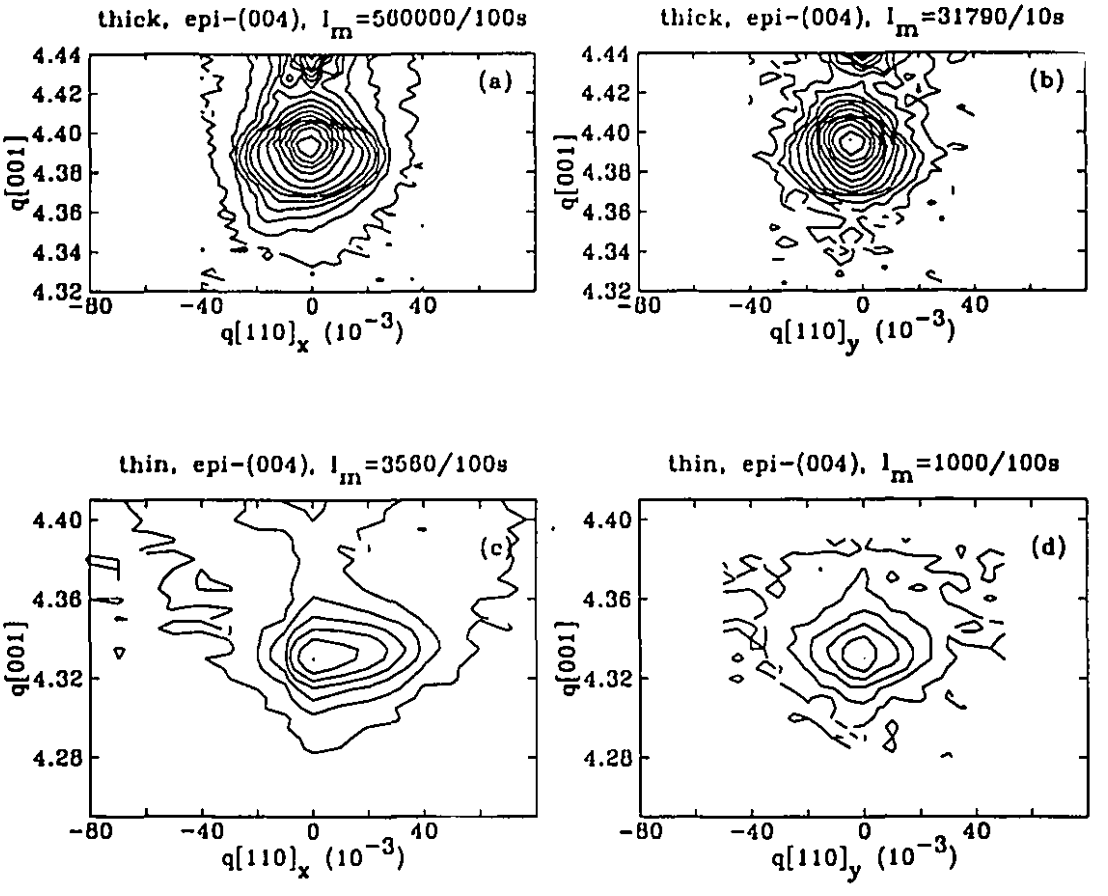

Figure 4.2: The out-of-plane meshes of (004) peaks of epilayers. The maximum counts of the Bragg peaks are labeled as I_m in the titles of figures. The counts of each contour are half of the counts of the contour which is closer to the intensity maximum. The vertical direction is along GaAs (001), and the value of q[001] is referenced to the origin point of reciprocal space with unit [001]Å^{-1}, *i.e.*, Å^{-1}. The horizontal directions are along the in-plane axes x and y, and the value of q[110]x or q[110]y is referenced to the center of the Bragg peak of the GaAs substrate with unit [110]Å^{-1}, *i.e.*, $\sqrt{2}$Å^{-1}. The axes of x and y are defined as previously mentioned in the discussion of the sample. (a) The contours of (004) epi-peak of the thick sample in x-z plane. (b) The contours of (004) epi-peak of the thick sample in y-z plane. (c) The contours of (004) epi-peak of the thin sample in x-z plane. (d) The contours of (004) epi-peak of the thin sample in y-z plane. In (a) and (b) the tail of the center streak of the GaAs substrate (004) peak can be seen.

structure of the epilayer, or the inclination of the whole crystalline (001) planes of the epilayer with respect to that of the substrate. The (004) epi-peak of the thin sample presents a strong asymmetric scattering in the x-z plane towards positive $q[110]x$ direction, as shown in (c). This asymmetric scattering strongly suggests an in-plane microstructure. The scattering of the (004) peak of the thin epilayer in y-z plane is essentially symmetric. The meshes shown on left and right are the same peaks, the different counts of the peak maximums in x-z mesh and y-z mesh is due to the different intensities of the incident beams, which are determined by the slits used in measurements.

The q_l scans of the (004) and (002) peaks of the thick sample are fit to EWGL curves and shown in Figure 4.3. In the subfigure (a), the fit position of GaAs (004) peak for $K_{\alpha 1}$ line is 4.4463[001]Å^{-1}, which agrees with the GaAs lattice constant within the error bar caused by thermal expansion. The HWHM width of the GaAs (004) peak is 0.00123[001]Å^{-1}, which is slightly larger than the resolution limit of q_l scan for GaAs (004) peak because there is a $4\mu m$ $Ga_{0.84}In_{0.16}As$ on top of it. To fit the whole curve, the (004) peak of the GaAs substrate is first fit to EWGL curves with the correction for slit effects, as discussed in Section 3.4. All parameters representing the geometrical and optical features of this setup are then used to fit the (004) peak of the epilayer. The (004) peak of the epilayer is fit with two peaks: one is located at 4.393[001]Å^{-1} with HWHM width 0.0038[001]Å^{-1}, and another one is located at 4.3885[001]Å^{-1} with HWHM width 0.0081[001]Å^{-1}. The ratio of integrated intensities of the first part to the second part is 3.13. Although the uncertainty of the In composition of the thick epilayer is 0.07%, the positions of the first and second peaks of the epilayer are smaller than the averaged theoretical value by 0.087% and 0.19% respectively. This fact suggests that the first peak may be corresponding to the region of the epilayer near the sample surface which is almost completely relaxed and that the second peak may be corresponding to the region of

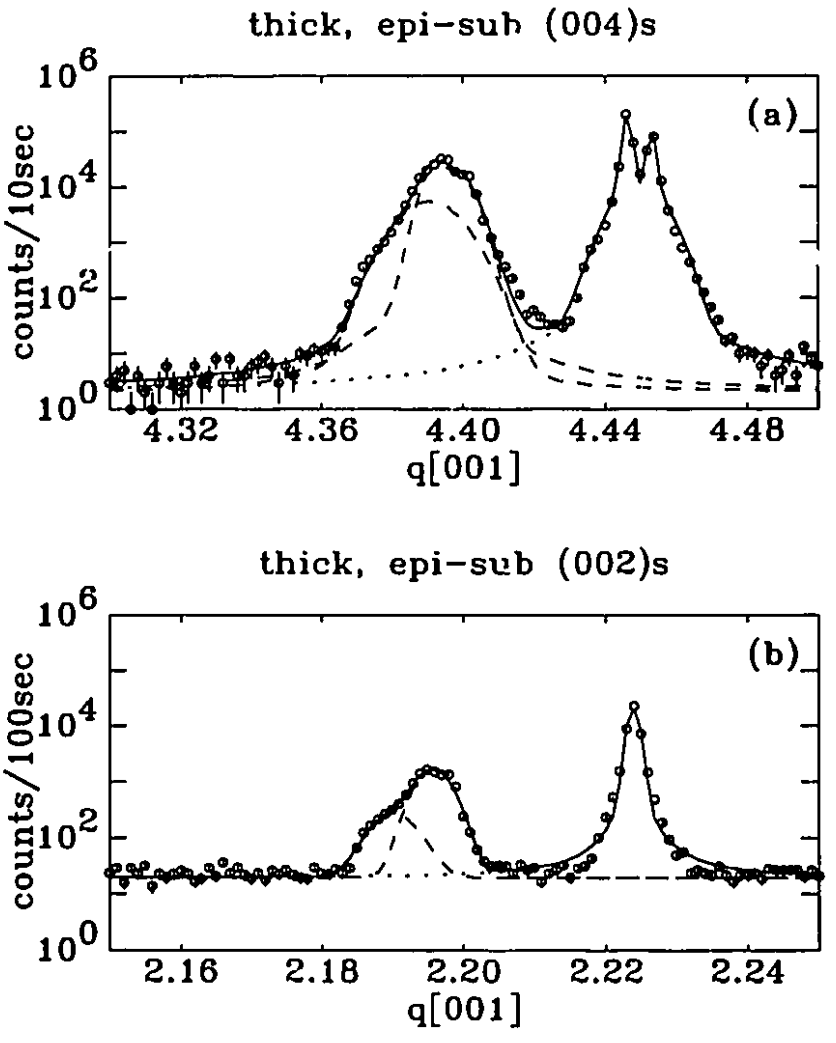

Figure 4.3: Out-of-plane structure of the thick sample determined by $q_l scans$. The intensities of scattered x-rays due to both of the epilayer and the substrate are fit with Lorentzian-Gaussian curves with a constant background of 0.2 counts per second. The solid lines are the fitting curves. The dotted lines are the substrate peaks and the dashed lines are the epilayer peaks. The epilayer peaks resolved as two parts, the nearly fully relaxed epilayer located at higher q[001] with smaller peak width and the strained epilayer located at lower q[001] with bigger peak width. The strained epilayer is closer to the epitaxial interface with out-of-plane strain $\epsilon_z = 0.19\%$ and thickness of about $1.3\mu m$, which is evaluated by the ratio of integrated scattering intensities of the two parts of epilayer. (a) (004) peaks of the thick sample. (b) (002) peaks of the thick sample. The $K_{\alpha 1}$ line and $K_{\alpha 2}$ line are well separated in substrate (004) peak and unresolved in (002) peaks. The dispersion effect of x-ray wavelength indicates the fact that the double-peak shape of the epilayer is due to the microstructure of the epilayer, not the x-ray source.

the epilayer near the epitaxial interface which is still strained. The thicknesses of these two regions can be evaluated by the ratio of integrated intensities, which give a $2.7\mu m$ region near the surface and a $1.3\mu m$ region near the interface. To evaluate the thickness, the absorption should be accounted for because the measured intensity of the scattering from the bottom region must pass the top region. The x-ray absorption length of $Ga_{0.84}In_{0.16}As$ is about $20\mu m$.

These arguments have been confirmed by fitting the (002) peak of the epilayer, which is shown in the subfigure (b). The (002) peak of the substrate is located at $2.2233[001]\text{Å}^{-1}$ with HWHM width $0.00078[001]\text{Å}^{-1}$. The first (002) peak of the epilayer is located at $2.1956[001]\text{Å}^{-1}$ with HWHM width $0.00256[001]\text{Å}^{-1}$, which agrees with the first peak in (004) fitting and supports the argument of nearly full relaxation top layer. The second (002) peak of the epilayer is located at $2.19[001]\text{Å}^{-1}$ with HWHM width $0.0033[001]\text{Å}^{-1}$, which supports the argument of strained bottom layer near the interface. The ratio of integrated intensities of these two parts of the (002) peak is 5.78. This ratio is about twice as big as that measured in the (004) peak because of the x-ray absorption difference at (002) and (004) peaks, and supports the argument of top-bottom regions of the thick sample. The about 0.19% disagreement of the positions of the (002) and (004) peaks of the bottom region may be attributed to the microstructure near the interface.

Fig 4.4 shows the q_t scans of the (004) and (002) peaks of the thick sample. The subfigures of (a) and (b) are the q_t scans along $q[110]x$ direction, and (c) and (d) are the scans along $q[110]y$ direction. The HWHM width of the substrate (004) peak in (a) is $0.00083[110]\text{Å}^{-1}$, which agrees with the resolution of q_t scan for (004) peaks. The HWHM width of the (004) epi-peak of the fully relaxed layer is $0.0048[110]\text{Å}^{-1}$, and that of the strained epilayer is $0.0099[110]\text{Å}^{-1}$. The smaller width of the peak of the top region comparing with that of the bottom region suggests the in-plane structural evolution of the epilayer as its thickness exceeds $1.3\mu m$. The HWHM

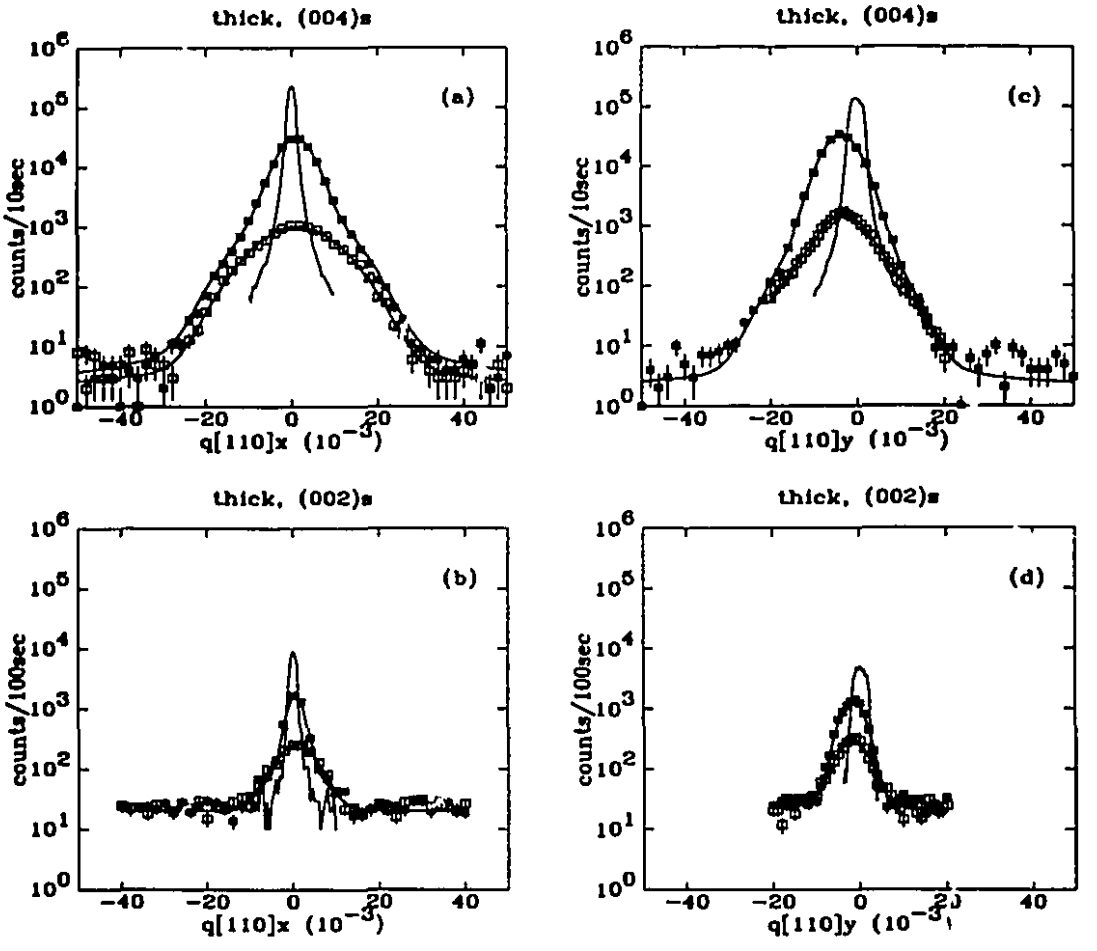

Figure 4.4: Out-of-plane structure of the thick sample determined by q_t scans. The solid curves without pts are the q_t scans of substrate peaks (raw data). The solid lines with data points are fitting curves of the epilayer peaks. The q_t scans of the epi-peaks are taken at the two peak maximums which are indicated by the q_l scans as shown in Figure 4.3. Each epi-peak is fit with two parts, and their ratio of maximum intensities is determined by the fitting of q_l scan. The q_t scans and q_l scans are fit alternatively a few times to get the physical parameters with improved accuracy. (a) (004) peaks along x axis. (b) (002) peaks along x axis. (c) (004) peaks along y axis. (d) (002) peaks along y axis. The width of the peaks due to the strained part is about twice of that due to the relaxed part. In the x direction the epi-peaks are well aligned with the sub-peaks, but in the y direction the epi-peaks are about 0.07° misaligned to those of the sub-peaks. The background of 0.2 counts per second is accounted for in all data fittings.

width of the substrate (002) peak in (b) is 0.00077[110]Å^{-1}, and those of the top and bottom layers are 0.0018[110]Å^{-1} and 0.005[110]Å^{-1} respectively. The two subfigures on the right, (c) and (d), are the similar scans but along q[001]y direction. The HWHM width of the (004) sub-peak in (c) is 0.0014[110]Å^{-1}, and those of (004) epi-peaks are 0.0045[110]Å^{-1} and 0.0058[110]Å^{-1} respectively. The (004) peak of the epilayer is 0.07° misaligned with the substrate (004) peak, and the (002) peaks show the same feature. This misalignment had been previously explained as tilting of the crystal planes of the epilayer with respect to that of the substrate [85], but can also be interpreted as the effect of microstructure in the strained epilayer. The HWHM width of (002) peak of the substrate is 0.0013[110]Å^{-1}, and those of the epilayer are 0.0029[110]Å^{-1} and 0.0035[110]Å^{-1} respectively. The ratio of integrated intensities of Bragg peaks of the epilayer to that of the substrate agrees with the thickness of the epilayer. The unit of integrated intensity of a Bragg peak is counts·Å^{-2}.

With the same method, the q_t scans of the (004) epi-peak of the thin sample are fit, and shown in Fig 4.5. The HWHM width of the (004) sub-peak along q[110]x is 0.00021[110]Å^{-1}. The (004) peak of the thin epilayer along q[110]x is fit by two peaks. The HWHM width of the peak well aligned with the substrate is 0.0024[110]Å^{-1}, while that of peak which is misaligned to the substrate 0.16° is 0.013[110]Å^{-1}. These peaks are all well aligned to the substrate along q[110]y direction, and their widths are 0.0024[110]Å^{-1} and 0.0128[110]Å^{-1} respectively. The width of the substrate along this direction is 0.00023[110]Å^{-1}.

The q_t scan of the thin (004) peak is also fit, and shown in Figure 4.6. The sharp peak is located at 4.3305[001]Å^{-1} with HWHM width of 0.0061[001]Å^{-1}, and the broad peak is located at 4.3352[001]Å^{-1} with HWHM width of 0.0128[001]Å^{-1}. The substrate (004) peak of the thin sample is located at 4.4462[001]Å^{-1} with HWHM width 0.00072[001]Å^{-1}. The ratio of integrated intensities of the epilayer to the substrate is 0.029, and agrees with the scattering of an epilayer of 500Åthick. The

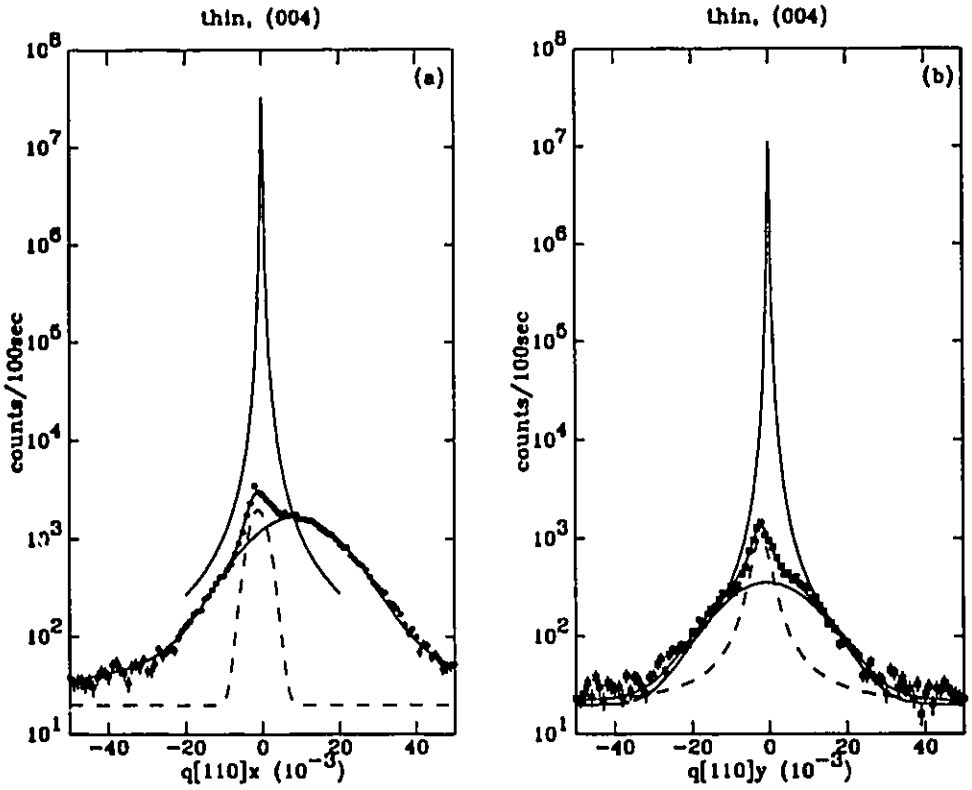

Figure 4.5: Out-of-plane structure of the thin sample suggested by q_t scans. The solid lines without pts are fitting curves of q_t scans of the substrate (004) peaks, used for indicating the transverse resolution of the diffractometer near GaAs (004). The shape of (004) peak of the epilayer suggested in-plane microstructure. With the same method as used in fitting q_t scans of the thick sample, the (004) peak of the epilayer is fit as two parts, one is broader and another is sharper but still quite bigger than the instrumental resolution. (a) (004) peaks along x axis. (b) (004) peaks along y axis. The broad part of the epi-peak along x axis is misaligned to that of the substrate, while it is quite well aligned along y axis. The sharp part in both x and y directions are well aligned with the substrate.

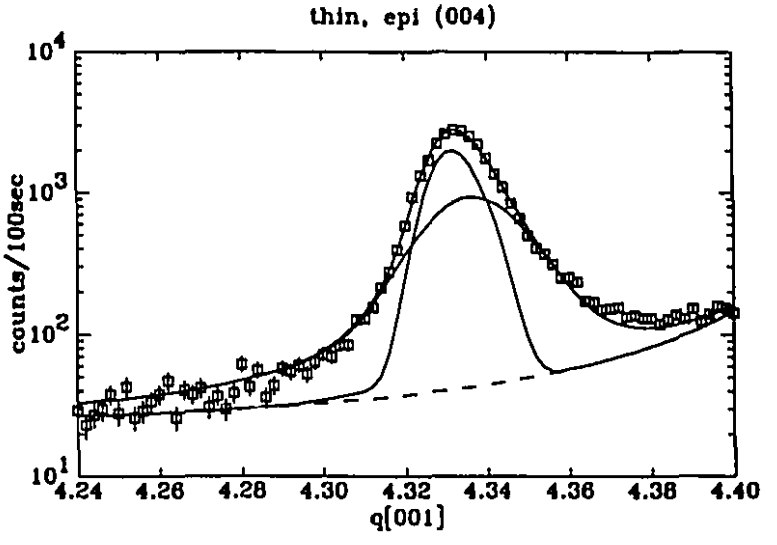

Figure 4.6: Out-of-plane structure of the thin sample suggested by q_t scans. The (004) peak of the thin epilayer is fit as two parts, and the ratio of maximum intensities of the two parts is determined by data fitting of q_t scans, as shown in Figure 4.5. The dashed line is the tail of the streak of the substrate (004) peak. The width of the sharper part of the epi-peak agrees with the thickness of the epilayer, *i.e.*, 500Å. Combining with the data fitting of q_t scan of this peak, the total integrated intensity is determined, which also evaluates the thickness of the epilayer to be 500Å.

width of the sharp part of the epi-peak along q[001] direction also gives the same evaluation of the thickness of the epilayer. The (002) peak of the thin epilayer is weak and not fit.

The fitting of the (004) peak of the thin epilayer shown above is only a preliminary examination of the scattering of the thin epilayer. The incoherent summation of scattering may not be adequate for an epilayer of 500Åthick, which is smaller than the coherence length of the incident x-rays. The scattering of the thin epilayer as measured should be considered as a single peak with a shape which is due to microstructure and will be discussed later.

4.2.2 Reflectivity Measurements

Figure 4.7 shows the reflectivity measurement of the thin sample in x-y plane. The mesh is performed with a series of ω-scans along q_x, in which the incident and exit angles of x-rays are equal with respect to the sample surface and summed up to 2θ. The angle ω has been reset as zero with respect to the crystalline plane of the substrate (ref: Section 4.1.1). The specular reflection of the thin sample occurs at $\omega = 1.4025°$. The cross-section of the incident beam is determined by Slit 3 (ref: Figure 3.3), which has been set to be $0.1 \times 4.0mm$ in this measurement. The length of the sample along x axis is $4.6mm$. The two "wing"s starting at $q_x = 0.53Å^{-1}$ are called "Yoneda wings", which appear when either the incident or the exit angle of the x-ray beam equals the critical angle of the sample. The diffuse scattering of this sample is asymmetric towards the lower ω side. The subfigure at the bottom of Figure 4.7 shows three longitudinal scans, *i.e.*, q_l scans, along the surface normal, at $\omega = 1.35°$ (solid line), $1.4025°$ (pts) and $1.45°$ respectively. The q_l scan at $\omega = 1.4025°$ is on the ridge of the specular scattering, and the wiggles is due to the interference of the x-rays reflected from the surface and interface of the thin epilayer. The asymmetry of the non-specular scattering is shown by the intensity difference

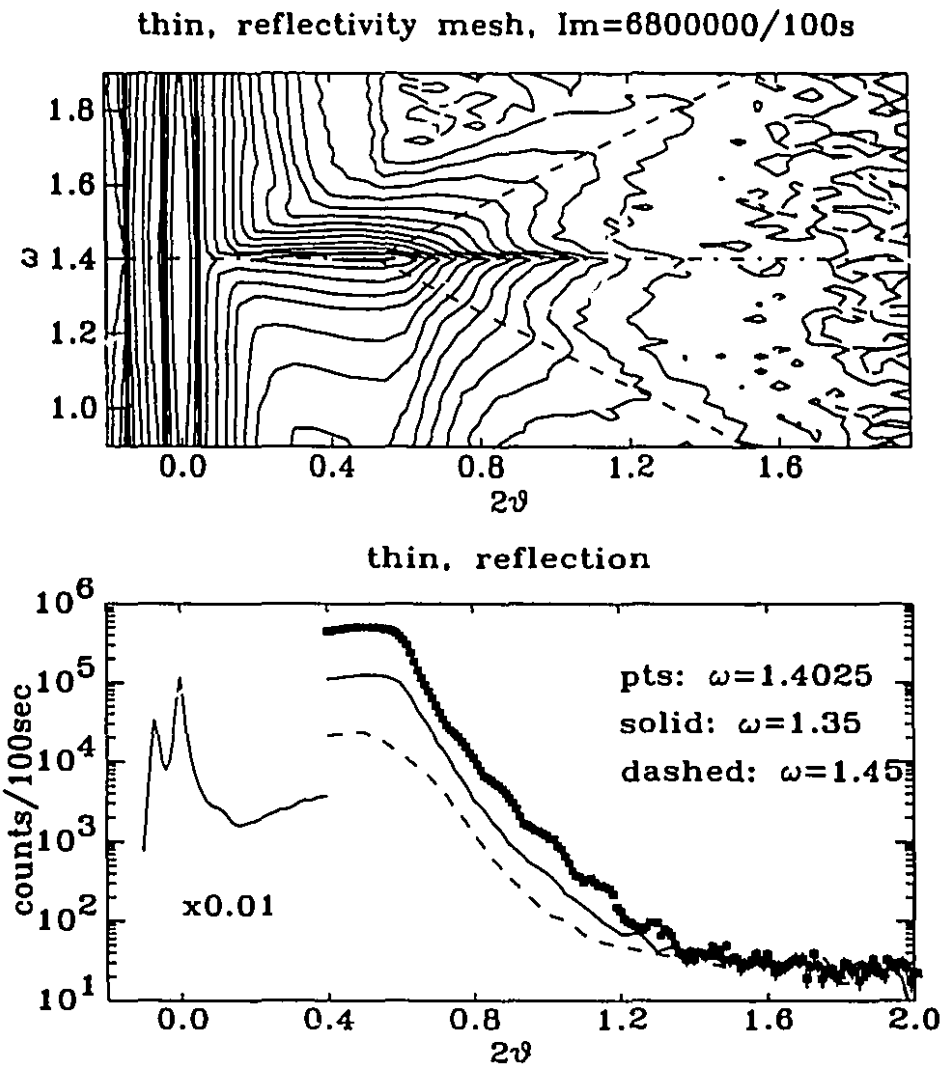

Figure 4.7: Reflectivity measurement of the thin sample. The cross-section of the incident x-ray beam is $0.1 \times 4.0mm$. The counts around $2\vartheta = 0$ is half of the incident beam directly accepted by the counter. The specular reflection occurs at $\omega = 1.4025°$, which is the projection of the miscut in x-z plane. The non-specular scattering is asymmetric towards the lower ω side. The maximum counts which appears at $2\theta = 0$ on the top figure is 6800000/100sec. The two wings around the specular reflection and start at the critical angle are the so-called "Yoneda" wings. The bottom figure shows three longitudinal scans (2θ-θ scan) at ω equals 1.4025° (pts line), 1.35° (solid line) and 1.45° (dashed line) respectively. The wiggles appear in the specular curve is due to the interference of reflected x-rays from the surface and interface. The counting time for the x-ray beam at 2θ around zero is 1 second.

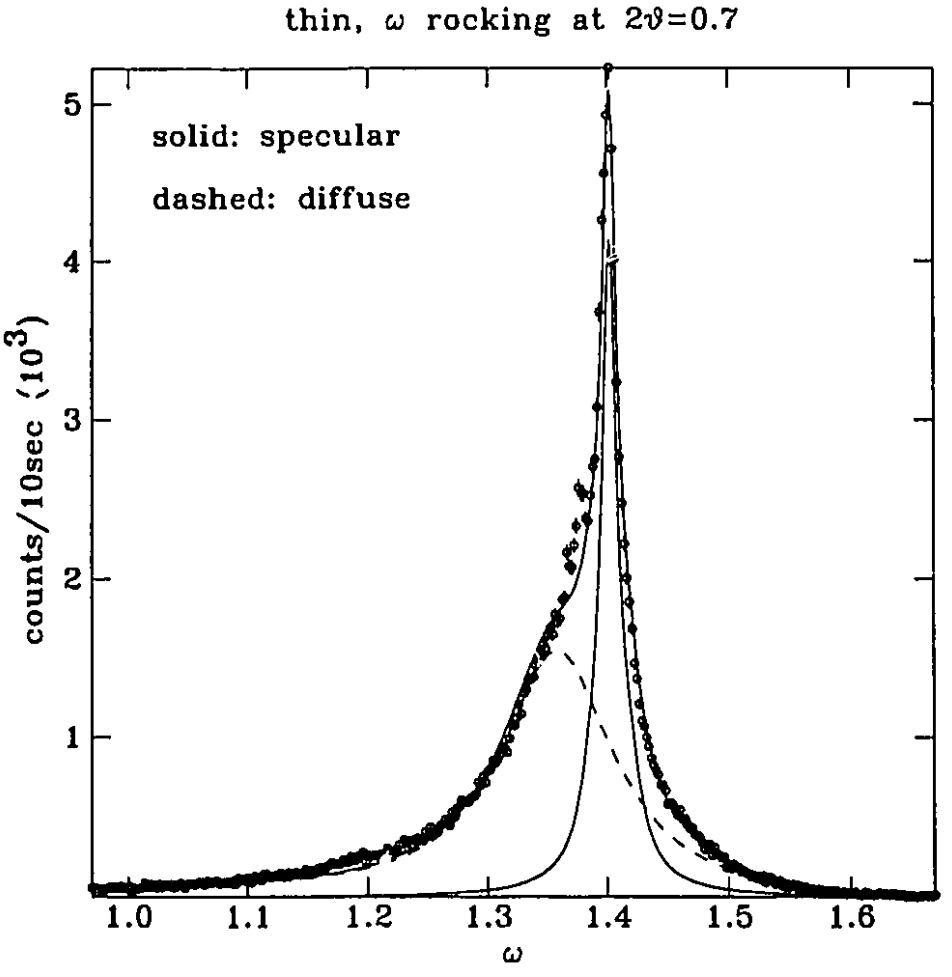

Figure 4.8: The ω scan of thin sample reflection at $2\theta = 0.7°$. The reflection is fitted as two parts: a) the specular reflection located at $\omega = 1.402°$ with HWHM width 0.0087°; and b) the non-specular scattering centered at $\omega = 1.358°$ with HWHM width 0.057° . The ratio of integrated intensities of the specular part to the non-specular part is 0.4. The intensity of diffuse scattering at the specular ridge ($\omega = 1.402°$) is 1.0/7.5 of the intensity of the specular scattering, which is about the average intensity of the scattering taken at ω equals 1.35° and 1.45°.

of q_l scans taken at $\omega = 1.35°$ and $\omega = 1.45°$. The primary incident beam at arm zero with the sample aligned has been presented as a reference. The counting time for a single data point is 1 second.

To extract information from the specular reflection, the diffuse scattering should be subtracted. Figure 4.8 shows the ω scan cross the specular ridge at $2\theta = 0.7°$. This profile can be fit to two Gaussian peaks: a) the specular scattering peaked at $\omega = 1.4025°$ and the diffuse scattering peaked at $\omega = 1.358°$. The width of the specular scattering is resolution limited ($\Delta\omega = 0.01°$), and the width of the diffuse scattering is five times broader. As shown in the figure, the intensity of the diffuse scattering at the specular ridge is about 1.0/7.5 of the maximum of the specular scattering, which can be considered as an average of the intensities taken at $\omega = 1.35°$ and $\omega = 1.45°$. By subtracting the average intensity of the two off-specular q_l scans and normalizing by the primary incident beam, the true specular reflectivity of the sample is obtained.

Figure 4.9 shows the fitting of the specular reflectivity along q_z. The thickness of the epilayer is measured to be 492Å. The *rms* values of the surface and interface roughnesses are measured to be 25.3Å and 15Å respectively. The reflectivity curve is fit by accounting for the footprint correction in theoretical calculations because it is different for $K_{\alpha 1}$ and $K_{\alpha 2}$ lines (ref: Section 3.4). The solid curve in the figure shows the reflectivity of only $K_{\alpha 1}$ line with footprint correction suppressed. The specular reflectivity below the critical angle is evaluated to be 0.6 because of the intensity lost to the diffuse scattering. The electron density of the epilayer evaluated by the value of critical angle is about 1.1% larger than that of $Ga_{0.81}In_{0.19}As$ in the equilibrium state, and suggests strong in-plane strain. For comparison, the dashed line shows the calculation with equal roughness at the surface and the interface, in which the amplitude of intensity oscillation along q_l equals constant. The dotted line shows the calculation with a smooth interface, in which the amplitude of intensity

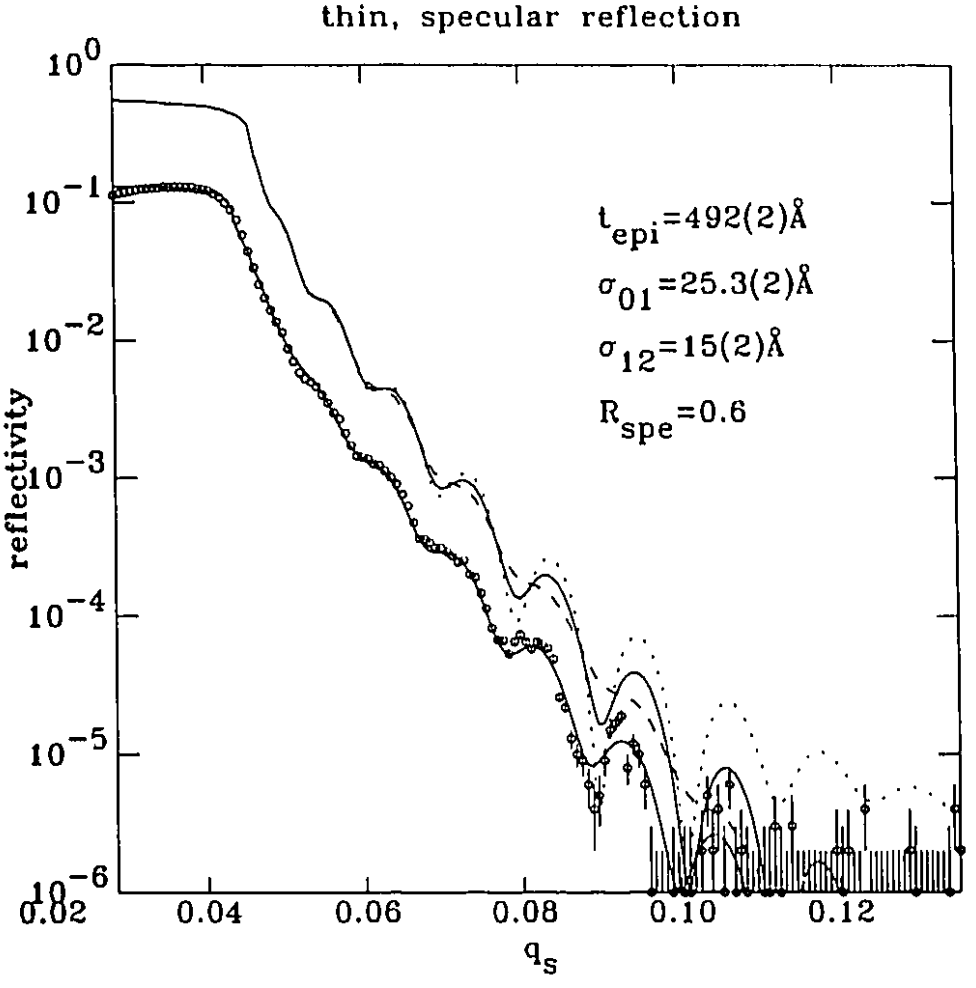

Figure 4.9: Specular reflectivity of the thin sample. The average thickness of the epilayer is accurately determined to be 492(2)Å. The electron density of the epilayer is 1.1% higher than that of calculated value, which can be attributed to the in-plane lattice contraction. The *rms* value of surface roughness is 25.3(2)Å and that of interface roughness is 15(2)Å. The roughness we measured is actually a "local" roughness (within the coherence length of the x-ray source), and can be quite different from the "global" roughness observed by TEM [49]. The solid curve without points is the reflectivity curve of $K_{\alpha 1}$ line without any footprint correction. The specular reflectivity below the critical angle is about 0.6. The dashed line and the dotted line show the effect of alternately setting the interface roughness equals the surface roughness and zero, none of which describes the data.

oscillation is modulated.

The diffuse scattering can be studied separately by ignoring the specular scattering. Figure 4.10 shows the diffuse scattering at $2\theta = 0.7°$, or at $q_z = 0.0498\text{Å}^{-1}$. The asymmetric geometric factor presented by the transverse scans has been corrected for. The angular offset of ω is reset and the origins of q_x and q_y are defined at the specular ridge. The relation between ω and q_x or q_y is given by [37]

$$q_x = q_z tan(\omega - \omega_0), \tag{4.1}$$

where ω_0 is the angular position of specular reflection. The rough surface of as-grown epilayer can be approximated as self-affine and the height-height correlation function can be written as

$$g(r) = Ar^{2h}, \tag{4.2}$$

where r is in-plane correlation distance, h is the index of fractal dimension and A is coefficient to present the correlated length scale. The value of h determines how smooth or jagged (subjectively speaking) such a surface is. Thus, small values of h produce extremely jagged surfaces, while values of h approaching 1 appear to have "smooth" hills and valleys. By approximating h equals to one (for simplicity), the diffuse scattering can be calculated with the formula

$$\left.\frac{d\sigma}{d\Omega}\right|_{dif} = \frac{2\pi C}{A{q_z}^4} e^{-({q_x}^2+{q_y}^2)/2A{q_z}^2}, \tag{4.3}$$

where C is a proportionality constant. By fitting the diffuse scattering, we obtain the values of A to be 0.056 along q_x and 0.062 along q_y.

The reflectivity measurement of the thick sample is presented in Figure 4.11, the effect of the substrate can not be seen. It seems that there is no specular scattering on the surface of the thick sample. The diffuse scattering is maximized at $\omega = 0.15°$ along x axis and $\omega = 0.14°$ along y axis. The surface roughness is asymmetric, which has rms values of 27Å along x and 18Å along y. The A coefficient

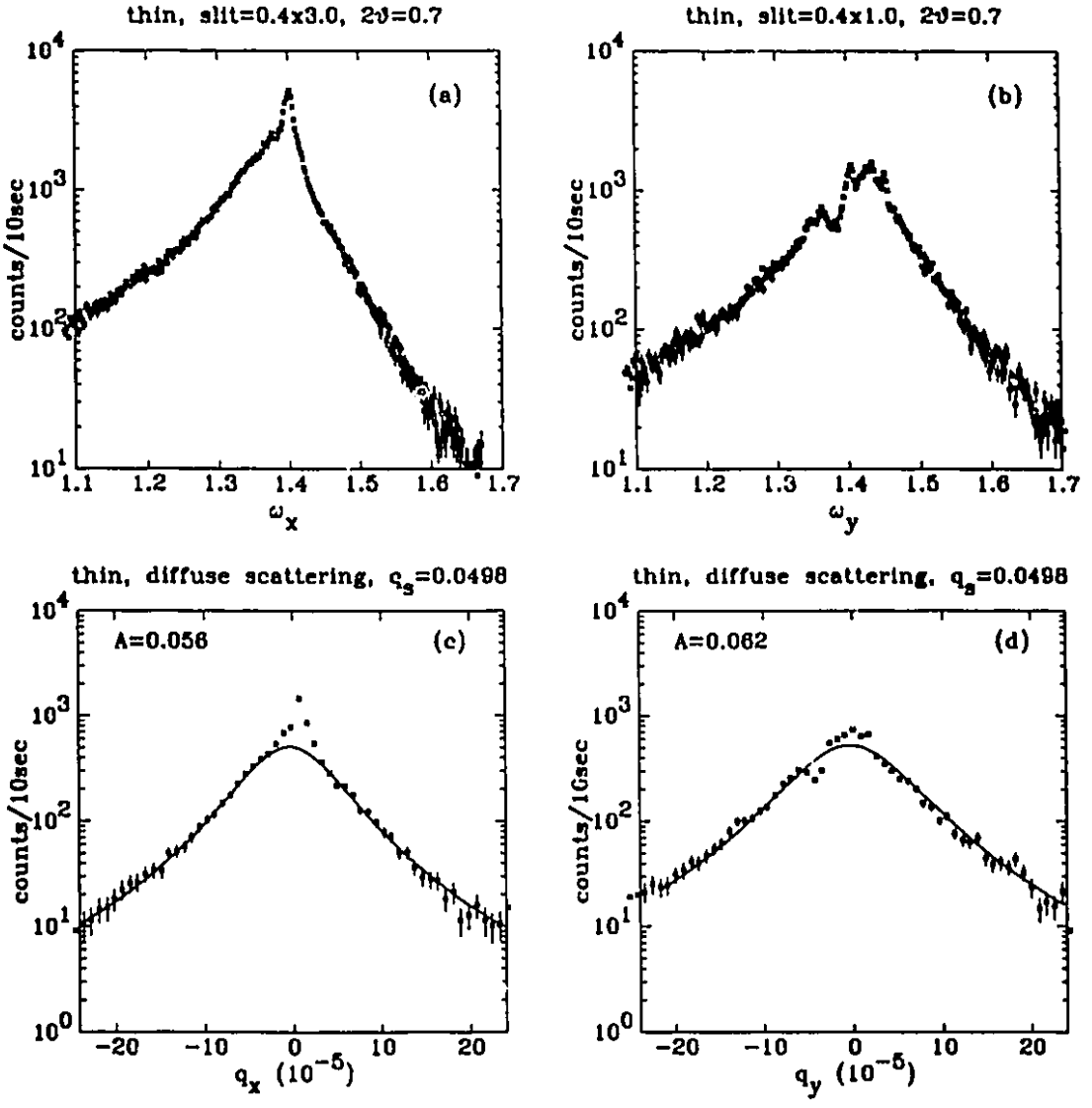

Figure 4.10: Rocking curves crossing the reflection ridge and diffuse scattering of the thin sample. (a) ω_x scan at $2\theta = 0.7$. The same data is shown in Figure 4.8, but here the counts are plotted in logarithmic scale. (b) ω_y scan at $2\theta = 0.7$. It shows more than one specular maximum. The projection of miscut in y-z plane is about 1.45°. (c) and (d) show the same data as shown in (a) in (b) respectively. The asymmetric factor mainly due to the miscut is corrected and the number of data points are reduced by taking one out of five. The coefficient of height-height correlation function is 0.056 along q_x and 0.062 along q_y.

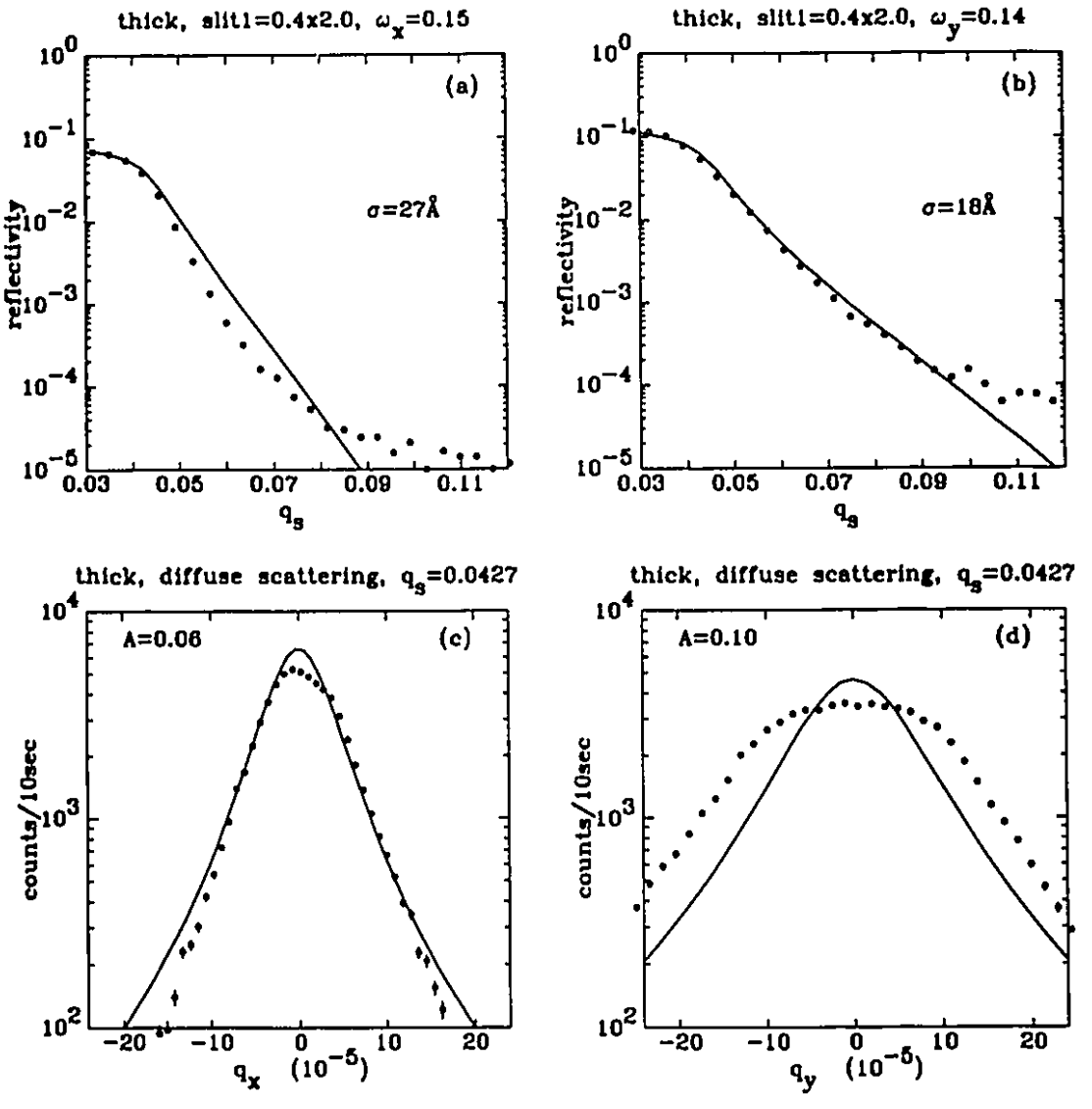

Figure 4.11: Reflection of the thick sample. (a) q_l scan along the surface normal at $\omega_x = 0.15$. (b) q_l scan along the surface normal at $\omega_y = 0.14$. (c) The transverse scan cross the ridge of reflection along q_x. (d) The transverse scan cross the ridge of reflection along q_y. As indicated by (c) and (d), no true specular reflection can be identified along both axes, and all of the counts are treated as diffuse scattering. The total reflection below the critical q_s is scaled to unity and the reflection curves show in (a) and (b) include the footprint effect. The *rms* values of the surface roughness are 27Å and 18Å respectively. The coefficient A equal 0.06 along q_x and 0.10 along q_y.

of the height-height correlation function is also different along the two orthogonal axes, one is 0.06 and another one is 0.10. These parameters are extracted simply by comparison, not by fitting the data.

As a summary to this subsection, we have learned: the thickness of the thin epilayer is 492Åand its surface and interface roughnesses are 25.3Å and 15Å respectively. The specular reflectivity below the critical angle is 0.6. There is no true specular reflection of the thick sample, which has asymmetric roughnesses of 27Å along x axis and 18Å along y axis. The miscuts on the surface of both samples are measured, which are about 2° for the thin sample and 0.2° for the thick sample.

4.2.3 In-plane Measurements

The in-plane structures of the epilayers have been measured with glancing incidence scattering, and the data have been collected with azimuth mode of the four-circle goniometer (ref: Section 3.2.3). With glancing incidence scattering, the momentum transfer of the incident x-rays, q, has been principally aligned in the x-y plane of the sample with only a small out-of-plane component to assure the positive incident and exit angles between the x-rays and the surface of the sample. By means of azimuth mode, the data can be directly collected in the reciprocal space under the constraint of specular x-ray reflection with respect to the sample surface, *i.e.*, $\alpha_h = \alpha_i$, as shown in Figure 3.8. Because the in-plane data are related to the out-of-plane alignment of the x-ray momentum transfer in glancing incidence scattering, the lattice truncation rods of the substrate crystal should be first studied.

Figure 4.12 shows the $(220)_x$ scattering rod of the substrate of the thin sample. The subfigures (a) and (b) present the same scattering rod with q_t-q_v meshs, but the data have been collected in different reference coordinate frames. Figure 4.12 (a) shows the scattering rod with respect to the surface normal and cleavage edge of the substrate crystal, while Figure 4.12 (b) shows the rod with respect to the crystallo-

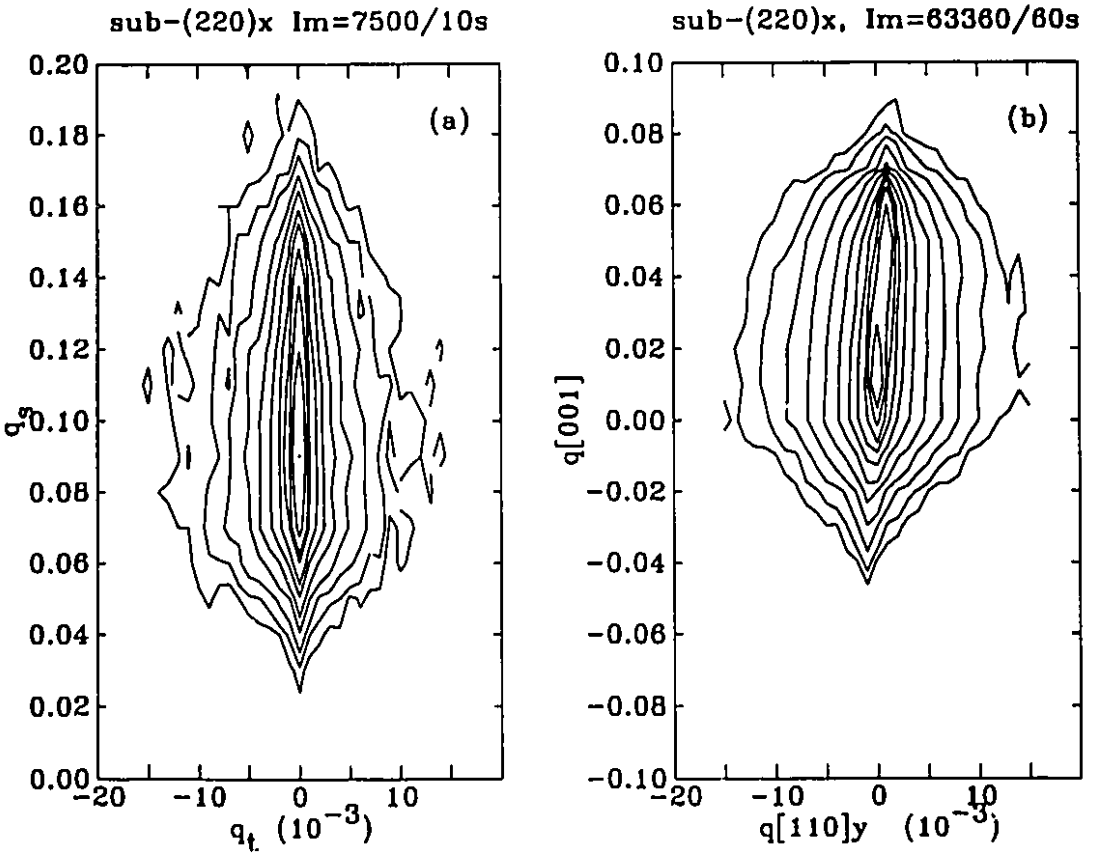

Figure 4.12: The $(220)_x$ lattice truncation rod of the substrate of the thin sample. (a) The q_t-q_v mesh of the rod at $q_x = 2.2222[110]x$ with q_v along the surface normal. (b) The q_t-q_v mesh of the rod at $q_t = 2.223[110]x$ with q_v along (001) axis of the substrate. The axis q_t in figure (a) has the same unit as the axis $q[110]y$ in figure (b), *i.e.*, $\sqrt{2}\text{Å}^{-1}$. Both of them have been enlarged by a factor of 2 in the figures for clarity. The lattice truncation rod is perpendicular to the surface of the sample. The vertical axes q_v and $q[001]$ have the same unit, *i.e.*, Å^{-1}. The offset of the scattering maximum of the rod along the vertical axes is caused by the projection of the surface miscut angle in x-z plane, *i.e.* α_{mx}. The inclining angle of the scattering rod towards positive q[110]y in figure (b) is the projection of the surface miscut angle in y-z plane, *i.e.*, α_{my}. The scattering rod shown in (b) has been cut in higher $q[001]$ side by the vertical window of Slit 3.

graphic axes of the substrate crystal. As mentioned earlier, the cleavage edge of the sample agrees with one of the in-plane (110) axes. The unit of horizontal axis used for q_t in (a) and that used for $q[110]y$ in (b) are both equal to $\sqrt{2}$Å^{-1}, and enlarged by factors of 2 in the figures for clarity. The units of vertical axes in both (a) and (b) are equal to Å^{-1}.

The in-plane component of the x-ray momentum transfer, q_x, shown in Figure 4.12 (a), is set at 2.2222[110]Å^{-1}, which has been optimized by a q_t scan. The intensity maximum of the scattering rod out-of-plane appears at $q_z = 0.08$Å^{-1}. The value of the x-ray momentum transfer is given by the vector summation of the in-plane and out-of-plane components and calculated to be 2.2229[110]Å^{-1}. The angular position of the intensity maximum of the scattering rod on χ-circle, *i.e.*, the angle between the x-ray momentum transfer and the surface of the sample, is 1.46°. This angle is slightly bigger than α_{mx}, the x-z component of the surface miscut angle, which equals 1.4025° (ref: Section 4.2.3). The position of intensity maximum of the scattering rod is determined not only by the in-plane lattice spacing of the sample, but also the x-ray reflection and footprint correction on the sample surface. The crystal plane and surface of the sample are related by the miscut angle, which play an important role in in-plane data measurement.

The in-plane component of the x-ray momentum transfer, q_x, shown in Figure 4.12 (b), is optimized at 2.223[110]Å^{-1}, at which the mesh in y-z plane of the sample has been carried out. The intensity maximum of the scattering rod appears at $q_z = 0.05$[001], indicating the geometrical and optical effects of glancing incident scattering. As expected, the scattering rod inclines towards q[110]y direction by 1.45°, which agrees with α_{my}, the y-z component of the surface miscut angle. The rapid decreased intensity at high q[001] side of the scattering rod is due to Slit 3, (ref: Section 3.4).

In principle, the in-plane data can be collected by taking either q[001] or q_z

of the sample as the azimuth reference vector. In both cases, corrections to the intensities or to the positions of the peaks are required as fitting the in-plane data to EWGL curves. Because the resolution along q_v is relatively low, 0.022Å^{-1}, the out-of-plane component of the x-ray momentum transfer can be easily optimized. All the scattering rods of the in-plane peaks of the substrate crystal have the same features, *i.e.*, along the surface normal, but their intensities depend on their orientations because of the surface miscut. Comparing with that of the substrate, the scattering rods of the epilayer are longer and weaker due to its smaller thickness.

Figure 4.13 shows the contours of four in-plane peaks of the thin sample: $(220)_x$ peaks in (a); $(220)_y$ peaks in (b); $(440)_x$ peaks in (c) and $(440)_y$ peaks in (d). They are q_l-q_t meshs in the x-y plane of the sample reference frame and taken at $q_z = 0.0[001]\text{Å}^{-1}$, where the intensity of scattering is optimized out-of-plane (ref: Figure 4.12 (b)). The four substrate peaks of GaAs crystals are located at the positions as expected: the (220) peaks at $2.223[110]\text{Å}^{-1}$ and the (440) peaks at $4.446[110]\text{Å}^{-1}$. The dispersion of $K_{\alpha 1}$ and $K_{\alpha 2}$ emission lines of the x-ray source are clearly shown in the higher order peaks. The substrate peaks are sharp with high intensity. The broader parts of scattering in these figures are due to the $Ga_{0.81}In_{0.19}As$ epilayer. As the contours show, the in-plane atomic ordering of the epilayer is not as good as that of the substrate. The dispersive effect of the $K_{\alpha 1}$ and $K_{\alpha 2}$ lines of the source helps us to identify the scattering of the epilayer because it is different for (004) and (002) peaks (ref: Section 3.3). The in-plane peaks of the epilayer do not match the in-plane peaks of the substrate, which reveals a residue incommensurability between the epilayer and the substrate. The broadening of the high order peaks, of the epilayer, as indicated by the density of the contour lines, demonstrates the strong non-uniform microstrain of the epilayer with respect to the epitaxial interface. The misalignment of the center of the epilayer peak and the substrate peak along $q[110]_y$ axis is observed.

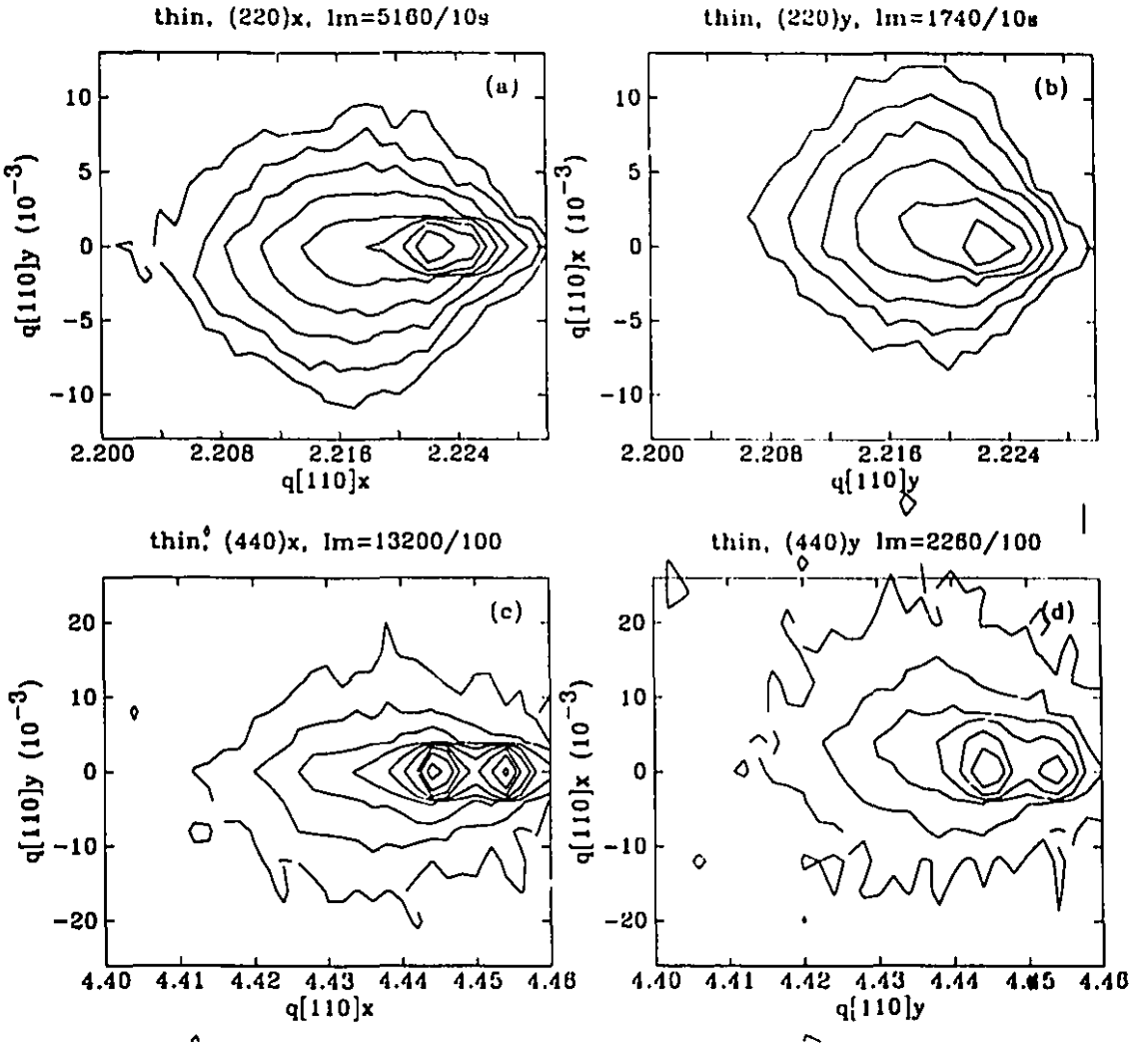

Figure 4.13: Contours of in-plane Bragg peaks of the thin sample. (a) The $(220)_x$ peaks. (b) The $(220)_y$ peaks. (c) The $(440)_x$ peaks. (d) The $(440)_y$ peaks. The meshs are taken at $q_v = 0.0[001]$. The peaks of the GaAs substrate are sharper and those of the epilayer are broader. Comparing $(220)_x$ peak with $(440)_x$ peak, or comparing $(220)_y$ peak with $(440)_y$ peak, the wavelength dispersion of x-ray source and the scattering of the epilayer can be easily identified. The widths of epi-peaks are more than twice as broad in the $(440)_x$ and $(440)_y$ peaks than those in the $(220)_x$ and $(220)_y$ peaks, as shown by the density of contour lines. The centers of the epilayer peaks are 0.18% mismatched that of the substrate. A 0.03° misalignment of the epilayer peaks to that of the substrate along the $q[110]y$ axis has been shown in both (b) and (d).

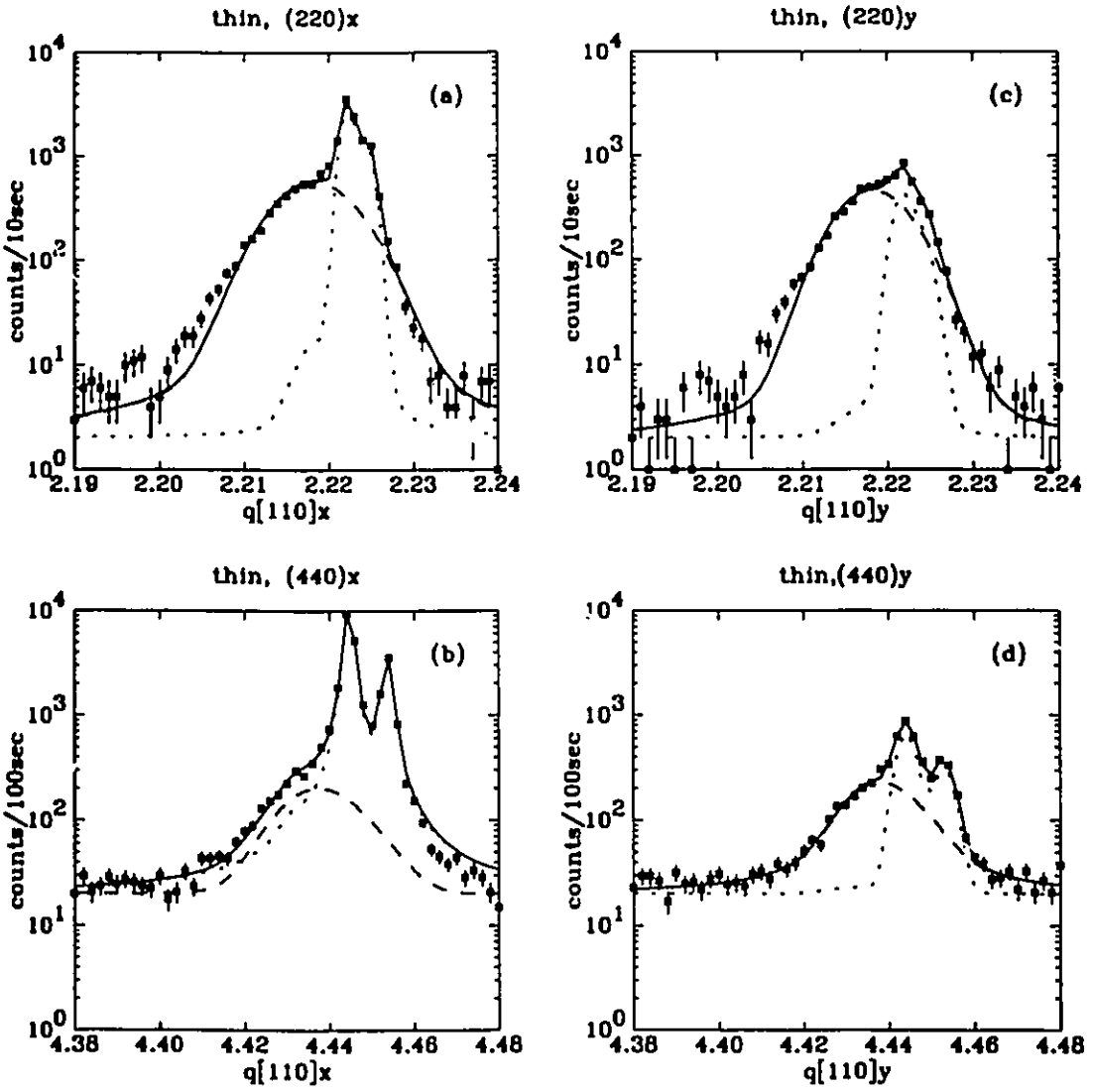

Figure 4.14: In-plane structure of the thin sample with q_l scans. (a) The fitting of the $(220)_x$ peaks. (b) The fitting of the $(440)_x$ peaks. (c) The fitting of the $(220)_y$ peaks. (d) The fitting of the $(440)_y$ peaks. The widths of the substrate peaks are broader than the resolution because of the epilayer. The wavelength dispersion is resolved at higher q_l scans, as shown in (b) and (d). The maximum intensities of the substrate peaks in (c) and (d) are not presented because q_l has been optimized at the epi-peaks. There are some extra scatterings at lower q_l side in figures (a) and (c), which are not exactly fit to single EWGL curves for the peaks of epilayer. The solid lines are the fitting curves, the dashed lines are the epi-peaks and the dotted lines are the substrate peaks.

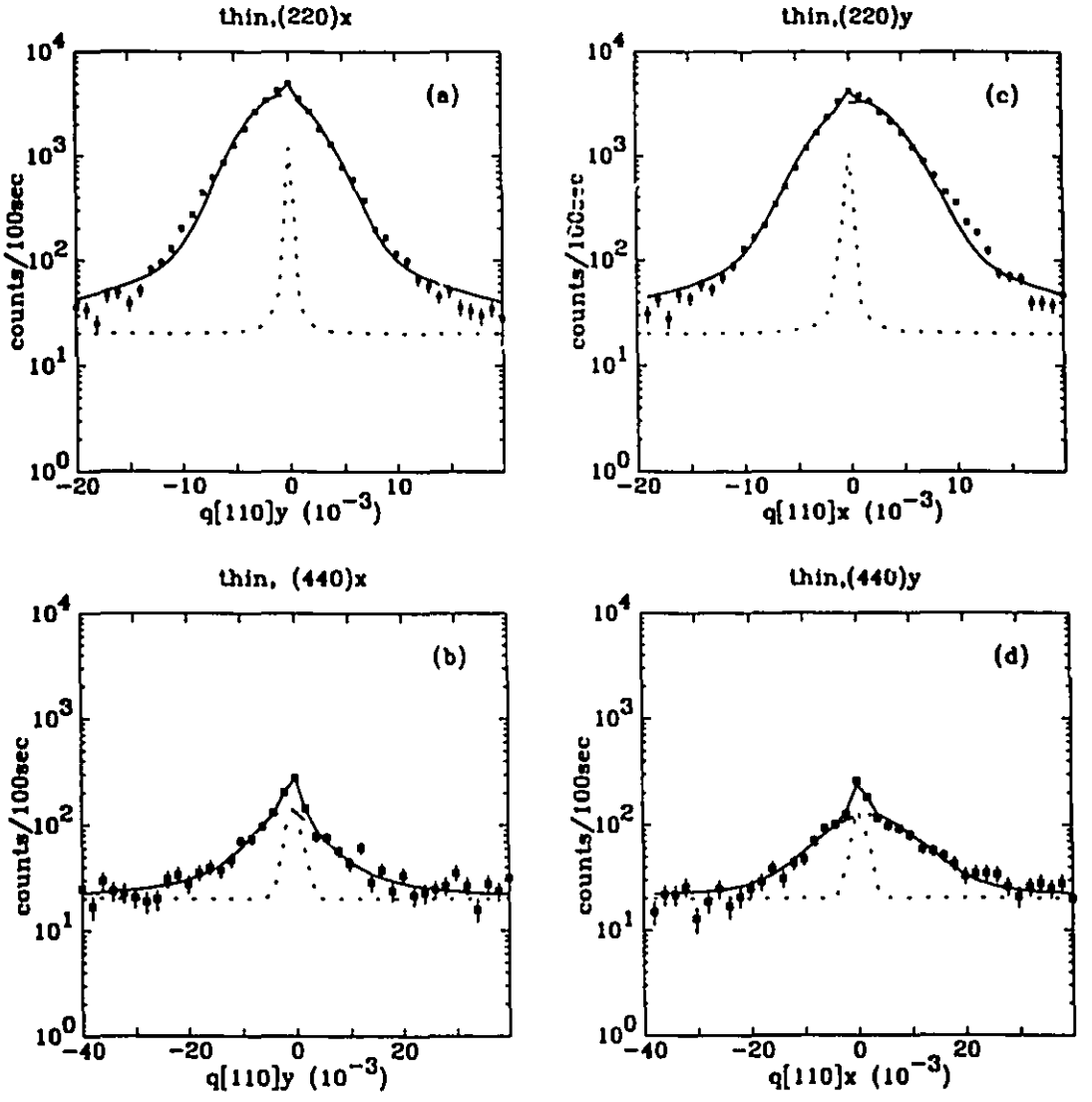

Figure 4.15: In-plane structure of the thin sample with q_t scans. (a) The $(220)_x$ peaks. (b) The $(440)_x$ peaks. (c) The $(220)_y$ peaks. (d) The $(440)_y$ peaks. The ratios of maximum intensities of epi-peaks to substrate peaks are determined by the corresponding fitting of q_t scans, as shown in Figure 4.14. The solid lines are the fitting curves, the dashed lines are the epi-peaks and the dotted lines are the substrate peaks.

The more quantitative analysis of the peaks of the epilayer is given by fitting the peaks along both q_l and q_t axes through the intensity maximums, as shown in Figure 4.14 and Figure 4.15 respectively. The fitting of the longitudinal and transverse scans of the $(220)_x$ peaks indicates that the peak of the $Ga_{1-x}In_xAs$ epilayer is located at 2.2193[110]$Å^{-1}$ with HWHM widths 0.0052[110]$Å^{-1}$ along $q[110]x$ and 0.0036[110]$Å^{-1}$ along $q[110]y$. The residue incommensurability between the thin epilayer and the GaAs substrate is 0.18%. As described in Section 2.2, this incommensurability usually results in a modulated structure at the epitaxial interface, which will be discussed later.. The in-plane strain of the thin epilayer at the interface is measured to be 1.13% along $(110)_x$ axis. The in-plane strain along the $(110)_y$ axis is the same, except the 0.03° misorientation of the peaks of the epilayer with respect to those of the GaAs substrate. The HWHM widths of the $(220)_y$ peak of the thin epilayer is 0.0046[110]$Å^{-1}$ along $q[110]y$ and 0.0043[110]$Å^{-1}$ along $q[110]x$.

The $(440)_x$ and $(440)_y$ peaks are fit in the same way as for the $(220)_x$ and $(220)_y$ peaks by accounting for the dispersive effect (ref: Section 3.3). By doubling the positions of the $(220)_x$ and $(220)_y$ epi-peaks, the peak widths of the $(440)_x$ and $(440)_y$ of the epilayer are evaluated. The HWHM widths of the $(440)_x$ epi-peak are 0.0097[110]$Å^{-1}$ along q[110]x and 0.0064[110]$Å^{-1}$ along q[110]y respectively. The HWHM widths of the $(440)_y$ epi-peak are 0.0094[110]$Å^{-1}$ along q[110]x and 0.0080[110]$Å^{-1}$ along q[110]y respectively. The broadening of the peak widths at higher order scattering indicates the non-uniform strain at the epitaxial interface. The contours and scans also show that the peaks of thin epilayer are broader along q[110]x than along q[110]y.

Figure 4.16 shows more contours of the in-plane Bragg peaks of the thin sample. The peak represented the vector summation of $(220)_x$ peak and $(220)_y$ peak in the preferential quadrant is denoted as (400) peak and shown in Figure 4.16 (a), and the peak represents the vector subtraction of $(220)_x$ and $(220)_y$ is denoted as (040)

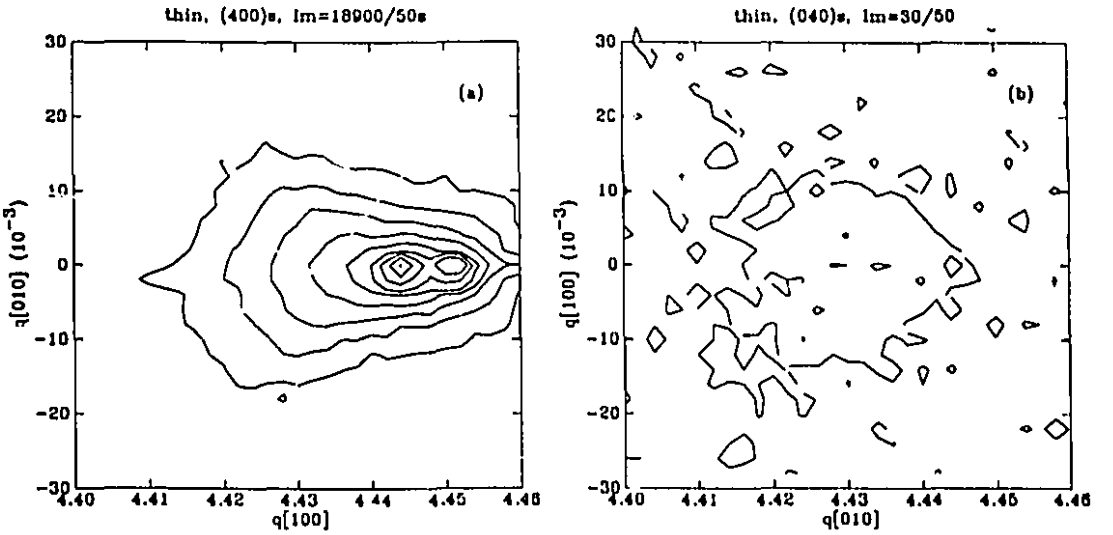

Figure 4.16: More contours of the in-plane Bragg peaks of the thin sample. (a) The (400) peaks. (b) The (040) peaks. The (400) peaks are located within the preferential quadrant and strong, while the (040) peaks are not located in the preferential quadrant and weak. The (040) substrate peak does not appear.

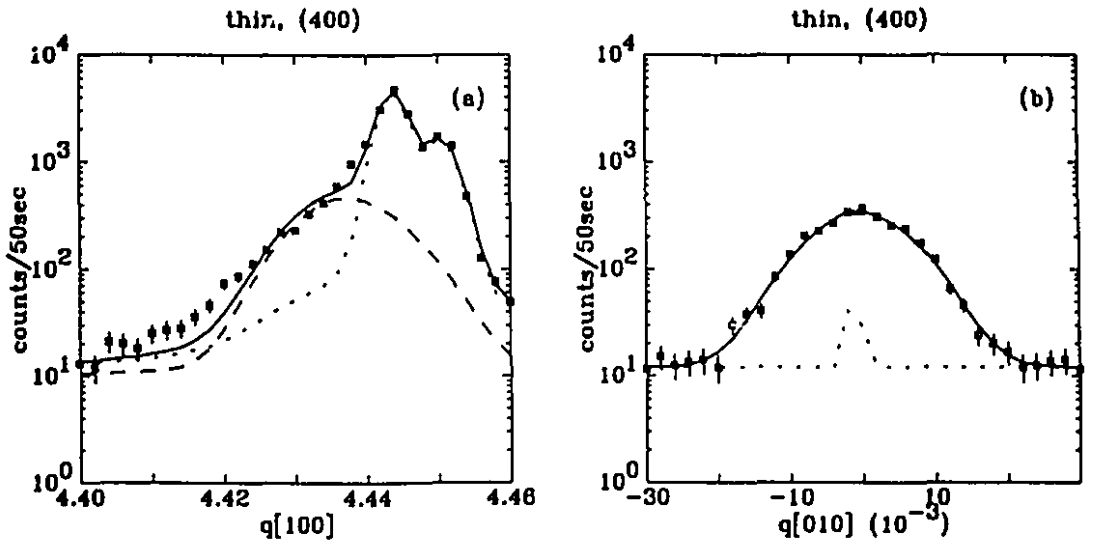

Figure 4.17: In-plane structure of the thin sample with (400) peak fiting. (a) The fitting of q_l scan. (b) The fitting of q_t scan. The solid lines are the fitting curves, the dashed lines are the epi-peaks and the dotted lines are the substrate peaks.

peak and shown in Figure 4.16 (b). Comparing with the (400) peak, the intensity of the (040) peak is much weaker because of the surface miscut which produces a preferential quadrant for glancing incidence x-ray scattering. The shape of (400) or (040) peak may be considered as two peaks superimposed on each other with a small shift in position, or it may have an assymetric single peak due to the in-plane microstructure. To fit the scans to EWGL curves, the HWHM widths of the (400) peak of the epilayer are evaluated to be $0.0075[100]\text{Å}^{-1}$ in q_t scan and $0.0079[010]\text{Å}^{-1}$ in q_t scan, as illustrated by Figure 4.17. The width of the GaAs substrate peak is bigger than the resolution limit because of the GIXS geometry.

As mentioned earlier, it seems that there is some "extra" scattering at the low $q[110]x$ side of the $(220)_x$ peak of the thin epilayer, which can not be fit exactly to a EWGL curve. These "extra" counts can be fit by adding another EWGL curve, which is peaked at $2.213[110]x$ with HWHM width $0.0107[110]\text{Å}^{-1}$, as shown in Figure 4.18. Because of its smaller q and broader HWHM width comparing with the peak at $2.219[110]x$, this part of scattering may be attributed to the epilayer near the top surface, which can be less strained by the GaAs substrate than that near the epitaxial interface. If this is correct, an in-plane structural evolution of the epilayer along the direction of growth is suggested. The evolution can be possibly studied by changing the penetration depth of x-rays in glancing incidence scattering.

Figure 4.19 shows the x-ray penetration depth to the thin sample as the out-of-plane component of the x-ray momentum transfer changes along the surface normal of the sample. The solid line is the penetration depth to the epilayer and the dashed line is the penetration depth in the substrate. The penetration depth of the x-ray evanescent wave is 21Åwhen the incident angle is zero, *i.e.*, $q_z = 0$. In principle, the total external reflection will occur up to $q_z = 0.053\text{Å}^{-1}$. The reflectivity can be significantly less than one because of the absorption and surface roughness, as discussed in last subsection. There is no total external reflection at the epitaxial

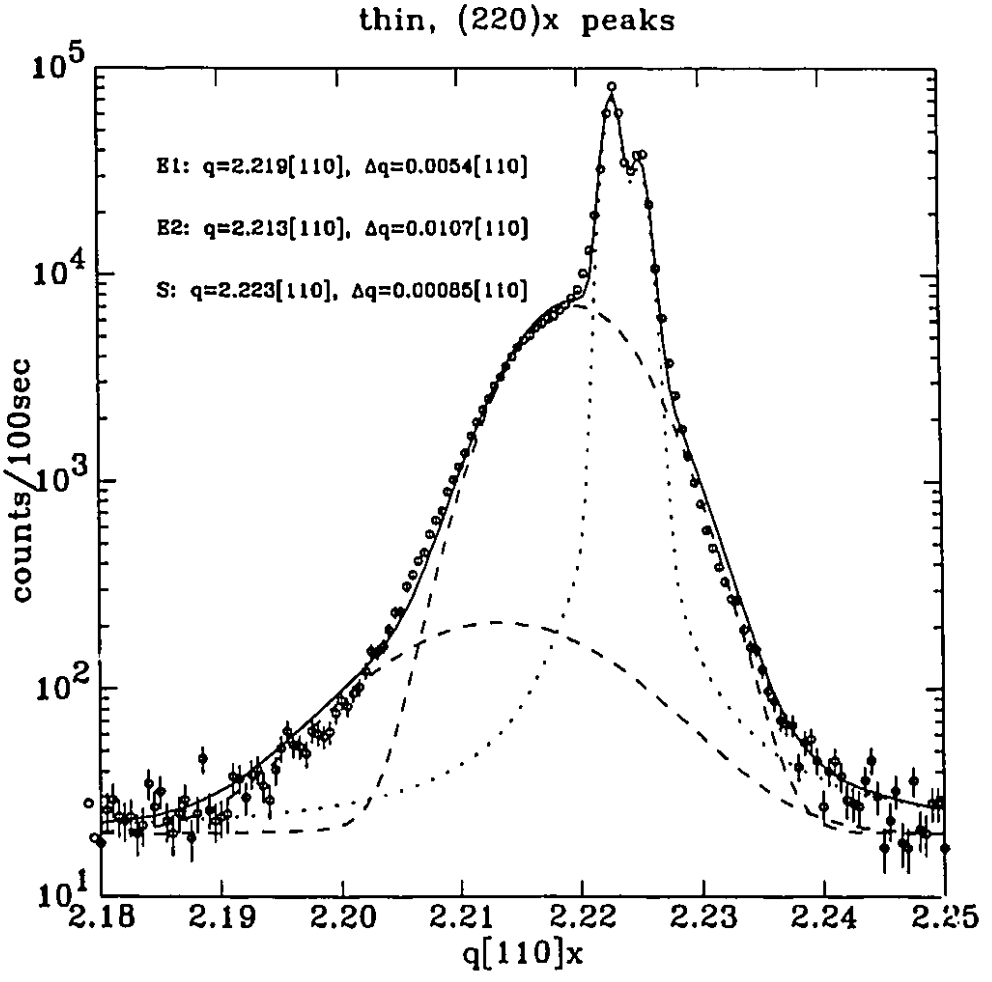

Figure 4.18: The in-plane structure of the thin sample. The asymmetric scattering at lower $q_{\parallel}$ side of (220) peak can be fit by another peak. This peak is located at 2.213[110]Å^{-1} with width twice broader than the epi-peak located at 2.219[110]Å^{-1}. This part of scattering can be attributed to the partially relaxed epilayer on the surface of the sample.

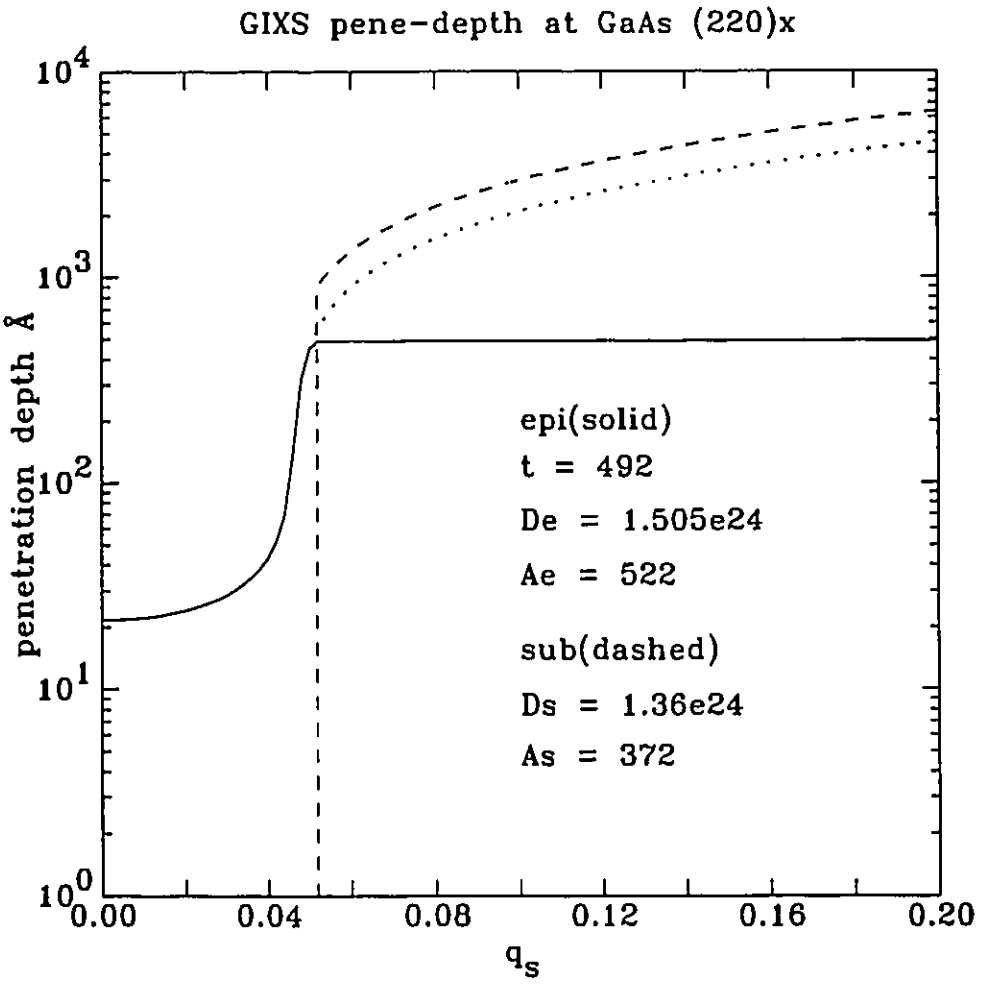

Figure 4.19: The calculated x-ray penetration depth of GIXS geometry at GaAs $(220)_x$ of the thin sample. The solid line is the penetration depth in the epilayer, and the dashed line is the penetration depth in the substrate. The electron density and linear absorption coefficient of the epilayer are $1.505 \times 10^{24}/cm^3$ and $522/cm$, and its thickness is 492Å. The electron density and linear absorption coefficient of the substrate are $1.36 \times 10^{24}/cm^3$ and $372/cm$ respectively. These parameters are obtained from the fitting of the reflectivity curve, as shown in Figure 4.9.

interface because the substrate is not a less dense optical medium for x-rays with respect to the epilayer. The values of electron densities and the absorption coefficients of the epilayer and the substrate used in this calculation are taken from literature [23]. The values obtained in reflectivity measurements (ref: Section 4.2.2) make little change in evaluating the x-ray penetration depth.

Figure 4.20 shows the in-plane structure depth profiling carried out along the $(220)_x$ scattering rod. The integrated intensity of the $(220)_x$ epi-peak of the thin sample reachs the maximum at $q_z = 0.07\text{Å}^{-1}$, and that of the $(220)_x$ substrate peak reachs the maximum at $q_z = 0.08\text{Å}^{-1}$ (ref: Figure 4.12). Because the scattering rod is misaligned with the q[001] axis of the sample, the geometrical correction is required in fitting the positions of Bragg peaks. All profiles of the scattering can be fit to the three peak model used in Figure 4.18, in which one peak is located at $q = 2.223[110]\text{Å}^{-1}$ for the substrate, two peaks for the epilayer are located at $q = 2.213[110]\text{Å}^{-1}$ and $q = 2.219[110]\text{Å}^{-1}$ respectively. At $q_z = 0.02\text{Å}^{-1}$, the penetration depth of x-rays is about 21Å, as illustrated by Figure 4.19, and the scattering intensity of x-rays is dominated by the epilayer at the surface. As the penetration depth increases with q_z, more and more scattering due to the bottom part of the epilayer and the substrate is measured.

Figure 4.21 shows the evolution of integrated intensities due to the three parts scattering of the thin sample along q_z. The scattering intensity is mainly due to the epilayer when the penetration depth of the x-ray evanescent wave is small. The intensity of the top part of the epilayer increase slow with q_z and soon gets saturated at $q_z = 0.07\text{Å}^{-1}$ because of its limited thickness. The scattering intensities of the epilayer near the interface and the substrate increases faster with q_z. The ratio of the integrated intensities from different parts of materials can be used to evaluate the amount of materials which scatter x-rays. Based on the positions and integrated intensities of these peaks, we find that the thin epilayer is strongly strained in-plane

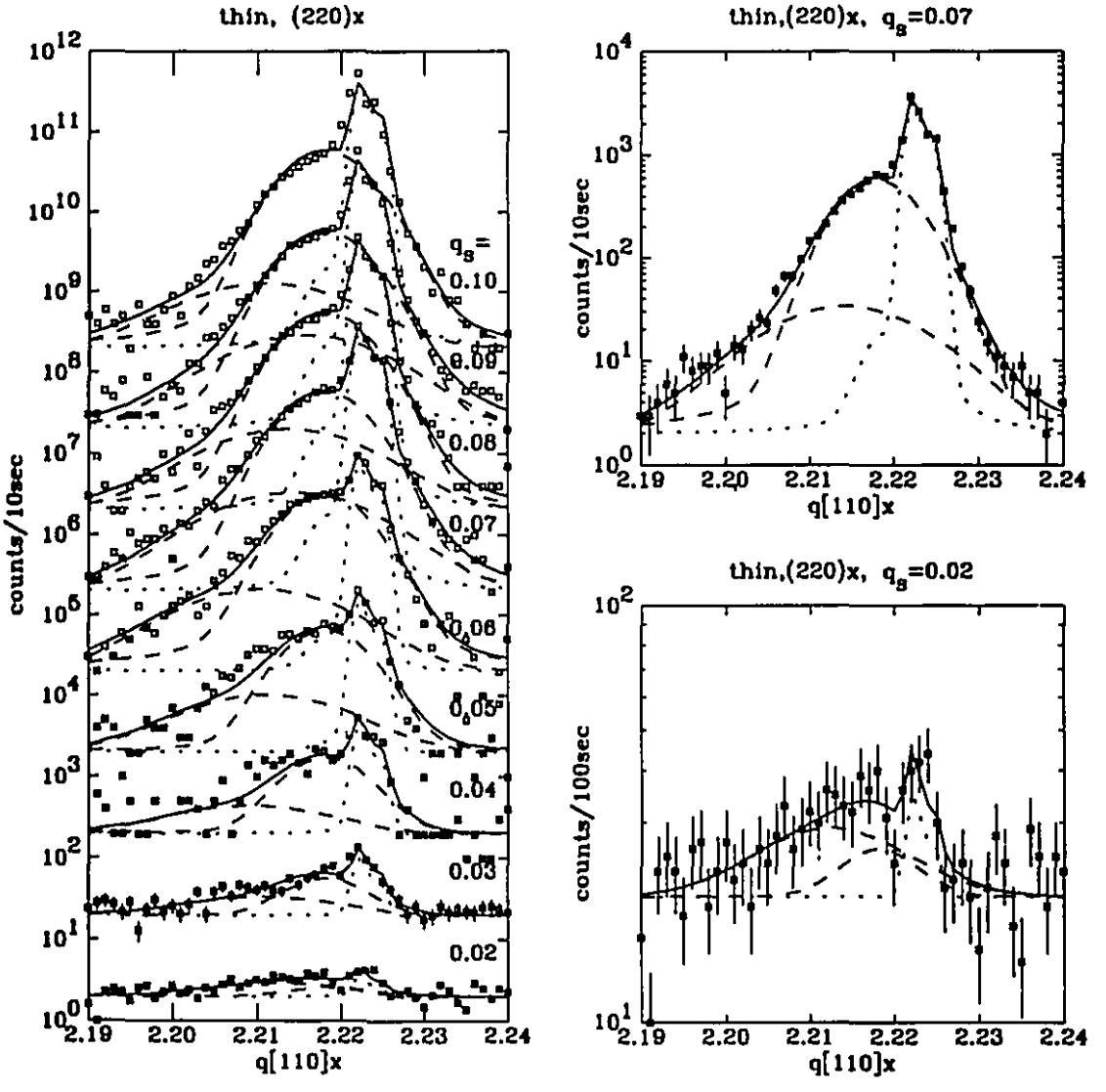

Figure 4.20: The depth profiling of in-plane q_x scans of $(220)_x$ peaks of the thin sample along q_z. This is the depth profiling along the truncation rod of $(220)_x$ peaks. q_z starts from 0.02Å^{-1}. The scattering intensity of the epilayer reachs the maximum at $q_z = 0.07\text{Å}^{-1}$.

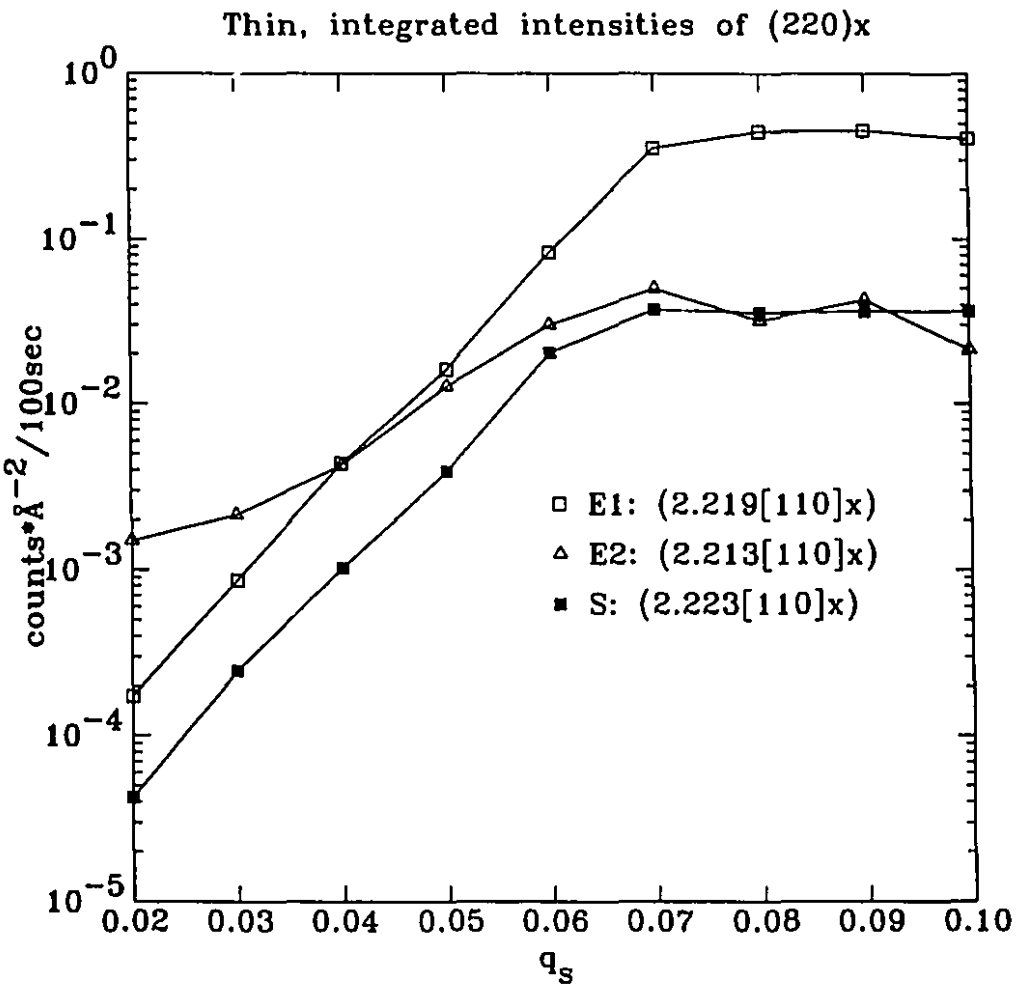

Figure 4.21: The integrated intensities of the three parts of scattering of the thin sample $(220)_x$ peaks. The scattering of the top surface of the epilayer, denoted as E2, is larger than that of the epilayer near the interface and of the substrate at small q_z, but increases slower with q_z due to its limited thickness and reachs the intensity maximum at $q_z = 0.07\text{Å}^{-1}$. The ratio of integrated intensities can be used to evaluate the amount of materials which scatter x-rays. The plots of integrated intensities also provide a low resolution information on the out-of-plane widths of $(220)_x$ peaks which are reciprocal to their thicknesses.

to match the substrate. But it remains 0.18% incommensurability to the GaAs substrate near the interface up to 400Å, and this residual incommensurability is relaxed to 0.45% near the surface of the epilayer. The out-of-plane footprint correction will raise the scattering intensity at small q_z, as indicated by Equation 3.29, but its correction to the ratio of integrated intensities of different parts can be ignored.

Figure 4.22 shows the contours of the in-plane Bragg peaks of the thick sample. With the geometry of glancing incidence x-ray scattering, the in-plane peaks of the GaAs substrate can not be seen because x-rays can not penetrate the thickness of the epilayer (ref: Figure 4.19. The axes of the sample coordinate system have been defined with the $(220)_x$ and $(220)_y$ substrate peaks from the edges of the sample. The sample is translated horizontally after setting the orientation matrix to perform the glancing incidence scattering. The reference coordinates can also be examined and corrected by means of the $(331)_x$ and $(331)_y$ substrate peaks to make sure the orientation matrix has been correctly set. Optimizing the intensity of $(220)_x$ peak with χ-circle gives the value of χ of 0.488°. This value means the angle between the incident x-rays and the surface of the sample is $\alpha_i = 0.188°$. With the same value set on χ-circle, the out-of-plane components of the momentum transfer q are $q_z = 0.026[001]\text{Å}^{-1}$ for the $(220)_x$ and $(220)_y$ epi-peaks, and $q_z = 0.053[100]\text{Å}^{-1}$ for the (400) epi-peak, which is located in the preferential quadrant of this sample. The (040) peak is not located in the preferential quadrant, and its scattering is optimized at $q_z = 0.0[001]\text{Å}^{-1}$ with maximum intensity of 100 counts per 100 seconds. The weak scattering of (040) epi-peak is merely used as a reference here. The shapes of all the in-plane peaks are consistent and clearly indicate the in-plane asymmetry and the uniaxial microstructure of the thick epilayer along $\langle 110\rangle_x$ axis.

The q_l and q_t scans of the in-plane peaks of the thick epilayer are fit to EWGL curves, as illustrated in Figure 4.23 and Figure 4.24 respectively. The $(220)_y$ peak is located at $2.20[110]\text{Å}^{-1}$ with HWHM width $0.003[110]\text{Å}^{-1}$ along $\langle 110\rangle_y$ axis.

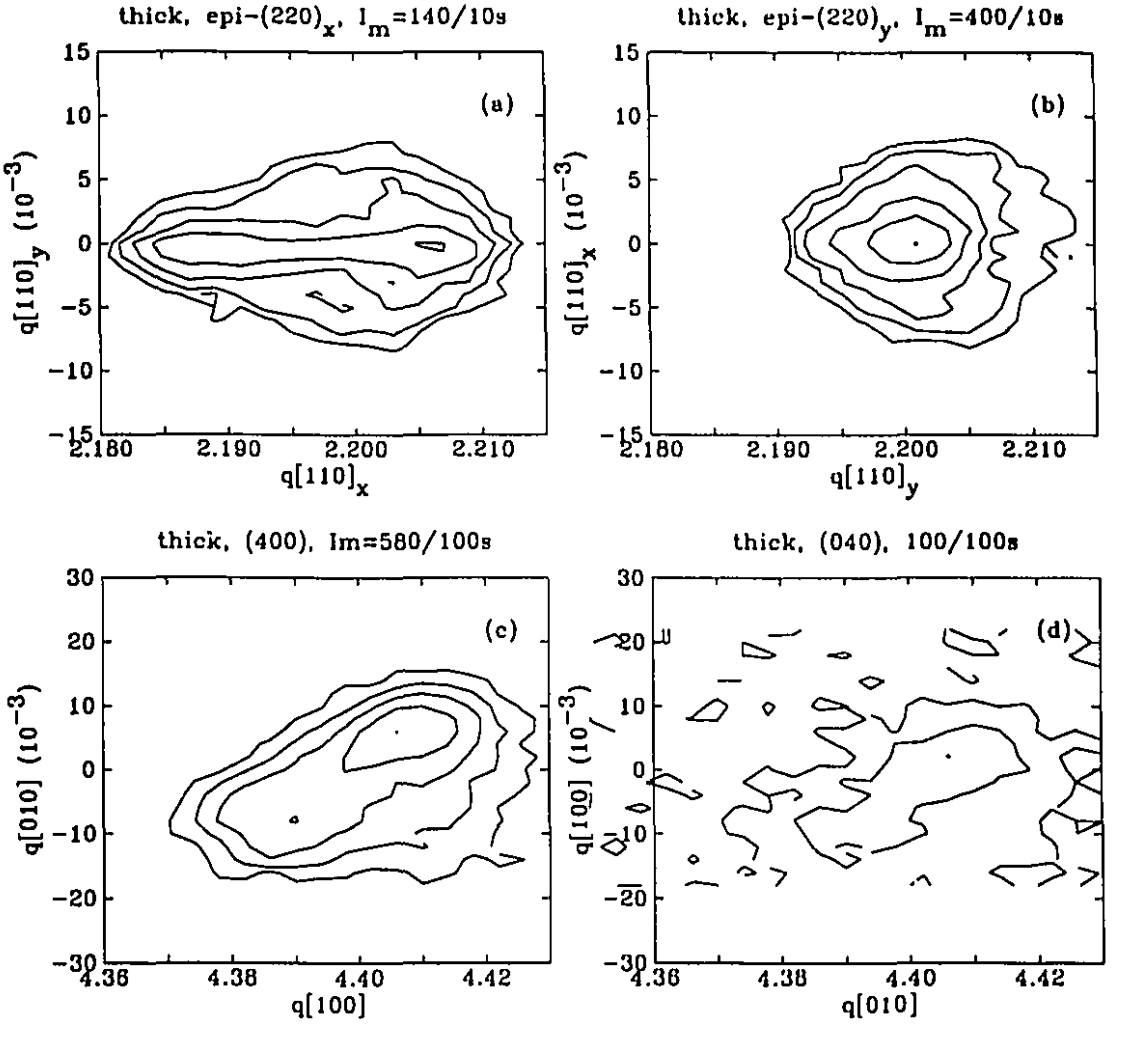

Figure 4.22: Contours of in-plane Bragg peaks of the thick sample. (a) q_l-q_t mesh of the $(220)_x$ epi-peak. (b) q_l-q_t mesh of the $(220)_y$ epi-peak. (c) q_l-q_t mesh of the (400) epi-peak. (d) q_l-q_t mesh of the (040) epi-peak. The shapes of the peaks indicate the good atomic ordering along $(110)_y$ axis and modulated structure along $(110)_x$. The (400) peak is located at the preferential quadrant and demonstrates a combined structural feature of the $(220)_x$ and $(220)_y$ peaks.

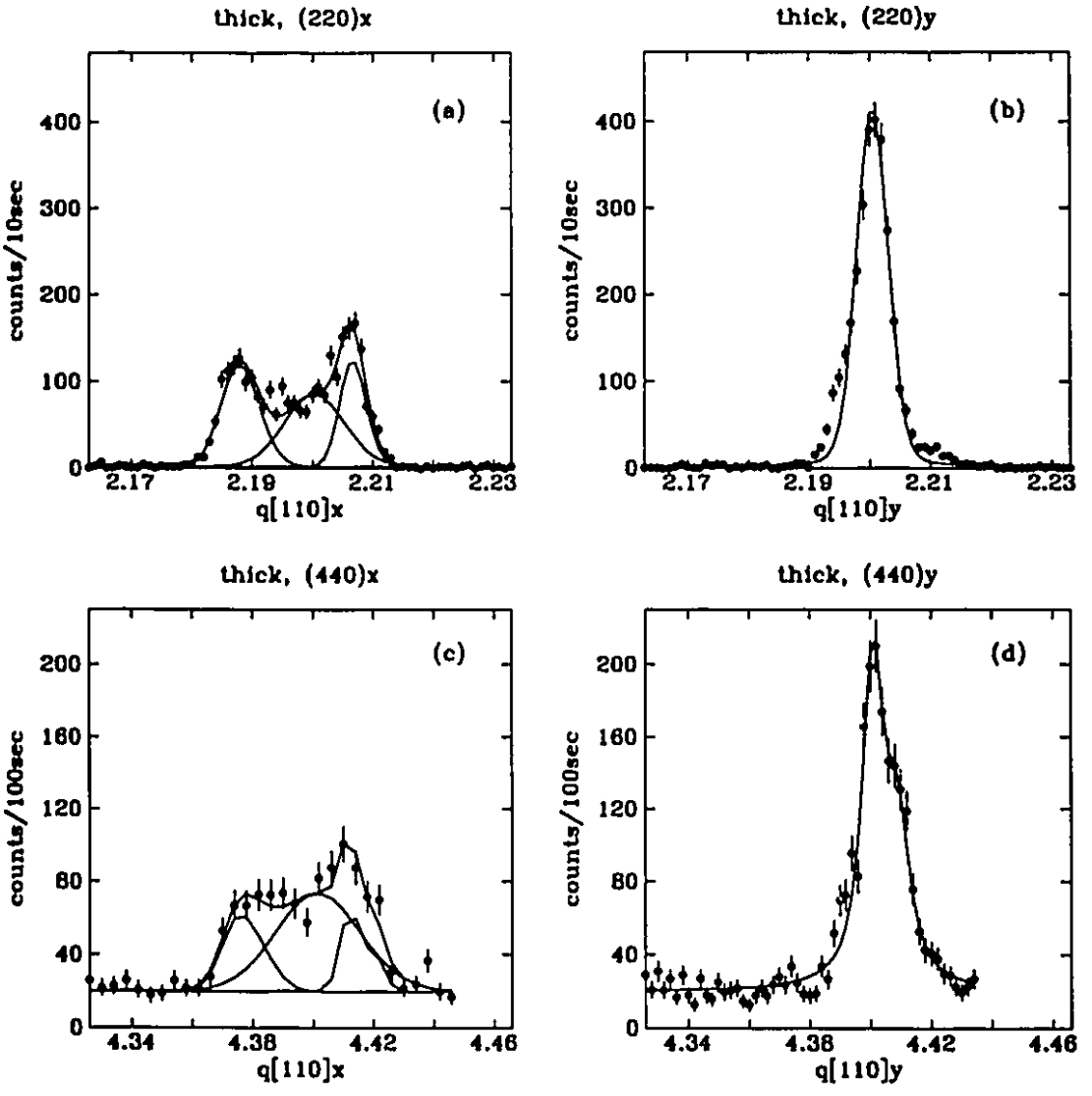

Figure 4.23: In-plane structure of the thick sample with q_l scans. The $(220)_y$ and the $(440)_y$ epi-peaks can be fit to single EWGL curves. The positions of the peaks along (110) indicate the complete structural relaxation along this axis, and the widths of these peaks indicate the good atomic ordering. The scattering along $(110)_x$ can be fit to three EWGL curves. The three peaks are weighted averaged at the positions indicated by Vegard's law, *i.e.*, the same positions as along $(110)_y$ axis.

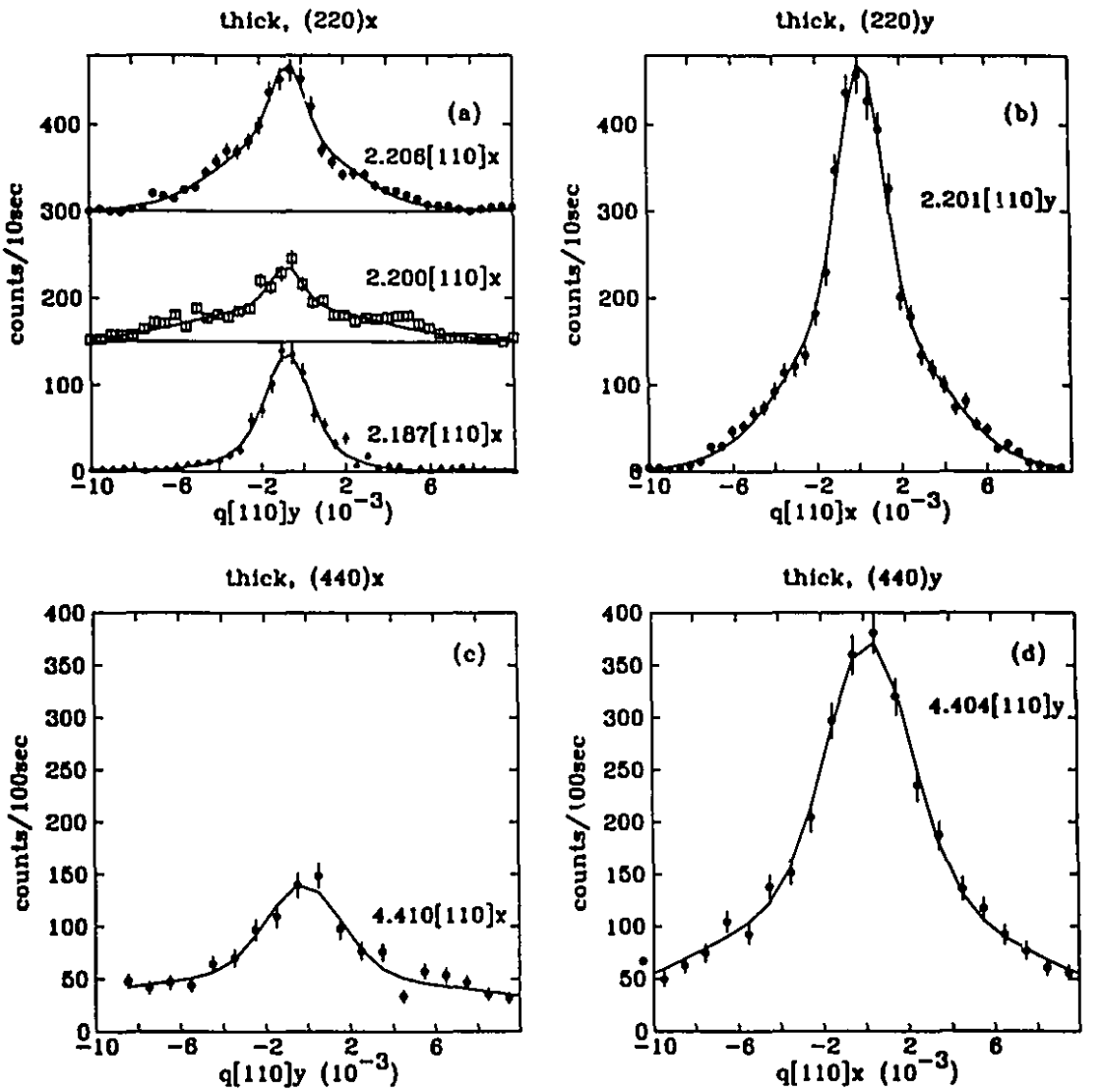

Figure 4.24: In-plane structure of the thick sample with q_l scans. (a) $(220)_x$ epi-peak. The three curves shown in (a) have been taken at q_l = 2.187[110]x, 2.200[110]x and 2.206[110]x respectively. Their shapes, positions and intensity ratios have also been indicated in the contours and q_l scan. (b) $(220)_y$ epi-peak at q[110]y = 2.201[110]Å^{-1}. (c) $(440)_x$ epi-peak at q[110]x = 4.410[110]Å^{-1}. The $(440)_x$ epi-peak demonstrates the same feature as the $(220)_x$ epi-peak, but only one transverse scan is shown because its weak intensity. (d) $(440)_y$ epi-peak at q[110]y = 4.404[110]Å^{-1}.

The transverse scan of this peak have been fit to two Gaussians centered at the same position, and their HWHM widths are 0.0012[110]Å^{-1} and 0.0038[110]Å^{-1} respectively. The q_l scan of the $(440)_y$ epi-peak is located at 4.40[110]Å^{-1} with HWHM width 0.0042[110]Å^{-1}. The double Gaussian HWHM widths of the q_t scan of the $(440)_y$ epi-peak are 0.0023[110]Å^{-1} and 0.0076[110]Å^{-1} respectively. The shapes of the $(220)_x$ and $(440)_x$ peaks are complicated, and the q_l scans can be fit to three EWGL curves. For the $(220)_x$ scattering, one peak is located at 2.20[110]Å^{-1} with longitudinal HWHM width 0.0056[110]Å^{-1} and transverse HWHM width 0.0046[110]Å^{-1}. This peak agrees with the peak along $\langle 110\rangle_y$ axis. The second one is centered at 2.187[110]Å^{-1} with longitudinal width 0.0034[110]Å^{-1} and transverse width 0.001[110]Å^{-1}. The third one is centered at 2.206[110]Å^{-1} with longitudinal width 0.0022[110]Å^{-1} and transverse width 0.001[110]Å^{-1}. The total integrated intensity of $(220)_x$ scattering agrees with that of $(220)_y$ scattering the thick epilayer. The $(440)_x$ epi-peak has been fit in the same way. The first peak is centered at 4.3992[110]Å^{-1} with longitudinal width 0.015[110]Å^{-1} and transverse width 0.0093[110]Å^{-1}. The second peak is centered at 4.3745[110]Å^{-1} with longitudinal width 0.0063[110]Å^{-1} and transverse width 0.002[110]Å^{-1}. The third peak is centered at 4.412[110]Å^{-1} with longitudinal width 0.0036[110]Å^{-1} and transverse width 0.002[110]Å^{-1}.

Figure 4.25 shows the in-plane structure depth profiling of the $(220)_x$ peak of the thick epilayer. As expected, the $(220)_x$ peak of the substrate can not be seen. The overall scattering intensity of $(220)_x$ in-plane epi-peak is maximized at q_s = 0.04Å^{-1}, which is equivalent to q_z = 0.026[110]Å^{-1} by accounting for the surface miscut. The depth profiling of this peak shows that the scattering profile of the epilayer slightly evolves as the penetration depth of x-rays increases.

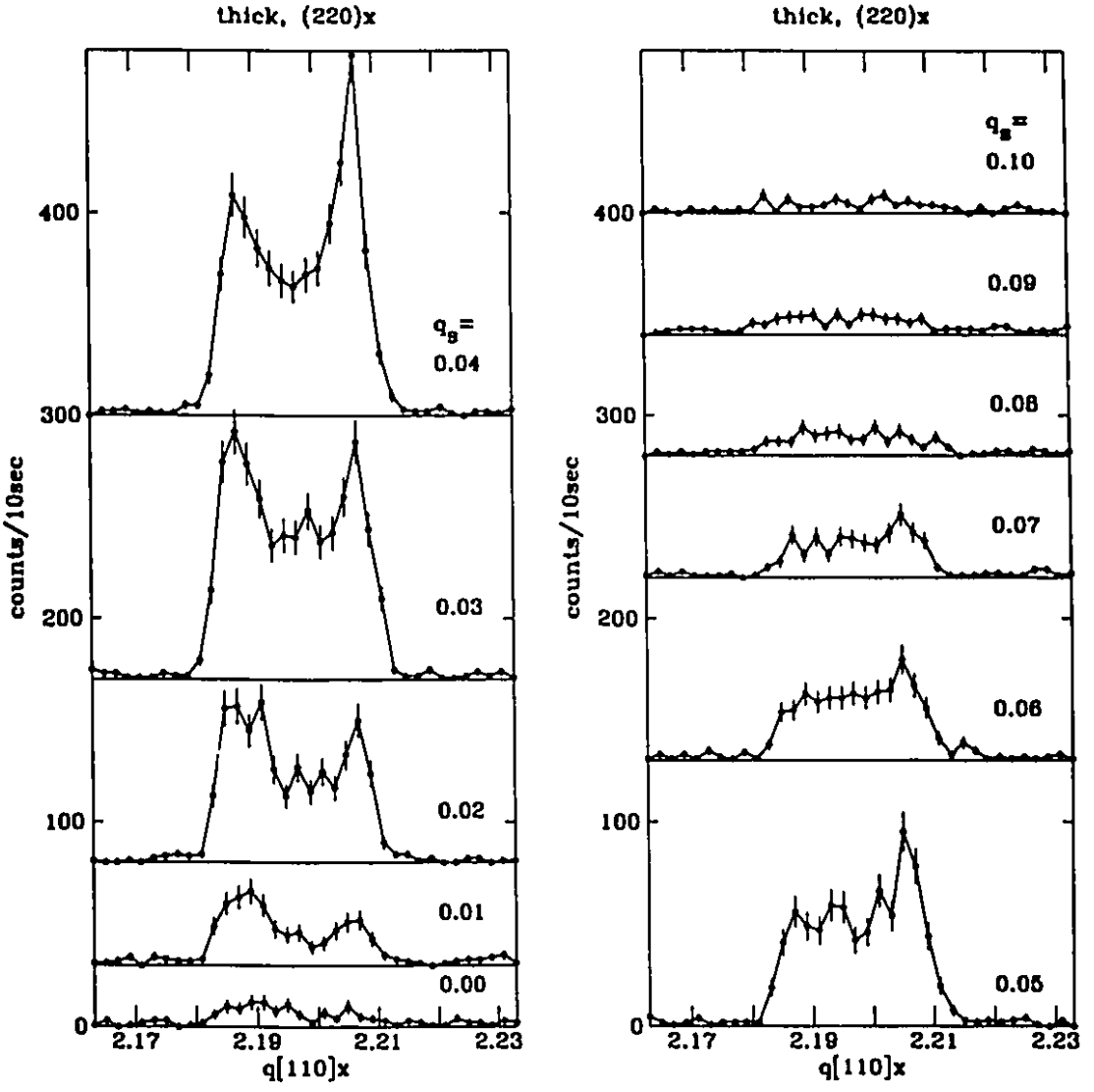

Figure 4.25: In-plane depth-profiling of $(220)_z$ epi-peak of the thick sample. The $(220)_z$ substrate peak of this sample, which should locate at $q_l = 2.223[110]\text{Å}^{-1}$, can not be seen because the x-ray can not penetrate the thick epilayer.

4.3 The Analysis

4.3.1 General Characterization

All of the out-of-plane and in-plane data presented in last section for both of the thick sample and the thin sample have been schematically summarized in Figure 4.26 and Figure 4.27 respectively. A general structural characterization which is mainly based on the analysis of the positions and widths of Bragg peaks is presented in this subsection.

As illustrated by both Figure 4.26 and Figure 4.27, the Bragg peaks of the GaAs substrates are sharp and intense, and located at the positions as expected. The Bragg peaks of the GaAs substrates have been used to define the reference frame in our measurement and have also provided an accurate determination of the lattice constant of the GaAs crystals used in our samples. This lattice constant has been measured to be 5.6531(3)Å. The resolution limited widths of the Bragg peaks of the GaAs substrates indicate their structural perfection.

Since the structure and lattice constant of the GaAs substrates are well defined, the structure and lattice constants of the epilayers can be evaluated by their scattering with respect to that of the substrates, or evaluated independently because the reference frames have been defined. The location of the scattering maxima of the epilayer in reciprocal space as shown in Figure 4.26 and Figure 4.27 indicates that the structures of epilayers can be regarded same as that of the GaAs substrates, but with different lattice parameters. These lattice parameters can be different in-plane and out-of-plane with respect to the epitaxial interfaces if macrostrains exist.

The average lattice constant of the thick epilayer is 5.717(4)Å, based on the evaluation of the average positions of the out-of-plane and in-plane peaks. According to the Vegard's law, as indicated by Equation 2.19, the In composition of the thick epilayer is calculated to be 15.8%, which is fairly close to the value previously

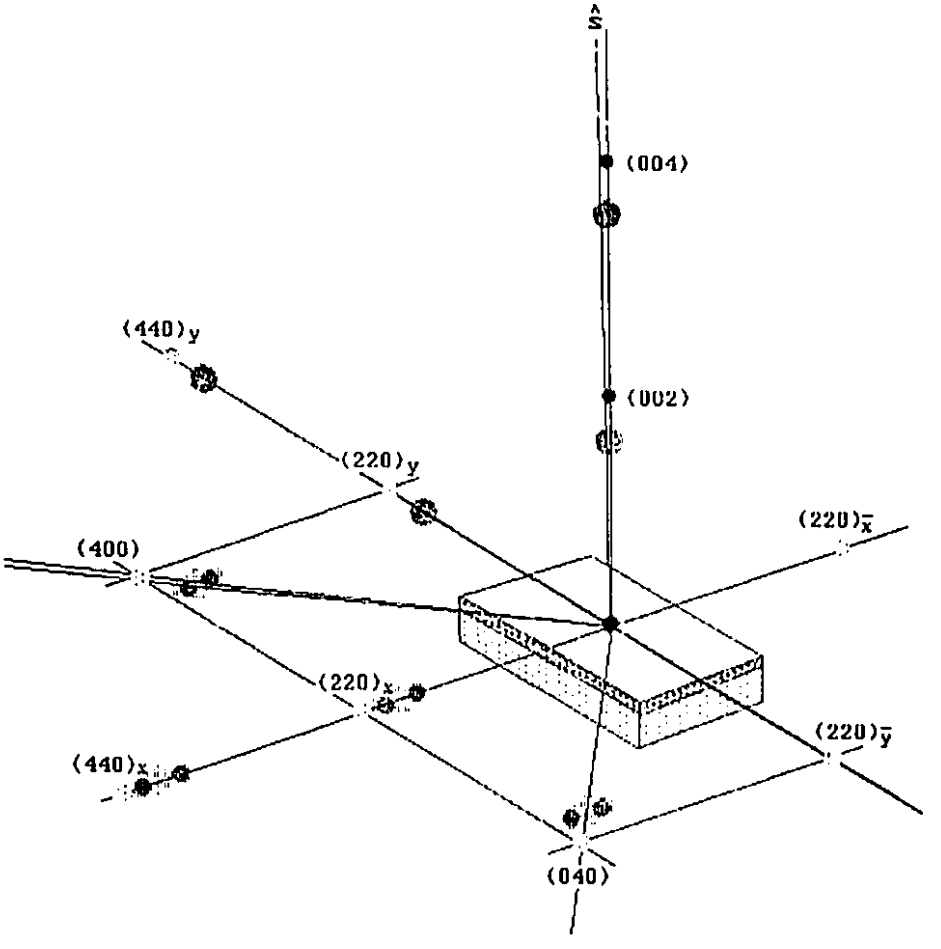

Figure 4.26: The schematic summary of the thick sample. The in-plane peaks of the GaAs substrate can not be seen. The average lattice constants of the thick epilayer evaluated by both out-of-plane and in-plane epi-peaks agree with the value of equilibrium bulk state within 0.07%, which indicates a nearly complete structural relaxation. The shapes of epi-peaks along $\langle 110 \rangle_z$ axis suggest an uniaxial displacive modulation. The in-plane grey spots along $\langle 110 \rangle_z$ denote the average peak positions witch agree with the peak positions along $\langle 110 \rangle_y$. The misalignment of the scattering maxima of the epilayer and the substrate in y-z plane can be interpreted as a tilt of the crystal planes or the microstructure of the epilayer.

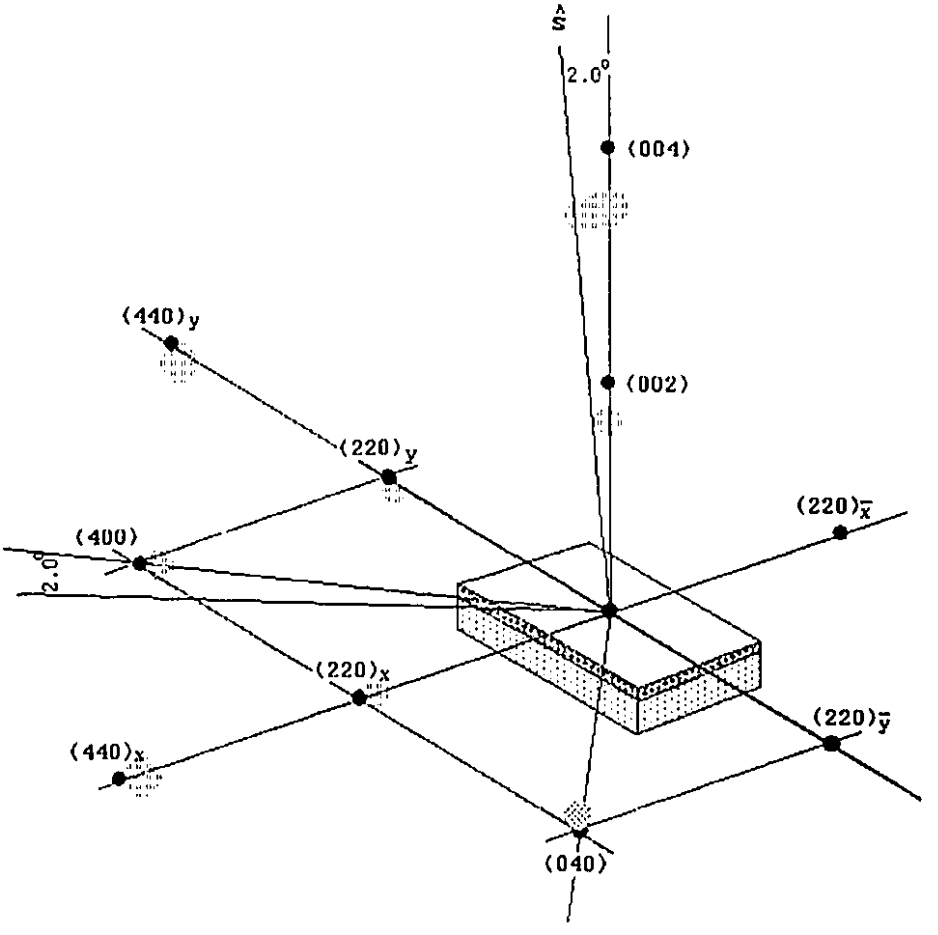

Figure 4.27: The schematic summary of the thin sample. All the Bragg peaks of the epilayer are considerably broader than that of the GaAs substrate, which are resolution limited. The in-plane peaks of the epilayer shift towards that of the substrate and reduce the incommensurability from 1.36% to 0.18%. The out-of-plane peaks of the epilayer shift away from that of the substrate and leads to 1.28% strain along the direction of growth. The (004) peak of the epilayer has a sharp spike and a broad shoulder, which is asymmetric in x-z plane, and quite symmetric in y-z plane of the reciprocal space. This shape of scattering suggests an asymmetric microstructure of this epilayer.

estimated. The In composition of the epilayer can also be evaluated by the reflectivity measurement in which the critical angle of the specular reflection is determined by the electron density of the epilayer. The electron density of the thin epilayer evaluated by this method, as presented in Section 4.2.2, is about 1.1% larger than that calculated by Vegard's law with weighted average of 19% In composition. This discrepancy may be attributed to the strain effect which increases the electron density, or in other words, decreases the volume of unit cells of the epilayer. The average volume of an unit cell of the thin epilayer can be evaluated by the positions of Bragg peaks. The in-plane peaks of the thin epilayer shift towards that of the substrate and reduce the incommensurability from 1.36% to 0.18%. The out-of-plane peaks of the epilayer shift away from that of the substrate and result in a 1.28% lattice expansion along the direction of growth. This shift of peak position suggests a tetragonal distortion of the thin epilayer, and the Poisson's ratio is evaluated to be 0.36. This value of Poisson's ratio is about 12% larger than that previous reported for this system [85] (ref: Section 4.2.1). The directly measured in-plane lattice constant is 5.6631(2)Å, and out-of-plane lattice constant is 5.8037(1)Å. The percentage difference of the unit cell volumes between the strained thin epilayer and the equilibrium state of $Ga_{0.81}In_{0.19}As$ (a = 5.7303Å) is calculated to be -1.08%, which agrees fairly well with the increase of electron density in the epilayer evaluated by reflectivity measurements.

Even though the thick epilayer has been considered as nearly completely relaxed for evaluating the lattice constant of its equilibrium state, the data have revealed more structural detail, such as an asymmetry and satellite peaks, which may be particular to the epilayers and require special analysis. As shown in Figure 4.26 and Figure 4.27, both of the thick and the thin epilayers have demonstrated an asymmetrical in-plane structures, such as that the shapes of the in-plane Bragg peaks are different along axes x and y, or the out-of-plane Bragg peaks are different

in the two perpendicular transverse scans. The structural characterization will be started with the scattering in the y-z plane of the thick sample, because it seems have the simplest structural features.

According to the out-of-plane measurement, as shown in Figure 4.3, the thick epilayer can be separated as two structural regions. Region I has lattice constant $a_z = 5.7218(2)\mathring{A}$, and is about $2.7\mu m$ near the top surface of the thick sample. Region II has lattice constant $a_z = 5.7306(5)\mathring{A}$, and is about $1.3\mu m$ near the epitaxial interface. The structural regions of the thick sample in y-z plane has been schematically illustrated by Figure 4.28. A subregion of about $0.02\mu m$ thick at the top surface of the sample, labelled as region Ia in the figure, is defined by the penetration depth of the x-rays in glancing incidence scattering. Region Ia is used for convenience, which implies that only the in-plane lattice constant in this region has been actually measured, and this lattice constant can be different with other parts of the thick epilayer.

As indicated by the data of reflectivity measurement presented in Section 4.2.2, the surface normal of the thick sample is misaligned with the $\langle 001 \rangle$ axis of the GaAs substrate by 0.14°, and the rms value of the surface roughness of the thick epilayer is 18Å as observed along $\langle 110 \rangle_y$ axis. The out-of-plane data for both (004) and (002) peaks demonstrate the centers of Bragg peaks of the thick epilayer are misaligned with that of the substrate by 0.07° towards the negative side of $\langle 110 \rangle_y$ axis. This misalignment can be interpreted as a tilt of the crystal plane of the epilayer around the $\langle 110 \rangle_x$ axis.

The domain size and microstrain of the epilayer can be evaluated by studying the widths of the Bragg peaks. Because the measured peaks of the epilayers are usually Gaussian-like (ref: Section 4.2), the peak widths of Bragg scattering, Δq can be evaluated by the formula [23]

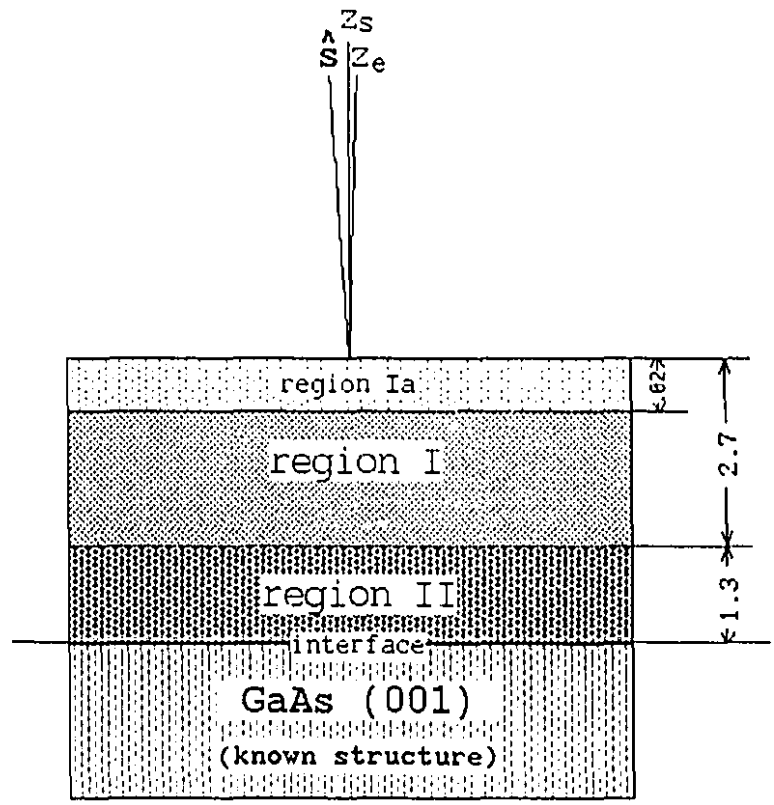

Figure 4.28: Regional structures of the thick epilayer in y-z plane. The region I and region II of the epilayer are identified by out-of-plane measurement, which have thicknesses of $2.7\mu m$ and $1.3\mu m$ respectively. Region Ia is part of region I is out-of-plane measurement, and is identified by the penetration depth of glancing incidence scattering. In actuality, the in-plane measurement with GIXS has been only performed in region Ia, which is approximated to $0.02\mu m$. The surface normal is misaligned with the (001) of the substrate by 0.14° and the crystal plane of the epilayer is tilted with respect to that of the substrate by −0.07°. The rms value of the surface roughness as viewed in y-z plane is $18\AA$.

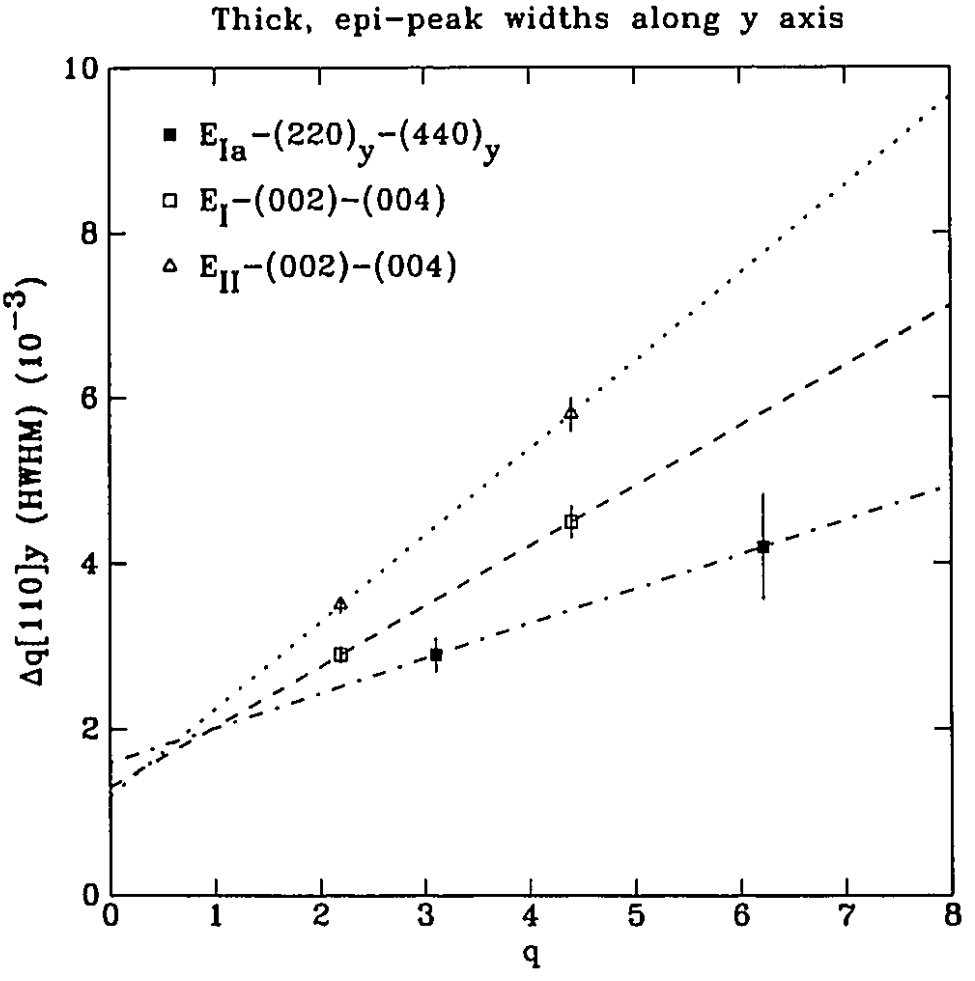

Figure 4.29: The epi-peak widths of the thick sample along y axis. The open squares and open triangles are the data points of normal Bragg scattering with q_t scans for region I and region II respectively. The full squares are the data points of glancing incidence scattering with q_l scans for region Ia. The domain sizes and microstrains in these regions can be evaluated according to Equation 4.5. The unit of momentum transfer q is Å^{-1}, and the unit of HWHM widths of the peaks, Δq, is $\sqrt{2}\text{Å}^{-1}$. The error bars denote the resolution limits of the setup.

$$\Delta q^2 = \Delta q_m^2 - \Delta q_r^2, \tag{4.4}$$

where Δq_m is the measured value and Δq_r is the instrumental resolution, as illustrated in Figure 3.6. All the widths of peaks used in this thesis are HWHM values. In general characterization, the width of Bragg peak, Δq, can be principally attributed to size broadening and strain broadening. The size broadening is caused by the termination of coherence in the ordering of scatterers, which has the same effect to all Bragg peaks. The strain broadening is caused by positional deviation of individual scatterers from the regular ordering, which is proportional to the value of x-ray momentum transfer. The mathematical expression of the peak broadering can be written as the summation of these two parts of broadening [21,23].

$$\Delta q = \frac{0.94\pi}{p} + \left(\frac{\Delta a}{a}\right) q, \tag{4.5}$$

where p denotes the average domain size, and $\frac{\Delta a}{a}$ denotes the microstrain. The measured peak widths of the thick epilayer in y-z plane are illustrated by Figure 4.29. The slope of peak widths in terms of the value of q is used to evaluate the microstrain and the average domain size is obtained by the extrapolation of peak width at $q = 0$. The extracted structural parameters of the thick epilayer are presented in the following table, in which the subscripts denote the error bars.

	a_z(Å)	a_y(Å)	ϵ_z(%)	ϵ_y(%)	$\left(\frac{\Delta a}{a}\right)_z$(%)	$\left(\frac{\Delta a}{a}\right)_y$(%)
region Ia		5.7123_3		-0.07_2		0.06_1
region I	5.7218_2		0.07_2		0.05_1	0.10_1
region II	5.7306_5		0.24_2		0.22_2	0.15_1

As evaluated by the extrapolation of the peak widths of the out-of-plane measurement, the average domain sizes in region I and region II are about the same, 1650(100)$\AA$. The major difference to characterize the in-plane structures of the thick epilayer at region I and region II is their microstrains, as indicated by the values of $\left(\frac{\Delta a}{a}\right)_y$ in the table. This observation suggests that the strained epilayer near the epitaxial interface can be relaxed through the evolution of microstrains as the thickness of the epilayer increases without generating more dislocations. From the scattering the structural features of the thick epilayer along the $\langle 110\rangle_x$ axis are very different from those along $\langle 110\rangle_y$ axis, and can not be simply characterized. They will be discussed in next subsection.

With the same method, the in-plane microstrain of the thin epilayer can be evaluated. The eight widths of the four in-plane Bragg peaks of the thin epilayer, as presented in Figure 4.13, are summarized in Figure 4.30. The values of the in-plane widths are slightly different between q_l and q_t scans. By extrapolating the average widths along $q[110]x$ and $q[110]y$ axes, the domain sizes are estimated to be 3100Åalong $\langle 110\rangle_y$, and infinitely large along $\langle 110\rangle_x$. Here infinitely large should be understood as well beyond the resolution limit of our diffractometer. The microstrains of the thin epilayer are evaluated to be: $\left(\frac{\Delta a}{a}\right)_x = 0.21\%$ and $\left(\frac{\Delta a}{a}\right)_y = 0.14\%$. Once again, we see the in-plane asymmetry in the values of domain sizes and microstrains. The value of 3100Å for the average domain size along $\langle 110\rangle_x$ axis agrees with the theoretical domain size calculated with Equation 2.10 for the epilayer with 0.18% incommensurability.

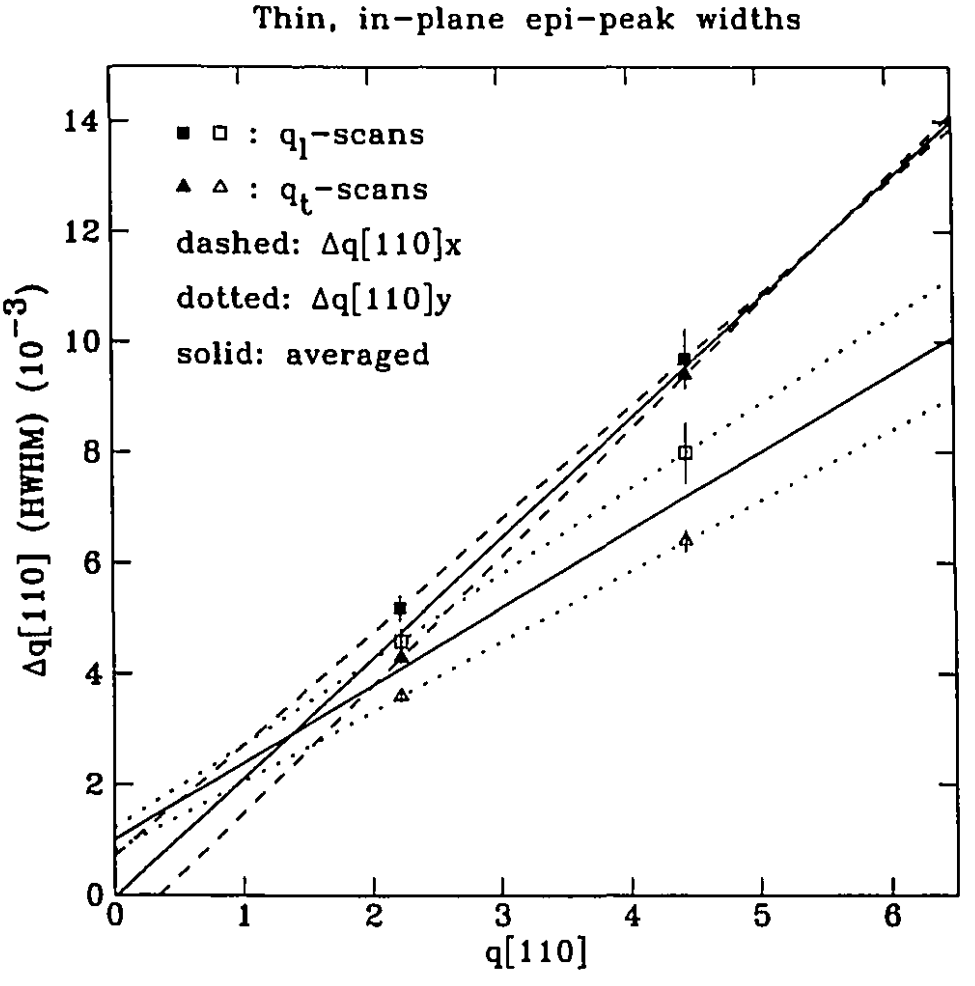

Figure 4.30: The in-plane epi-peak widths of the thin sample. The extrapolation of the peak widths along $\langle 110 \rangle_y$ gives the domain size, $p_y = 3100$ Å, and the microstrain, $\frac{\Delta a_y}{a_y} = 0.14\%$ The extrapolation of the peak widths along $\langle 110 \rangle_x$ gives the domain size, $p_x = \infty$, and the microstrain, $\frac{\Delta a_x}{a_x} = 0.21\%$.

4.3.2 Modulated Structures

As discussed in Section 2.2, the competition between the interfacial energy and the elastic strain energy in heteroepitaxy may result in a modulated structure. This modulated structure affects the shape of Bragg peaks in x-ray scattering measurements. In conventional x-ray structural characterization we usually fit the Bragg peaks to EWGL curves. Based on the parameters which define these curves, such as the positions, widths and intensities, we are able to extract structural information of the epilayer, such as the lattice constants, domain sizes and strains. However, important information of the microstructure of the epilayers is carried in the shape of Bragg peaks and has been ignored. In this subsection, we will discuss these effects.

Modulated structures can be investigated by studying the shape of Bragg peaks. But not all anomolous peak shapes correspond to modulated structures. Before we study the modulated structures, I would like to discuss what affects the shape of experimentally observed Bragg peaks in more detail.

An experimentally measured Bragg peak results from three parts: a) a coherent summation of scattering from an assembly of scatterers within a coherence region, and b) an incoherent summation of many such regions within the illuminated volume, and c) the convolution of this scattering with the resolution function of the diffractometer. The coherence regions and the illuminated volume are determined by the incident x-ray beam (ref: Section 3.1). The resolution function of the diffractometer and the x-ray source have been discussed in Chapter 3. Loosely speaking, the coherent summation corresponds to a structure whereas the incoherent summation corresponds to the distribution of possible structures. A normal Bragg peak may be fit to a sharp EWGL curve limited by the instrument resolution function, or a broad EWGL curve with width larger than the resolution limit. The former indicates a perfect order of scatterers. It is observed for the GaAs substrates we used and provides us a single structural parameter, the lattice constant. The latter

indicates some imperfect order in the scatterers, which can include modulated structure as well as many other types of disorder. We are not able to distinguish them without further information. This imperfection in ordering can be partially characterized by other structural parameters, such as the domain size and the strain (ref: Section 4.3.1). This strain is usually referred to as a microstrain in conventional characterization, because the overall strain, here referred to as the macrostrain, is related to the average position of the peak and not independent from the parameter determining the lattice constant. A Bragg peak which is not well characterized by a EWGL curve needs to be characterized by more parameters.

Given a detailled model of the structure of the material it is possible to calculate the expected x-ray diffraction profiles, it is not possible to infer uniquely what structures a given diffraction peak represents. In this section I will present some models to compare with the measured diffraction patterns. These models will hopefully give insight into possible structures in these materials and more importantly give some idea on what types of structures are not allowed.

Once we know the resolution function of the diffractometer and account for its effect in data analysis, the line shape analysis of Bragg peaks can be reduced to the two summations: coherent and incoherent. Some peaks will have their shape due to the incoherent summation from regions with different structures. This case can be analysed by fitting the data to a linear combination of two or three EWGL curves. We have discussed such fits to characterize the different regions of the epilayers (ref: Section 4.1 and 4.3). By studying many peaks, at low q and high q, in-plane and out-of-plane, we have convinced ourselves that the data interpretation makes sense and can not be explained better in other way. For example, we have fit both the (004) and (002) peaks of the thick epilayer as an incoherent summation of two peaks due to the top and bottom regions of the thick epilayer, and obtained a reasonable explanation for the positions, widths and intensities of these peaks (ref: Figure 4.3 and 4.4, and

Section 4.2.1). We have also fit the $(220)_x$ peak of the thin epilayer as two peaks due to the regions near the surface and near the epitaxial interface respectively and obtained direct information about the structural relaxation in strained epilayer (ref: Figure 4.18 and 4.20). We have, in fact, fit all our data with combinations of these line shapes, even in cases where it may not be appropriate. Not all peaks of a complex nature can be analysed in this simple way because the physical structure may not be simple. Modulated structures are an example and they would determine the coherent aspect of scattering summation. For example, the in-plane peaks of the thick epilayer are considerably different along the $(110)_x$ axis and the $(110)_y$ axis. In conventional characterization, the Bragg peaks along the $(110)_x$ axis suggest three lattice constants. Is this due to three regions of the epilayer? If so, why is there only one lattice constant along the $(110)_y$ axis? Another example is the (004) peak of the thin epilayer, which is asymmetrically distributed along the $(110)_x$ axis with respect to the (004) peak of the GaAs substrate. This peak has been fit as the sum of two EWGL curves, and suggests that there are two regions of the thin epilayer: one is aligned with the substrate, and the another one is tilted. Does this interpretation make sense? How are these regions distributed over the epilayer? If they arise from two different regions, by translating the sample to look at different regions of the epilayer, we could maybe expect to find, one spot on the sample which only has the peak which is aligned with the substrate, or the one which is misaligned. We have translated the sample, and taken data over a region much bigger than the illuminated spot of the incident x-ray beam and have observed the same pattern with the same relative peak intensities everywhere. These questions suggest that some other interpretation of the data is required. One such interpretation is given by modulated structures. We use these simplified models to try to extract some information about the nature of possible distortions. Although over simplified, they incorporate some of the essential features of how one might expect the dislocations which are created to relax the structure could effect the

scattering. Because x-ray scattering data can be usually reduced to one dimensional analysis and the perspective modulated structures seem uniaxial, we simplify our discuss of modulated structures to one dimensional problems.

Let us first consider a one dimensional atomic chain, as illustrated by Figure 4.31. For simplicity, all atoms in this chain are assumed to be the same type. A fundamental lattice is presented in (a). This lattice is characterized by two parameters: 1) the form factor of a single atom, f; 2) the lattice constant, a. One of the simplest modulations to this lattice is a sine wave modulation, as presented in (b) and (c). In (b), the displacement of each atom in this chain from its lattice point in the fundamental lattice has been plotted. For simplicity, we assume that the displacements of the atoms are confined to one dimension along the atomic chains. To characterize this atomic chain, as shown in (c), we need two more parameters: 1) the period of modulation, $N \cdot a$; 2) the magnitude of modulation, $e \cdot a$. The value of e corresponds to the microstrain in a conventional characterization (ref: Section 4.3.1). In the modulated chain shown in (b) and (c), the modulation parameters are: $N = 6$, and $e = 0.2$. If the continuity of modulated chain is disrupted between adjacent modulated periods, as shown in (d) and (e), we need more parameters to define this chain. The simplest case is that all the breaks occur at the same place with respect to a single modulated period and shift the modulated periods the same amount from every adjacent period. The average lattice constant changes to $a(1 + \epsilon)$, where ϵ corresponds to the macrostrain in a conventional characterization (ref: Section 4.3.1). If the modulation within a modulated period vanishs, *i.e.*, $e = 0$, we will have a lattice chain as shown in (f). As we have seen, the values of parameters a and ϵ of the atom chains from (a) to (f) are defined relatively and depend on the way one defines the average lattice constant of the chain.

Based on the above picture of an atomic chain, now let us consider two extreme cases of modulation: 1) the modulation exists within a domain (a single modulated

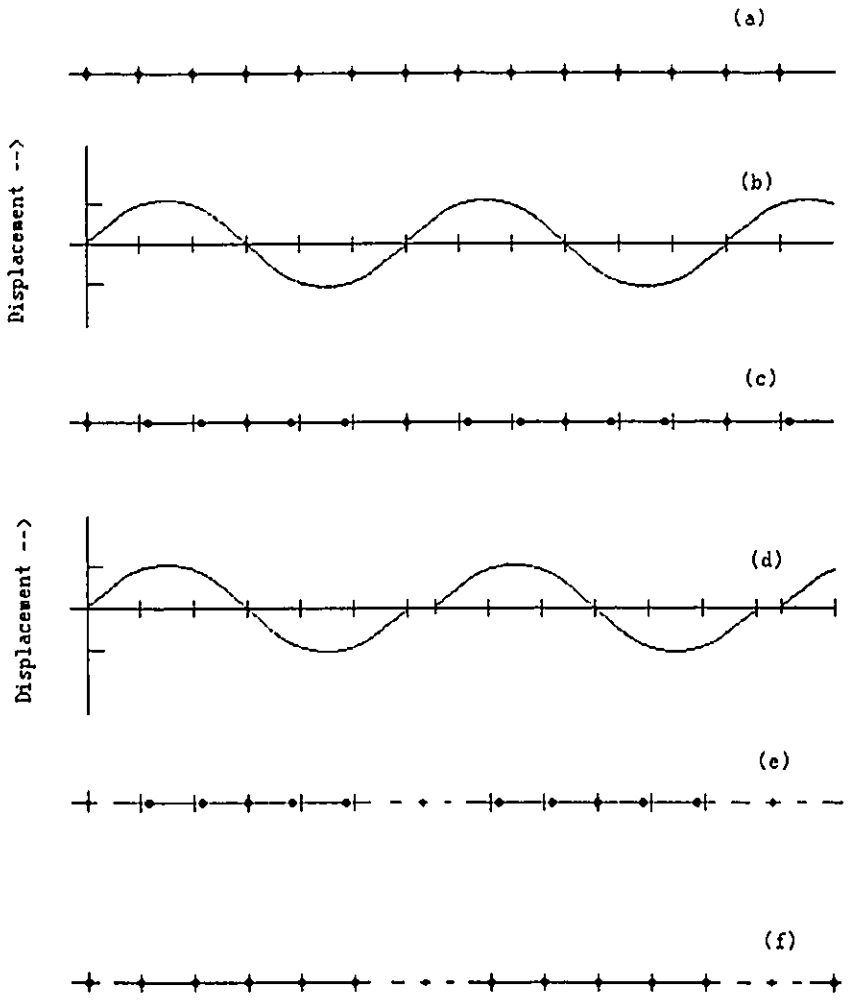

Figure 4.31: The one-dimensional modulated atomic chain. (a) Fundamental lattice. (b) Displacive modulation by plane wave. (c) Modulated lattice (commensurate). (d) A phase shift between modulated periods. (e) Modulated lattice (incommensurate). (f) Modulated lattice (discommensurate). The averaged lattice constants of (a) and (c) are same, and those of (e) and (f) are same. The change of lattice constants from (c) to (e) is accommodated by macrostrain.

period); 2) the modulation is between correlated domains. Instead of using a sine wave modulation with respect to the fundamental lattice, we use a model of a strain modulation with respect to a single domain, and write the position of atom j within a domain as

$$r_j = a_j j = a[1 + e \cdot cos(\frac{2\pi j}{N} + \alpha_i)]j, \tag{4.6}$$

The parameter, α_i, is the initial phase of the plane wave modulation with respect to the domain boundaries. A coherent summation of scattering from an atomic chain consisting of m such modulated domains with common phase shift h between any adjacent domains can be written as

$$\frac{d\sigma}{d\Omega} = C \left| \sum_{k=0}^{m-1} \sum_{j=0}^{N-1} exp[iqa_j \cdot (j + kN) + ihk] \right|^2, \tag{4.7}$$

where q is the momentum transfer of x-rays and C is a proportionality constant. The scattering factor of a single atom in this chain is assumed to be 1 and the Debye-Waller factor is ignored. The scattering patterns with varying parameters are illustrated in Figure 4.32. The parameter a used in the calculation of scattering patterns is 5.7123Å, which is the in-plane averaged lattice constant of the thick epilayer. The subfigure (a) and (b) show the second order and the fourth order scattering patterns of this atomic chain respectively, in which $e = 0.0014, N = 2000$, $\alpha_i = 0.0$, and $m = 1$. The two scattering patterns have approximately the same shape which is asymmetrically distributed around the unmodulated peaks, shown by the dashed curves in the figures (obtained by setting $e = 0$). These peaks produced by the unmodulated lattice are also called the main peaks. The width of the fourth order scattering is twice as broad as that of the second order scattering which illustrates the nature of x-ray analysis of microstrain discussed in last subsection. The distance between the first spike (or alternatively speckle) at the lower q side and the main peak is twice the distance between the main peak and the last spike at the higher q side. This pattern shifts and evolves with the value of initial

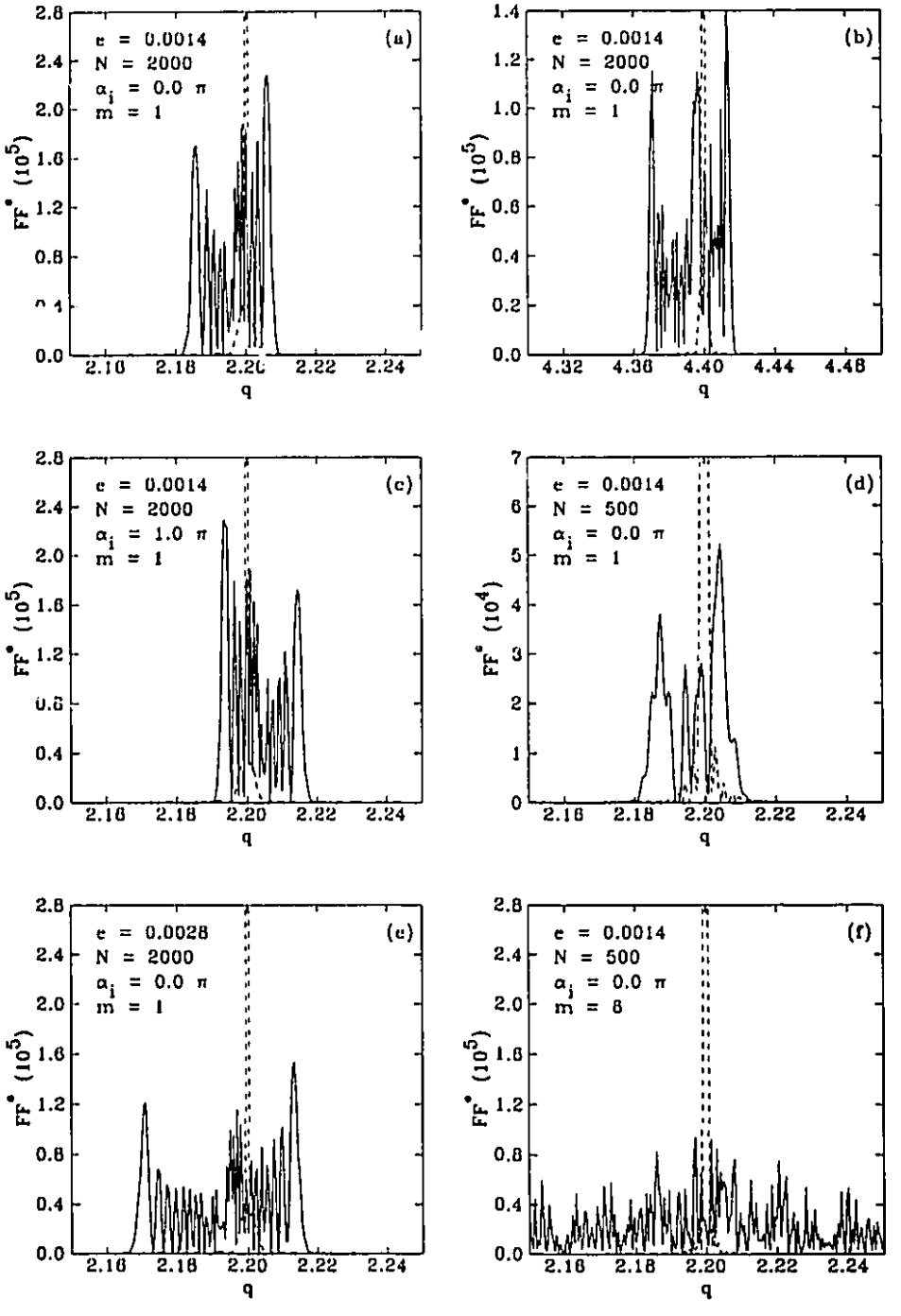

Figure 4.32: The scattering patterns of modulated atomic chains. The dashed curves are the scattering of the fundamental lattice. The definitions of the parameters shown in the figures are described in the text. F is the structure factor of this atom chain.

phase α_i. For example, when $\alpha_i = 1.0\pi$, the distribution of scattering is flipped with respect to the main peak, as shown in (c). The sharpness of the spikes is determined by N, which represents the range of the coherent summation. The spikes in (d) are less sharp than those in (a) because of the different value of N ($N = 500$ in (d) and $N = 2000$ in (a)). For the same order of scattering, the width of the scattering profile is proportional to the magnitude of modulation e, as shown in (e), in which $e = 0.0028$. In the case that the scattering of more than one modulated period, say 6 modulated periods as shown in (f), are coherently summed up, the scattering intensity becomes much more symmetrically distributed with respect to the main peak. Although the phase shift between the modulated periods changes the scattering pattern, it does not change the envelope of the scattering pattern and summing over many periods incoherently, one should possibly expect to get a Gaussian curve. In the special case when the parameter e is zero, as shown in Figure 4.31 (f), the effect of phase shift between domains can be directly measured [128,129].

With this model of structural modulation, we are now able to study the shape of Bragg peaks caused by such a modulated structure. As we have seen from the data, the in-plane peaks of the thick epilayer are significantly different along the two in-plane axes $\langle 110 \rangle_x$ and $\langle 110 \rangle_y$. These peaks fit quite well to EWGL curves along $\langle 110 \rangle_y$ axis, but not along $\langle 110 \rangle_x$ axis. The surface of the thick epilayer is also rougher along $\langle 110 \rangle_x$ axis ($\sigma_x = 27$Å, $\sigma_y = 18$Å). As you may have noticed that these two peaks, $(220)_x$ and $(440)_x$ of the thick epilayer, look very like the scattering patterns shown in Figure 4.32 (a) and (b) if the sharp spikes in the theoretical curves are smeared out by the dispersive effect of the x-ray source and incoherent summation of different domains. The constant C used in Equation 4.7 can be adjusted to account for the scattering factor of atomic sheets in the y-z plane of the epilayer. Figure 4.33 shows that the two scattering patterns of the thick epilayer along $\langle 110 \rangle_x$ fit quite well to the model with parameters: $a = 5.712(4), e =$

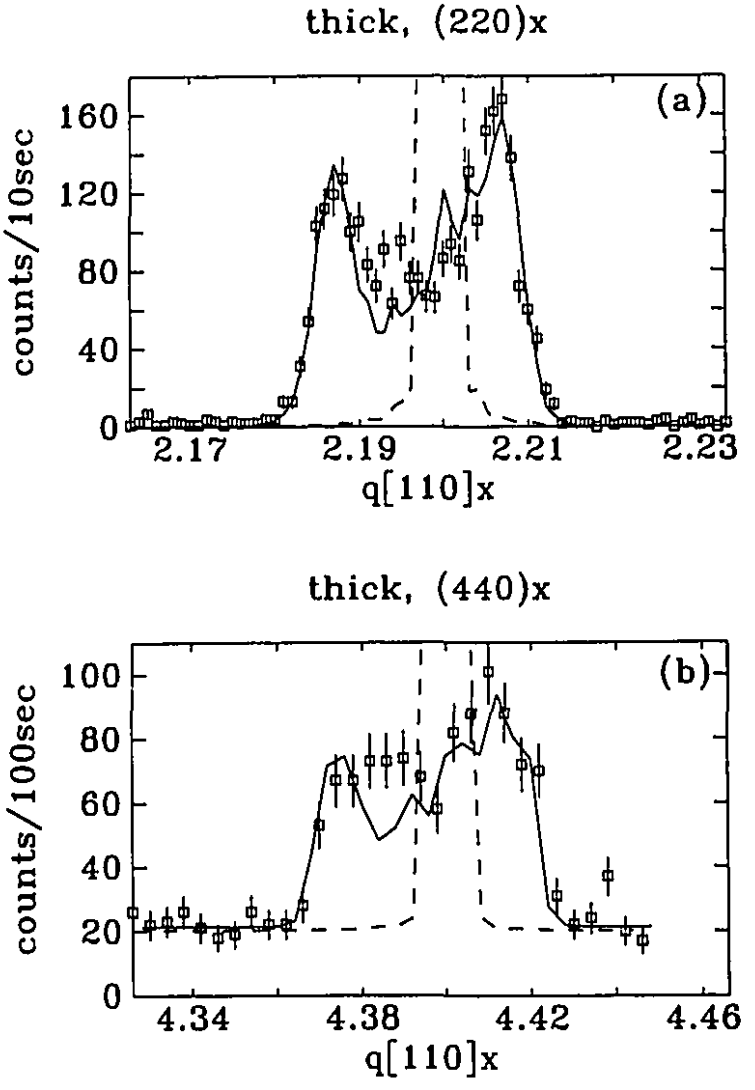

Figure 4.33: The fit of the $(220)_x$ and $(440)_x$ peaks of the thick epilayer to a strain modulation with plane wave. The dashed curves represents the $(220)_x$ and $(440)_x$ peaks of the fundamental lattice, which are plotted by setting $e = 0$, and keeping other parameters unchanged. For both $(220)_x$ and $(440)_x$ peaks, the modulation parameters are: $a = 5.712(1), e = 0.00142(3), N = 760$, $\alpha_i = 0.0$, and $m = 1$.

$0.00142(3), N = 760(8), \alpha_i = 0.0$, and $m = 1$. The parameter a agrees with the lattice constant evaluated along $(110)_y$ axis of the thick epilayer. The magnitude of modulation e is comparable to the microstrain evaluated by the out-of-plane data. The modulated range can be calculated by $\frac{a}{\sqrt{2}} \times N$ which equals to 3100Å. This range of modulation is about twice big as the average domain size estimated by the out-of-plane measurement.

The uniaxial modulation within domains is not shown by the shape of the in-plane Bragg peaks of the thin epilayer, which have been smeared out to Gaussian curves. These Bragg peaks have been characterized by the simple lineshapes in last subsection. The thin epilayer is strongly strained and the value of macrostrain is higher than that of microstrain (ref: Section 4.2.1). The presence of strong in-plane macrostrain in the thin epilayer implys the formation of correlation between domains and may also reduce the magnitude of the displacive modulation. This suggests the other extreme of modulation, as shown in Figure 4.32 (f), [84,128,129], *i.e.*, the correlated domain modulation. Unfortunately, we are not able to extract the information of correlated domains directly from the in-plane peaks of the thin epilayer because they are basically Gaussian curves.

Previous structural work on heteroepitaxy has concentrated on the identification and characterization of misfit dislocations at the epitaxial interfaces (ref: Section 2.4). For $Ga_{1-x}In_xAs$ epilayers grown on GaAs substrates, 60° dislocations with (111) slip planes are commonly observed [49] (ref: Section 2.4). The (111) plane is inclined to the (001) plane by $tan^{-1}(\sqrt{2}) = 54.7°$ for an undistorted lattice. In the case of inclined domain walls, if there is a phase shift between domains in-plane, there should also be a phase shift between domains out-of-plane. The relation between the in-plane phase shift and out-of-plane phase shift is determined by the Burgers vector of dislocation and the distortion of lattice. Focusing on the phase shift between domains, the modulated structure of the thin epilayer can be studied

with the following model.

This model is developed from the atom chain shown in Figure 4.31 (f) by including a three dimensional phase shift between domains. It is assumed that all domains have the same thickness, *i.e.*, the thickness of the epilayer. The sizes of domains along x axis are denoted as $p_0, p_1, p_2, \cdots p_n$ and that along y axis are all the same. It is also assumed that the structure of the epilayer along the two in-plane axes x and y can be independently treated to simplify the calculation. The correlations between domains are defined by integer multiplications of a unit vector $\mathbf{h} = [h_x, h_y, h_z]$. If h equals zero, the correlated domains reduce to a single crystal. The domain walls between the domains act as a diffraction grating with a large length scale and its scattering convolutes with the diffraction of the underlying lattice of atomic scale. This model can be furtherly simplified by assuming that all the atomic sheets are identical in y-z plane, and their scattering are defined as $f(\mathbf{r})$, which is equal to 1 on the atomic sheets and 0 otherwise. It is also assumed that the domain sizes are large enough so that finite size effects cause the intensity to change in transverse scans more rapidly, at constant perpendicular momentum transfer, than either dynamical effects or the angular dependence of the scattering factors. Because we are going to study the transverse scans of the (004) peak of the thin epilayer, the in-plane phase shift between domains has little effect on the shape of this peak. For simplicity, we assume $h_x = 0$ and $h_y = 0$. In the case of inclined domain walls, the in-plane phase shift can be calculated from the out-of-plane phase shift if the angle of inclination of the domain wall is known. With the approximations mentioned above, our problem is now reduced to the model of diffraction from stepped surfaces which has been developed by Pukite, Lent and Cohen [130,131].

A summary of their calculation follows. Let the separation between any two scatterers be denoted as (x, lh_z), where l is an integer. The probability of finding

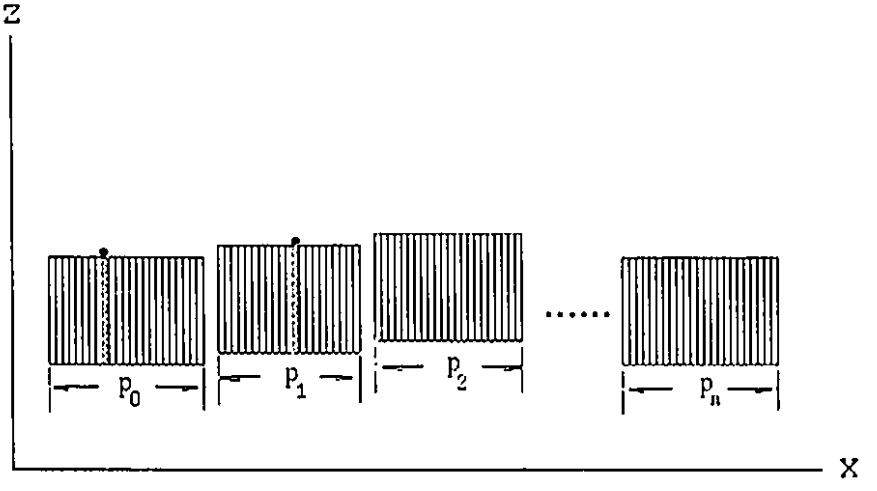

Figure 4.34: The correlated domains with both in-plane and out-of-plane phase shifts between domains.

these two scatterers at a given distance is the sum of the probabilities of all possible configurations of domains that separate these two scatterers. The probability of this configuration can be written as

$$P_0(p_0)P_1(p_1)\cdots P_{n-1}(p_{n-1})P_f(p_n)\Delta p_0\Delta p_1\Delta p_{n-1}\Delta p_n, \tag{4.8}$$

where the $P_j(p_j)$ with $j = 1, 2, \cdots, n-1$ are the probabilities per unit length of a domain size of p_j with out-of-plane phase shift jh_z. The function $P_0(p_0)$ is the probability per unit length that there is a scatterer at the origin that has a length p_0 before the first domain wall. The function $P_f(p_n)$ is the probability per unit length that there is a scatterer p_n away from the last domain wall. The middle $n-1$ $P_j(p_j)$ are identical and equal to $P(p_j)$ for the macroscopic lateral size of the epilayer. Equation 4.8 implicitly assumes that the domain sizes are statistically independent from one another. To find the pair correlation function, one must integrate over all possible configurations of domains. The out-of-plane phase shift distribution $H(l)$ and the domain size distribution $P(p)$ should be normalized according to:

$$1 = \sum_{l=-\infty}^{\infty} H(l), \qquad 1 = \int_{p=0}^{\infty} P(p)dp. \tag{4.9}$$

The scattering intensity of this model in x-z plane has been derived by Pukite *et al.* and can be eventually written as [131,132]

$$\frac{d\sigma}{d\Omega} = \frac{C}{\langle p\rangle q_x^2} Re\left\{\frac{[1-P(q_x)][1-H(q_z)]}{1-P(q_x)H(q_z)}\right\}, \tag{4.10}$$

where Re indicates the real part and $\langle p\rangle$ is the average domain size. $P(q_x)$ denotes the Fourier transform of the domain size distribution function $P(x)$, and $H(q_z)$ denotes the Fourier transform of the out-of-plane phase shift distribution function $H(l)$. One useful class of distributions of domain sizes can be described by gamma distributions, and are given by

$$P_M(x,\alpha) = [\alpha^M/\Gamma(M)]e^{-\alpha x}x^{M-1}, \tag{4.11}$$

where M is the disorder parameter, $\alpha = \frac{M}{<p>}$, and $\Gamma(M)$ is the gamma function. For $M = 1$, the gamma distribution is the exponential or geometric distribution of domain size. As M becomes large the gamma distribution approaches a normal distribution and in the extreme limit becomes a delta function centered at $x = \langle x \rangle$. For these functions the shape of Bragg peaks will vary between the extremes of $M = 1$ and $M = \infty$. Similar to the length distribution function which has been applied to the stepped surfaces [131,132], we assume that the domain size distribution is a linear combination of the first and the second order of Γ distributions, *i.e.*,

$$P(x) = AP_1(x,\alpha) + (1-A)P_2(x,\beta), \tag{4.12}$$

where α, β and A are adjustable parameters to define this distribution. Consistent with our expectations of possible out of plane phase shifts we assume the out-of-plane displacements of adjacent domains only have two choices, h_z or $-h_z$. Then $H(q_z)$ can be written as

$$H(q_z) = Be^{-ih_zq_z} + (1-B)e^{ih_zq_z}, \tag{4.13}$$

where B denotes the relative probability of each type. Equation 4.10 with Equations 4.12 and 4.13 can be used to fit the transverse scan of the (004) peak of the thin epilayer along $\langle 110 \rangle_x$ axis. We have used the same model to fit the transverse scan of the (004) peak of the thin epilayer along $\langle 110 \rangle_y$ axis, by simply substituting x by y in all equations. The in-plane scattering of the (004) peak of the thin epilayer is proportional to the product of the scattering cross sections calculated by the one dimensional model, as indicated by Equation 4.10, along $\langle 110 \rangle_x$ and $\langle 110 \rangle_y$ axes respectively.

The fit of the (004) peak of the thin epilayer to the model mentioned above is shown in Figure 4.35. The value of q_z, the out-of-plane x-ray momentum transfer, is 4.3305Å^{-1} as experimental measured. For both transverse scans along $q[110]x$ and $q[110]y$, the domain size distributions are fit by the same parameters, $\alpha = 0.0027(3)$,

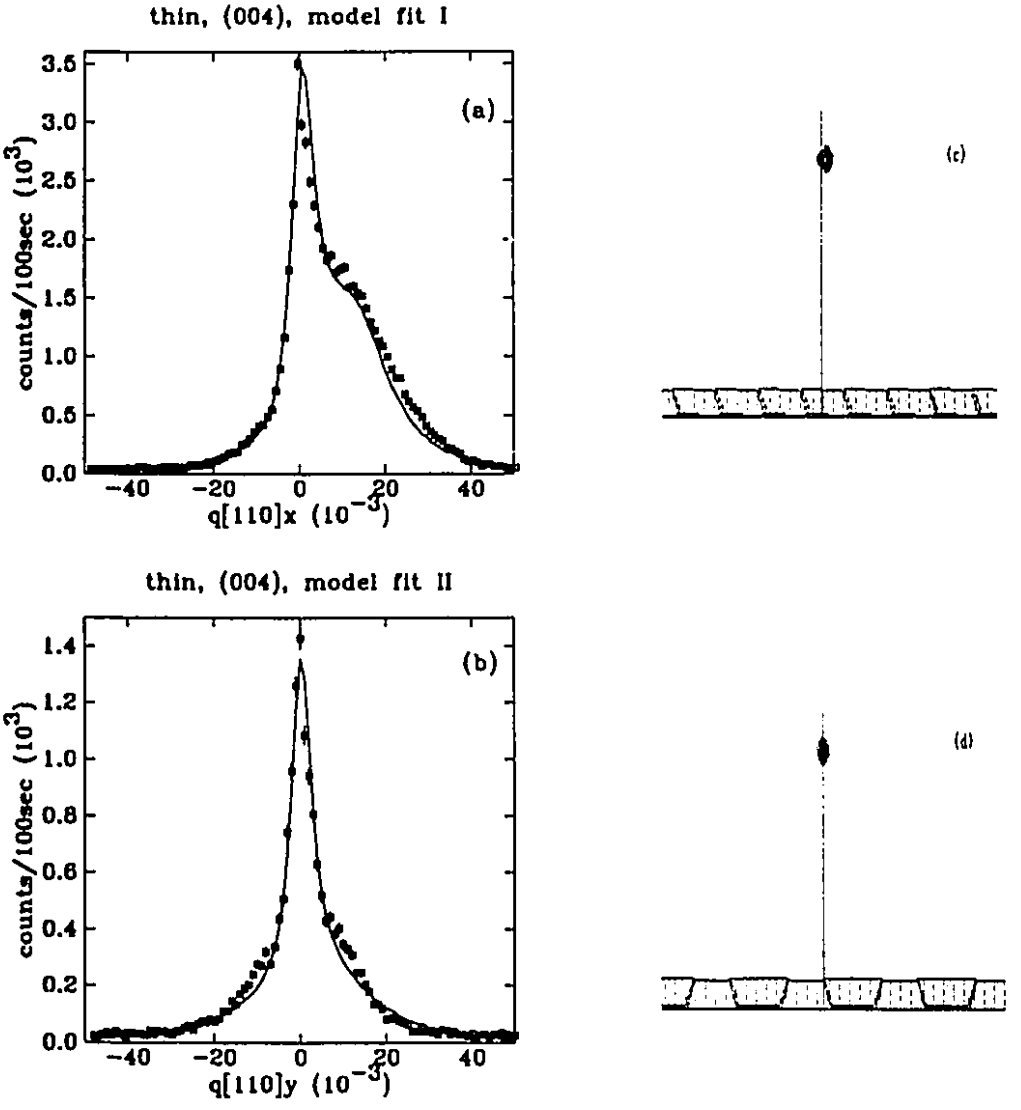

Figure 4.35: The interference of domains of the thin epilayer as seen at the (004) epi-peak. (a) The data and fitting curve of (004) epi-peak in x-z plane with $h_z = 1.088$ and $B = 0.9$. (c) the suggested domain correlation in x-z plane. (b) The data and fitting curve of (004) epi-peak in y-z plane with $h_z = 1.087$Åand $B = 0.59$. (d) the suggested domain correlation in y-z plane.

$\beta = 0.022(2)$ and $A = 0.204(1)$. The out-of-plane displacement distribution for both curves are fit by $h_z = 1.087(3)$Å, but with $B = 0.90(5)$ for the scan along $\langle 110 \rangle_x$ axis shown in (a), and $B = 0.59(2)$ for the scan along $\langle 110 \rangle_y$ axis shown in (b). The nearly unity value of the parameter B suggests the nearly monotonic phase shift up between adjacent domains along the $\langle 110 \rangle_x$ direction, as shown in Figure 4.35 (c). All the domain walls are nearly of the same type. The value of the parameter B being nearly one half in the other direction suggests the nearly equal probability of phase shifts up and phase shifts down between adjacent domains, as shown in Figure 4.35 (d). The neighbouring domain walls are nearly of opposite sign. This type of asymmetry has been previously suggested by the data of Abrahams *et al.* and Kavanagh *et al.* [105,49] (ref: Section 2.4). Abrahams *et al.* observed that the spatial arrangement of the two sets of orthogonal 60° dislocations tended to be uniformly distributed only along one $\langle 110 \rangle$ direction, while in the other $\langle 110 \rangle$ direction there was a marked tendency for periodic banding of the dislocations. Kavanagh *et al.* observed that the 60° α dislocations formed first in one $\langle 110 \rangle$ direction at the interface of thin epilayers. We guess that the 60° dislocations of like sign may be more easily generated at the interface than that of opposite sign, or that the dislocations of opposite sign may be overlooked under plain-view of TEM.

The domain size distributions of the thin epilayer are the same along both axes and illustrated by Figure 4.36. The average domain size is evaluated to be 460Å and the preferred domain size is evaluated to be 190Å. These domain sizes are much smaller than that evaluated in conventional characterization (ref: Section 4.3.1), but the domains in this model are correlated. The magnitude of the out-of-plane phase shift between adjacent domains is estimated by $2\pi\frac{h_z}{a_z} = 0.37\pi$. The disagreement on domain size evaluation between the conventional characterization and shape analysis suggests a limitation of Equation 4.5, which has been derived based on the approximation that all domains are randomly distributed in

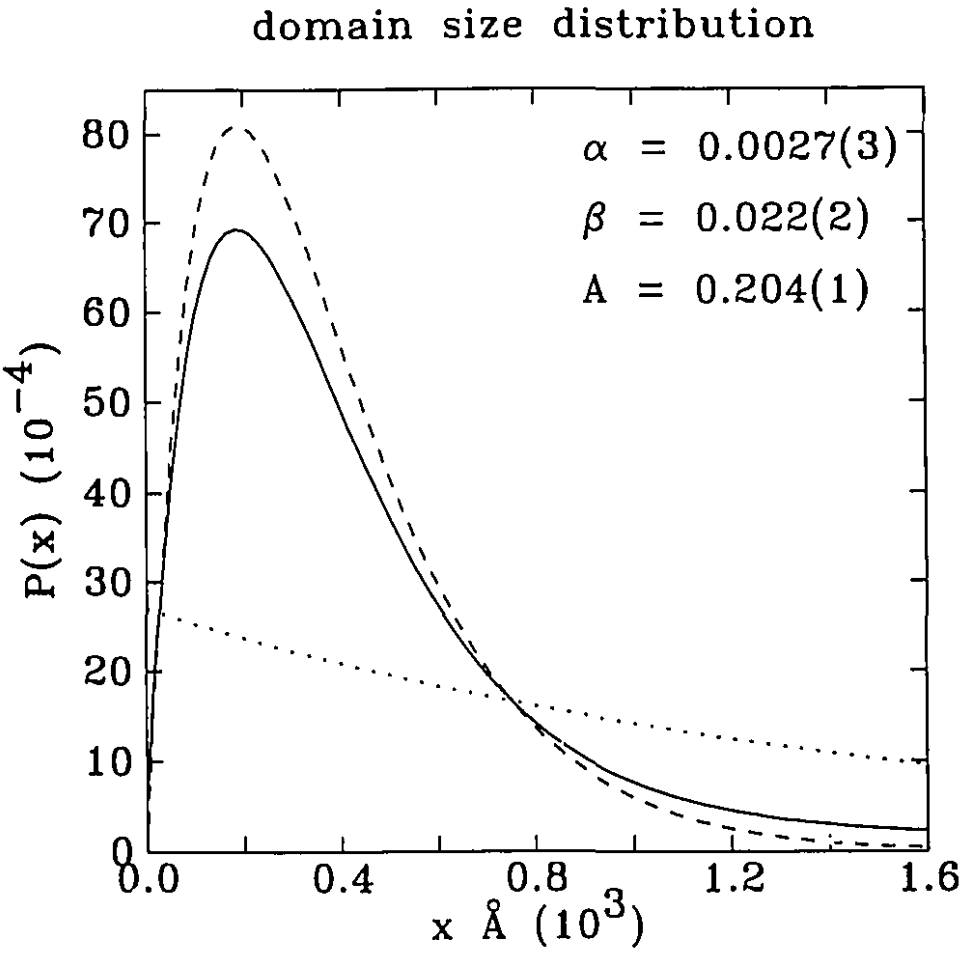

Figure 4.36: Domain size distribution of the thin epilayer. The solid line the domain size distribution funcion $P(x)$ as indicated by Equation 4.13. The dotted line is the first order gamma distribution, $P_1(x,\alpha)$, and the dashed line is the second order gamma distribution, $P_2(x,\beta)$. The parameters, α, β and A, are obtained by fitting the experimental data. This distribution gives a preferred domain size 190Å, and an average domain size 460Å.

orientations [21,23].

In this subsection, we have investigated the modulated structures of the epilayers by studying the shape of Bragg peaks. We have fit the in-plane peaks of the thick epilayer along the $(110)_x$ axis by using the model of strain modulation within domains. We have also fit the transverse scans of the out-of-plane peak of the thin epilayer by using the model of correlated domain modulation. These two models can be considered as the two extremes of modulated structures. We have extracted some information from these models, for example, the magnitude and range of modulated strains in the thick epilayer, the phase shift between adjacent domains in the thin epilayer. We may also have noticed that the modulation is basically uniaxial for both samples but different near the interface from near the surface.

4.3.3 Asymmetry

Our data suggest a transition region of modulated structures between the substrate and the surface of the epilayer in heteroepitaxy. This transition region may be asymmetric. The asymmetric properties of 60° dislocations appearing at the epitaxial interface of III-V compounds have been previously discussed by Abrahams *et al.* in terms of the chemical non-equivalence of α and β types of dislocations [105] (ref: Section 2.4). Here, mainly for a pedagogical point of view, I'd like to mimic the process of layer by layer growth and to show you how the asymmetrically distributed chemical bonds may result in asymmetric structure.

Figure 4.37 (a) shows a model of III-V compound, the atoms and the chemical bonds. Five (001) layers of atoms are shown in this figure. The dark circles represent the V atoms, and the grey circles represent the III atoms. The layers of III atoms and V atoms are alternately arranged along the (001) direction. The tetrahedral bonds of each atom are also clearly shown in this figure. For a III atom, the two bonds below the layer of III atoms lie in one plane which contains the (001) axis

and one of the ⟨110⟩ axes, while the two bonds above the layer lie in an orthogonal plane which contains the ⟨001⟩ axis and the other ⟨110⟩ axis. The crystallographic properties of this compound can be found in literatures [105,85].

With this structure for the III-V compounds, we can discuss the effect of the chemical bonding which may be responsible for the asymmetric structure of the $Ga_{1-x}In_xAs$ epilayers grown on the GaAs (001) substrates. Figure 4.37 (b) shows the first layer of As atoms grown on the GaAs (001) substrate (the substrate is not shown). In principle, this layer of growth is homoepitaxial. The second atomic layer (*i.e.*, the first complete layer of $Ga_{1-x}In_x$) along with the first layer of As atoms and their chemical bonds are shown in Figure 4.37 (c). The projections of the chemical bonds on the (001) plane is along one direction. This direction may be defined as ⟨110⟩ axis. If the indium composition x is not zero, this layer of $Ga_{1-x}In_x$ atoms is incommensurate with the substrate and will be modulated due to the competition between the interfacial energy and the elastic strain energy (ref: Section 2.1). This modulation is asymmetric because the chemical bonding is asymmetric (except the case of pseudomorphism). The interfacial energy should have different effects along the ⟨110⟩ axis than along the orthogonal one, say $\langle 1\bar{1}0\rangle$ axis (ref: Equation 2.3). The second layer of As atoms is now grown, as shown in Figure 4.37 (d). The previous asymmetry may be recovered or partially recovered by the newly grown layer of As atoms, because they bond the $Ga_{1-x}In_xAs$ atoms in the orthogonal direction, *i.e.*, $\langle 1\bar{1}0\rangle$ axis. The layers of $Ga_{1-x}In_x$ atoms and As atoms are alternately added, as shown in Figure 4.37 (e) and (f), and chemical bonds are alternately added and projected along the $\langle 110\rangle_x$ and $\langle 110\rangle_y$ axes. The incommensurate modulation is different along the $\langle 110\rangle_x$ direction from the $\langle 110\rangle_y$ direction due to the strength of bonding, and it affects the structure and relaxation of the epilayer. If the growth proceeds by adding two atomic layers, *i.e.*, one layer of $Ga_{1-x}In_xAs$, each time, the chemical bonds at the growth front are always along one of the ⟨110⟩ axes. The

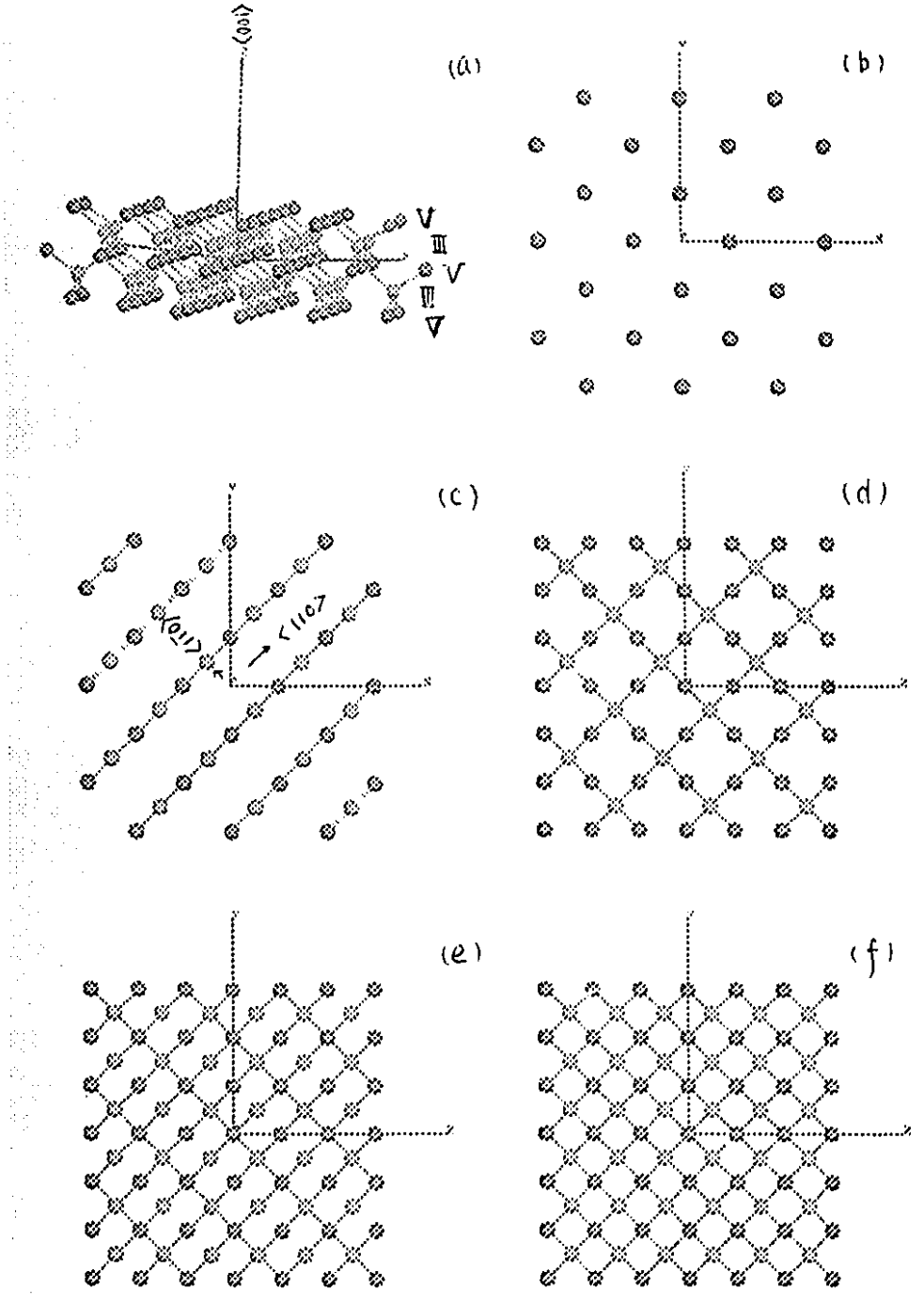

Figure 4.37: The asymmetric (001) epitaxial interface of III-V compounds. (a) tetrahedral bonded compound. (b) first layer of V atoms (dark) grown. (The substrate with III atoms on the surface is not shown.) (c) first layer of III atoms (grey) grown. (d) second layer of V atoms grown. (e) second layer of III atoms grown. (f) third layer of V atoms grown.

asymmetric properties are intrinsic to heteroepitaxy of $Ga_{1-x}In_xAs$ on GaAs (001) substrates.

Based on the above picture, we may think about the possibility of uniquely defining the ⟨110⟩ axis of III-V epitaxial interfaces. This will be very helpful for us to study the microstructure of the transition region in detail. It seems that the $(110)_x$ axis for both the thin and the thick samples can be considered as the ⟨110⟩ axis in terms of their modulated structures. Even though the modulated structures in the thin epilayer and the thick epilayer may be quite different, as we have studied in last subsection, they reflect some aspects of the feature of the competeting interaction at the epitaxial interface. In principle, if the bonding is strong along certain axis, say ⟨110⟩ axis, the interfacial energy has more chance to win, and the substrate will have more effect on the structure of the epilayer along this axis. But we still can not weeded out the alternate interpretation of our data by rotating one of the samples by 90°. For example, we still do not fully understand the nature of the misalignment of the in-plane $(220)_y$ and $(440)_y$ peaks of the thin epilayer with that of the substrate. We also not really have a good explanation for the misalignment of the (004) and (002) peaks of the thick epilayer with that of the substrate, except interpreting it as a tilt of the crytalline plane. The structure of epilayers is complicated. It changes from the interface to the surface of the epilayer along the direction of growth. It also changes along different in-plane axis. We need to study more samples and more systems to obtain a better understanding of heteroepitaxy. The scattering patterns are complicated. We need to develop more sophisticated models to make a full use of our data.

Chapter 5

Conclusions

This thesis has presented the techniques and results of our high resolution x-ray structural studies of heteroepitaxy. The specific system we have investigated is $Ga_{1-x}In_xAs$ grown on GaAs (001) substrates by MOCVD. The apparatus we have used is a triple-axis four-circle diffractometer with a conventional 2.2 kW Cu-target x-ray tube source and Ge (111) resolution.

It may have been thought that heteroepitaxy could be considered as a simple system because it is merely a combination of two crystals. Much research has been previously carried out to identify and characterize the lattice distortions and dislocations caused by the substrate crystal on the epitaxial crystal. This has indicated that heteroepitaxy should be considered as a complex system resulting from competeting interactions and kinetic effects during growth. Systems with competeting interactions have been extensively studied for the last decade in terms of commensurate-incommensurate phase transitions. Heteroepitaxy can be considered as a cross-over of the two extremes with both three dimensional and two dimensional structural features presented on various length scales. X-rays have been celebrated as powerful probes for both three and two dimensional structures and provide an ideal tool for studying heteroepitaxy.

Recent measurements have shown that it is possible to study the structure of a single atomic layer with x-rays using synchrotrons [31, 28, 33]. Although this would be impossible with conventional sources, conventional sources are suitable for studies of heteroepitaxy. This is because although the in-plane structure of the epilayer evolves along the direction of growth, we need not study the structural evolution layer by layer, but region by region. A region usually consists of many atomic layers of the same in-plane structural features, and these produce signals much stronger than that of one or two atomic layers.

Often high resolution work has tried to isolate the $K_{\alpha 1}$ line with slits and this considerably reduces the intensity of the incident beam. X-rays of different wavelengths do not interfere with each other, and produce their own scattering patterns from the sample. These scattering patterns are essentially the same in shape and only differ in intensities and positions which are determined by the incident beam profile of the x-rays and the configuration of the experimental set-up. We have used the whole beam profile monochromated by Ge (111) reflections to increase the incident beam intensity. This beam profile consists of three Lorentzians of $K_{\alpha 1}$, $K_{\alpha 2}$ and $K_{\alpha 3}$ lines. The momentum transfer of x-rays is defined in term of wavelength of $K_{\alpha 1}$ line, and scattering patterns of $K_{\alpha 2}$ and $K_{\alpha 3}$ lines are fit in the same way as that of $K_{\alpha 1}$ line by accounting for the intensity ratios and position displacements in q-space. In addition, the techniques to measure the surface miscut of samples by combining the normal Bragg scattering and specular reflection, and to handle the footprint correction under glancing incidence scattering in data treatment have proved to be very useful. Since our work is based on a conventional x-ray source, the techniques we have practised and developed can be used in any laboratory to characterize and study growth process and sample quality.

Our studies have concentrated on two samples: a 500Å $Ga_{0.81}In_{0.19}As$ epilayer and a 40000Å $Ga_{0.84}In_{0.16}As$ epilayer, both grown on GaAs (001) substrates

by MOCVD. According to Vegard's law, these two epilayers are lattice-mismatched to the GaAs substrates by 1.36% and 1.14% respectively. The miscuts on the substrate surfaces are 2° for the thin epilayer, and 0.2° for the thick epilayer, which have been accurately measured in our experiment. The In composition in the thick epilayer is evaluated to be 15.8% by averaging the measured lattice parameters, which agrees with the value evaluated by Prof. A. Roth, who prepared the samples. The electron density of the thin epilayer is evaluated to be 1.1% higher than that of $Ga_{0.81}In_{0.19}As$ by the reflectivity measurement, which agrees with the evaluation of average unit cell volume change resulted from strains. Our in-plane data show that the thin epilayer has been strongly strained to match the substrate but retains a 0.18% incommensurability near the interface up to 400Å and is partially relaxed to 0.45% near the surface. The out-of-plane lattice expansion of the thin epilayer is measured to be 1.28%. According to the directly measured values of the in-plane strain and out-of-plane strain of the thin epilayer (taking the Vegard's value as a reference), the Poisson's ratio is evaluated to be 0.36 near the epitaxial interface. This value is about 12% larger than that conventionally used. We find that the thick epilayer can be separated into two regions (bottom and top) according to in-plane microstrains. The bottom region is about 13000Å thick near the epitaxial interface, and the in-plane microstrain is 0.15%. The in-plane microstrain of the top region is 0.10%. Our data suggest a transition region between the substrate and the surface of the epilayer. This region accommodates the structural relaxation in heteroepitaxy in terms of both macrostrain and microstrain evolution.

We have gained some insight into the microstructure of the transition region by studying the shape of the Bragg peaks. We have fit the transverse scans of the (004) peak of the thin epilayer along both $(110)_x$ and $(110)_y$ axes to a model of correlated domain modulation. Based on this model, the average domain size is evaluated to be 460Å, and the preferred domain size is evaluated to be 190Å. The domain size

distributions are same, but the domain shapes may be different along the two in-plane directions. The probabilities of phase shift up out-of-plane between adjacent domains are 0.9 along the $\langle 110 \rangle_x$ direction and 0.59 along the $\langle 110 \rangle_y$ direction. These out-of-plane phase shifts can be understood as a result of inclined domain walls and imply 60° partial dislocations as frequently observed in thin strained epilayers. The like sign domain walls along $\langle 110 \rangle_x$ direction trend to be uniformly distributed and produce a better dislocation grating. The opposite sign domain walls along $\langle 110 \rangle_y$ direction have more chance to react and generate new domain walls and relax the lattice. We find that the domain sizes of the thick epilayer keep unchanged from the bottom region to the top region where the in-plane microstrain changes dramatically. This implys that the domain walls of the thick epilayer, at least in the top region, are perpendicular to the epitaxial interface. The full edge dislocations can be generated by interacting opposite 60° partial dislocations and are frequently observed in thick epilayers [53, 50]. This mechanism of dislocation generation gives a natural way to explain the asymmetries in both the thin and thick films and also explains how one evolves into the other under growth.

Our data suggests a complicated transition region exists in the epilayer and it extends to the surface of the even the four micron sample. It would seem that the conventional concept of a critical thickness, which is primarily based on theoretical models of epitaxy, leads to a too simplified view of the structural relaxation of a strained epilayer. To be fair, most models predicting critical thicknesses are based on thermodynamic equilibrium models. It is highly possible that the growth processes used to make the samples have resulted in non-equilibrium structures. In any extent more work remains to be done both from a theory and from an experimental point of view.

In this thesis, we have presented the techniques and results of our x-ray structural studies of heteroepitaxy. We proved the power of x-ray scattering and gained

some insight into the fundamental issue. In order to fully understand heteroepitaxy, we need to study more samples and more systems. We also need to improve the models to make a complete use of our scattering patterns.

Bibliography

[1] H. Freyhardt, editor. *Crystals, Growth, Properties, and Aplications.* Springer-Verlag, Berlin-Heidelberg-N.Y., 1980.

[2] L. Esaki. *Molecular Beam Epitaxy and Heterosiructures, edited by L. Chang and K. Ploog*, chapter 1, page 1. Martinus Nijhoff, Netherlands, 1985.

[3] O. Hipolito, G. Marques, and A. Fazzio, editors. *Current Topics on Semiconductor Physics.* World Scientific, 1987.

[4] M. Pepper and D. Wharam, Physics World **1**, 29 (1988).

[5] F. Capasso, Physics Today. 43(2), 45 (1990).

[6] E. Bauer, B. Dodson, D. Ehrlich, L. Feldman, C. Flynn, M. Geis, J. Harbison, R. Matyi, P. Peercy, P. Petroff, J. Phillips, G. Stringfellow, and A. Zangwill, Journal of Materials Research 5(4), 852 (1990).

[7] J. Matthews, editor. *Epitaxial Growth, Part B.* Academic Press, Inc., 1975.

[8] M. van Hove, W. Weinberg, and C.-M. Chen. *Low Energy Electron Diffraction.* Springer, Berlin, 1986.

[9] J. Cowley. *Reflection High Energy Electron Diffraction and Reflection Electron Imaging of Surfaces, edited by P.K. Larsen and P.J. Dobson*, page 261. Plenum Press, New York, 1988.

[10] D. William. *Practical Electron Microscopy in Materials Science.* Verlag Chemie International, Weinheim, 1984.

[11] L. Fiermans, J. Vennik, and W. Dekeyser, editors. *Electron and Ion Spectroscopy of Solids.* Plenum Press, New York, 1978.

[12] A. Howie and U. Valdie, editors. *Surface and Interface Characterization by Electron and Optical Methods.* Plenum Press, New York, 1988.

[13] I. Robinson, R. Tung, and R. Feidenhans'l, Phys. Rev. B **38**, 3632 (1988).

[14] E. Specht, G. Ice, C. Peters, C.J.Sparks, N. Lucas, X. Zhu, R. Moret, and H. Morkoc, MRS preceedings, Advances in Surface and Thin Film Diffraction **208** (1990).

[15] F. Walker, E. Specht, and R. Mckee, Phys. Rev. Letters **67(20)**, 2818 (1991).

[16] H. Hong, R. Aburano, D. Lin, H. Chen, T. Chiang, P. Zschack, and E. Specht, Physical Review Letters **68(4)**, 507 (1992).

[17] L. Bragg, Proc. Camb. Phil. Soc. **17**, 43 (1912).

[18] A. Compton and S. Allison. *X-rays in Theory and Experiment.* D. van Nostrand, New York, 1935.

[19] H. Bragg and L. Bragg. *The crystalline state.* G. Bell, London, 1949.

[20] U. Arndt and B. Willis. *Single Crystal Diffractometry.* Cambridge, At the University Press, London, 1966.

[21] B. Cullity. *Elemental of X-ray Diffraction.* Addison Wesley, Reading, Mass., 2 edition, 1975.

[22] R. James. *The Optical Principles of the Diffraction of X-rays.* Ox Bow, Connecticut, 1982.

[23] B. Warren. *X-ray diffraction.* Dover, New York, 1990.

[24] M. Krivoglaz. *Theory of X-ray and Thermal-Neutron Scattering by Real Crystals.* Plenum Press, New York, 1969.

[25] W. Marra, P. Eisenberger, and A. Cho, J. Appl. Phys. **50**, 6927 (1979).

[26] P. Eisenberger and W. Marra, Phys. Rev. Letters **46**, 1081 (1981).

[27] R. Birgeneau, P. Heiney, and J. Pelz, Physica (Utrecht) **110B**(109), 1785 (1982).

[28] I. Robinson, Phys. Rev. Letters **50**, 1145 (1983).

[29] M. Sutton, S. Mochrie, and R. Birgeneau, Phys. Rev. Letters **51**, 407 (1983).

[30] P. Pershan and J. Als-Nielsen, Phys. Rev. Letters **52**, 759 (1984).

[31] S. Mochrie, M. Sutton, R. Birgeneau, D. Moncton, and P. Horn, Phys. Rev. **B30**, 263 (1984).

[32] B. Ocko, A. Braslau, P. Pershan, J. Als-Nielsen, and M. Deutsch, Phys. Rev. Letters **57**, 94 (1986).

[33] E. Specht, A. Mak, C. Peters, M. Sutton, R. Birgeneau, K. D'Amico, D. Moncton, S. Nagler, and P. Horn, Zeitschrit fur Physik B **69**, 347 (1987).

[34] P. Fuoss, K. Liang, and P. Eisenberger. *Synchrotron Radiation Research: Advances in Surface and Low-Dimensional Science, edited by Z. Bachrach.* Plenum, New York, 1986.

[35] D. Gibbs, B. Ocko, D. Zehner, and S. Mochrie, Phys. Rev. B **38**, 7303 (1988).

[36] B. Ocko and S. Mochrie, Phys. Rev. B **38**, 7378 (1988).

[37] S. Sinha, E. Sirota, S. Garoff, and H. Stanley, Physical Review **38**, 2297 (1988).

[38] R. Feidenhans'l, Surface Science Reports **10**, 105 (1989).

[39] B. Baliga and S. Ghandhi, J. Electrochem. Soc. **122(5)**, 683 (1975).

[40] H. Nagai, J. Appl. Phys. **45(9)**, 3789 (1974).

[41] Y. Kawamura and H. Okamoto, J. Appl. Phys. **50(6)**, 4457 (1979).

[42] P. Gourley, I. Fritz, and L. Dawson, Appl. Phys. Lett. **52(5)**, 377 (1988).

[43] I. Fritz, P. Gourley, and L. Dawson, Appl. Phys. Lett. **51(13)**, 1004 (1987).

[44] T. Andersson, Z. Chen, V. Kulakovskii, A. Uddin, and J. Vallin, Appl. Phys. Lett. **51(10)**, 752 (1987).

[45] C. Herbeaux, J. D. Persio, and A. Lefebvre, Appl. Phys. Lett. **54(11)**, 1004 (1989).

[46] P. Berger, K. Chang, P. Bhattachaya, J. Singh, and K. Bajaj, Appl. Phys. Lett. **53(8)**, 684 (1988).

[47] P. Orders and B. Usher, Appl. Phys. Lett. **50(15)**, 980 (1987).

[48] S.-L. Weng, J. Appl. Phys. **66(5)**, 2217 (1989).

[49] K. Kavanagh, M. Capano, L. Hobbs, J. Barbour, P. Maree, W. Schaff, J. Mayer, D. Pettit, J. Woodall, J. Stroscio, and R. Feenstra, J. Appl. Phys. **64(10)**, 4843 (1988).

[50] K. Chang, P. Bhattacharya, and R. Gibala, J. Appl. Phys. **66(7)**, 2993 (1989).

[51] A. Drigo, A. Aydinli, A. Carnera, F. Genova, C. Rigo, C. Ferrari, P. Franzosi, and G. Salviati, J. Appl. Phys. **66(5)**, 1975 (1989).

[52] G. Whaley and P. I. Cohen, Appl. Phys. Lett. **57(2)**, 144 (1990).

[53] R. Dixon and P. Goodhew, J. Appl. Phys. **68(7)**, 3163 (1990).

[54] G. Price, Physical Review Letters **38**, 2297 (1988).

[55] Q. Sun, C. Lacelle, D. Morris, M. Buchanan, P. Marshall, P. Chow-chong, and A. Roth, Appl. Phys. Lett. **59(11)**, 1359 (1991).

[56] D. Hetherington, P. Hinrichsen, R. Masut, D. Morris, and A. Roth, Can. J. Phys. **69**, 378 (1991).

[57] Z. Hang, D. Yan, F. Pollak, G. Pettit, and J. Woodall, Phys. Rev. B **44(19)**, 10546 (1991).

[58] J. Matthews, S. Mader, and T. Light, J. Appl. Phys. **41**, 3800 (1970).

[59] M. Frankenheim, Ann. Phys. **37**, 516 (1836).

[60] L. Royer, Bull. Soc. Fr. Mineral. Crist **51**, 7 (1928).

[61] S. Sakai and Y. Ohashi, MRS preceedings, Interface Dynamics and Growth **237** (1991).

[62] J. Arthur and J. LePore, J. Vac. Sci. Technol. **6**, 545 (1969).

[63] K. Ploog. *Crystals, Growth, Properties, and Aplications, edited by H. Freyhardt*, chapter 3. Springer-Verlag, Berlin-Heidelberg-N.Y., 1980.

[64] G. Stringfellow. *Organometallic Vapor-Phase Epitaxy: Theory and Practice*, chapter 1. Academic Press, Inc., 1989.

[65] J. Duchemin, S. Hersee, M. Razeghi, and M. Poisson. *Molecular Beam Epitaxy and Heterostructures, edited by L. Chang and K. Ploog*, chapter 18, page 677. Martinus Nijhoff, Netherlands, 1985.

[66] P. Dapkus, Ann. Rev. Mater. Sci **12**, 243 (1982).

[67] T. Barker, J. Chem. Soc. Trans. **89**, 1120 (1906).

[68] D. Pashley. *Epitaxial Growth: edited by J.W. Matthews*, chapter 1, page 1. Academic Press, Inc., 1975.

[69] F. Frank and J. van der Merwe, Proc. Roy. Soc. (London) **A198**, 216 (1949).

[70] G. Honjo and K. Yagi. *Current Topics in Materials Science: edited by E. Kaldis*, page 195. North Holland. Amsterdam, 1975.

[71] S. Jain, J. Willis, and R. Bullough, Advances in Physics **2**, 129 (1990).

[72] R. People and J. Bean, Appl. Phys. Lett. **49**, 229 (1985).

[73] B. Dodson and J. Tsao, Appl. Phys. Lett. **51**, 1325 (1987).

[74] W. Schommers and P. von Blanckenhagen, editors. *Topics in Current Physics: Structure and Dynamics of Surfaces I, and II.* Springer-Verlag, Berlin-Heidelberg-N.Y., 1987.

[75] D. King, Physics World **3**, 45 (1989).

[76] M. Lagally, editor. *Kinetics of Ordering and Growth at Surfaces.* Plenum Press, San Francisco, 1978.

[77] R. Bruinsma and A. Zangwill, Europhys. Lett. **4**, 729 (1987).

[78] M. Grabow and G. Gilmer. *Layered Structures and Epitaxy, edited by J.M. Gibson, G.C. Osbourn and R.M. Tromp*, page 13. MRS, Pittsburgh, PA, 1986.

[79] J. Bean, L. Feldman, A. Fiory, S. Nakahara, and I. Robinson, J. Vac. Sci. Technol. **A2**, 436 (1984).

[80] P. Peercy and G. Osbourn, J. Metals **39**, 14 (1986).

[81] J. Venables, G. Spiller, and M. Hanbucken, Rep. Prog. Phys. **47**, 399 (1984).

[82] W. Bollman. *Crystal Defects and Crystalline Interfaces.* Springer-Verlag, Berlin-Heidelberg-N.Y., 1970.

[83] J. Frenkel and T. Kontorowa, Phys. Z. Sowj. **13**, 1 (1938).

[84] J. van der Merwe and C. Ball. *Epitaxial Growth: edited by J.W. Matthews*, chapter 6, page 493. Academic Press, Inc., 1975.

[85] G. Olsen and R. Smith, Phys. Stat. Sol. (a) **31**, 739 (1975).

[86] G. Olsen and M. Ettenberg. *Crystal Growth: Theory and Techniques, edited by C. Goodman*, volume 2, chapter 1, page 1. Plenum Press, New York and London, 1978.

[87] J. Villain. *Ordering in Strongly Fluctuating Condensed Matter Systems, edited by T. Riste.* Plenum Press, New York, 1980.

[88] J. Villain. *Ordering in Two Dimensions, edited by S.K. Sinha.* Elsevier North Holland, inc., Holland, 1980.

[89] P. Bak, Reports on Progress in Physics 45, 587 (1982).

[90] T. Bohr, Phys. Rev. B 25(11), 6981 (1982).

[91] E. Kasper, H. Herzog, H. Daembkes, and G. Abstreiter. *Layered Structure and Epitaxy, MRS Symposium Proceedings, edited by J.M. Gibson and G.C. Osbourn and R.M. Tromp*, volume 56, page 265. MRS, Pittsburgh, PA, 1986.

[92] W. Brantley, Appl. Phys. Lett. 44(1), 534 (1973).

[93] J. Matthews and A. Blakeslee, J. Cryst. Growth. 27, 118 (1974).

[94] F. Nabarro. *Theory of Crystal Dislocations.* Dover, New York, 1990.

[95] C. Nuese and R. Enstrom, IEEE Trans. Electron Devices **ED-19**, 1068 (1972).

[96] B. Williams, Appl. Phys. Lett. 14, 273 (1969).

[97] K. Yoon, G. Stringfellow, and R. Huber, J. Appl. Phys. 62, 1931 (1987).

[98] H. Manasevit and W. Simpson, J. Electrochem. Soc. 120, 135 (1973).

[99] J. Noad and A. SpringThorpe, J. Electron. Mater. 9, 601 (1980).

[100] J. Duchemin, J. Hirtz, M. Razeghi, M. Bonnet, and S. Hersee, J. Cryst. Growth 55, 64 (1981).

[101] M. Razeghi and J. Duchemin, J. Vac. Sci. Technol. B1, 262 (1983).

[102] A. Roth, M. Sacilotti, R. Masut, D. Morris, J. Young, C. Lacelle, E. Fortin, and J. Brebner, Can. J. Phys. 67 (1989).

[103] C. Nordling and J. Osterman, editors. *Physics Handbook.* Studentlitteratur, Sweden, 1980.

[104] P. Atkins. *Physical Chemistry.* Freeman, Sweden, 1980.

[105] M. Abrahams, J. Blanc, and C. Buiocchi, Appl. Phys. Lett. **21(5)**, 185 (1972).

[106] K. Kuesters, B. de Cooman, and C. Carter, Philos. Mag. A **53**, 141 (1986).

[107] C. Snyder, B. Orr, D. Kessler, and L. Sander, Phys. Rev. Letters **66(23)**, 3032 (1991).

[108] W. Friedrich, P. Knipping, and M. von Laue, Munchener Sitzungsber. page 303 (1912).

[109] R. Feynman. *Quantum Electrodynamics.* W.A.Benjamin, Inc., New York, 1961.

[110] M. Sutton, Private Communication (1992).

[111] M. Sutton, S. Mochrie, T. Greytak, S. Nagler, L. Berman, G. Held, and G. Stephenson, Nature **352**, 608 (1991).

[112] C. Darwin, Phil. Mag. **27**, 315 (1914).

[113] Z. Pinsker. *Dynamical Scattering of X-rays in Crystals.* Springer-Verlag, Berlin, 1978.

[114] M. Born and E. Wolf. *Principles of Optics.* Pergamon, Oxford, 1975.

[115] J. Als-Nielsen. *Structure and Dynamics of Surface II, phenomena, Models, and Methods, edited by W. Schommers and P. von Blanckenhagen*, chapter 5, page 181. Springer-Verlag, Berlin Heidelberg New York, 1987.

[116] G. Vineyard, Phys. Rev. B **26**, 4146 (1982).

[117] R. Cowley and T. Ryan, J. Phys. C: Solid State Phys. **19**, 61 (1986).

[118] Y. Shi. A high resolution x-ray diffractometer for studying crystal epitaxy. Master's thesis, McGill University, Montréal, Québec, Canada, 1987.

[119] R. Pynn, Y. Fujii, and G. Shirane, Acta Cryst. **A39**, 38 (1983).

[120] R. Cowley, Acta Cryst. **A43** 825 (1987).

[121] C. Lucas, E. Gartstein, and R. Cowley, Acta Cryst. **A45**, 416 (1989).

[122] E. Gartstein and R. Cowley, Acta Cryst. **A46**, 576 (1990).

[123] W. Busing and H. Levy, Acta Cryst. **22**, 457 (1967).

[124] G. Wertheim, M. Butler, K. West, and D. Buchanan, Rev. Sci. Instrum. **45**(11), 1369 (1974).

[125] W. Voigt, Munch. Ber. page 603 (1912).

[126] P. Bevington. *Data Reduction and Error Analysis for the Physical Sciences.* McGraw-Hill, New York, 1969.

[127] A. Roth, preprint, to appear in J. Crys. Growth (1992).

[128] A. Kortan, A. Erbil, R. Birgeneau, and M. Dresselhaus, Phys. Rev. Letters **49**, 1427 (1982).

[129] A. Erbil, A. Kortan, R. Birgeneau, and M. Dresselhaus, Phys. Rev. B **28**(11), 6329 (1983).

[130] C. Lent and P. Cohen, Surf. Sci. **139**, 121 (1984).

[131] P. Pukite, C. Lent, and P. Cohen, Surf. Sci. **161**, 39 (1985).

[132] Q. Shen, J. Chang, G. Navrotski, and J. Blakely, Phys. Rev. Letters **64**, 451 (1990).